Identification of causal structure-function relationships with non-invasive brain stimulation

Dissertation

zur Erlangung des akademischen Grades Doktoringenieur
Dr.-Ing.

vorgelegt der Fakultät für Informatik und Automatisierung
der Technischen Universität Ilmenau

vorgelegt von Dipl.-Psych. Ole Numssen
geboren am 14. März 1987

GutachterInnen:
Prof. Dr. Thomas R. Knösche
Prof. Dr. Gesa Hartwigsen
Prof. Dr. Carsten Wolters

Abstract

Transcranial magnetic stimulation (TMS) is a popular non-invasive brain stimulation technique, allowing researchers and clinicians alike to draw causal inference about structure-function relationships in the human brain. This powerful method actively interferes with local brain processing by depolarizing cortical neurons with an induced electric field (e-field). However, TMS notoriously suffers from the high autocorrelation of its e-field, impeding a straightforward and precise functional mapping of the cortex.

Here, I present a novel paradigm that leverages recent advances in e-field modeling to critically improve the spatial resolution of TMS localization within the cortex - on the single subject level. This mapping approach integrates information from many different stimulation sites to pinpoint functionally relevant neuronal populations. The cortical stimulation is quantified via high-resolution e-field simulations, thus providing realistic estimates of the stimulation exposure. Subsequently, the cortical e-field exposure is fitted to the evoked response to identifying the cortical origin of the modulated function.

First, I build upon previous work on cortical activation functions by TMS and apply this to locate finger muscle representations in the primary motor cortex. In a follow-up experimental session, I validate the localization results utilizing a practice-oriented metric: the resting motor threshold (rMT).
Second, I implement a generalized analytical approach to allow for the integration of quasi-random stimulation sites. With this, the experimental feasibility and sampling efficiency are substantially improved, enabling robust and precise cortical mappings of multiple finger muscle representations concurrently.
Third, the routine and the complete analyses code are provided production-ready to facilitate further the application of this cortical mapping approach in real-world scenarios.

The utilization of causal activation functions for cortex mappings lays the foundation for a TMS-dosing metric based on subject-specific cortical field thresholds and potentially helps to unlock the currently unrealized potential of TMS.

Zusammenfassung

Transkranielle Magnetstimulation (TMS) ist ein nicht-invasives Hirnstimulationsverfahren, das im Klinik- und im Forschungsalltag eingesetzt wird, um kausale Struktur-Funktions-Beziehungen im menschlichen Gehirn zu identifizieren. Mittels eines induzierten elektrischen Feldes wird durch Depolarisierung kortikaler Neuronen aktiv in die Verarbeitung lokal begrenzter Hirnregionen eingegriffen. Allerdings beschränkt die hohe Autokorrelation des induzierten elektrischen Feldes eine präzise Lokalisation des TMS Effekts im kortikalen Gewebe.

In dieser Arbeit präsentiere ich ein neues Paradigma, das aktuelle Entwicklungen im Bereich Feldmodellierung verwendet, um die räumliche Auflösung von TMS Lokalisation signifikant zu erhöhen. Stimulationsreaktionen auf verschiedene Stimulationsorte werden in einer Analyse kombiniert um die involvierten Neuronenpopulationen zu identifizieren. Die Stimulation wird quantifiziert mittels hochauflösender Feldberechnungen, um eine realistische Abschätzung der kortikalen Stimulation zu erzielen. Die Güte des funktionalen Zusammenhangs zwischen Feldexposition und modulierten Verhalten wird genutzt, um die involvierte Neuronenpopulation zu identifizieren.

Als erste Annäherung verwende ich Input-Output-Kurven für eine Reihe von Stimulationsorten um Muskelrepräsentationen im primären Motorkortex zu lokalisieren. Ich validiere die Ergebnisse experimentell mit Hilfe der Ruhemotorschwelle um die praktische Relevanz einer präzisen Lokalisation aufzeigen.
Anschließend entwickele ich einen generalisierten Ansatz, der Stimulationen an beliebigen Orten zulässt, um die praktische Durchführbarkeit und Effizienz zu erhöhen. Diese Implementierung ermöglicht eine robuste und präzise Lokalisierung mehrerer Muskelrepräsentationen zugleich. Um die Einsetzbarkeit dieser Methode zu gewährleisten ist die gesamte Routine, inklusive aller Auswertungsskripte und eines Beispieldatensatzes, im Detail beschrieben und veröffentlicht.

Die Verwendung von Aktivierungsfunktionen zur Lokalisierung von Funktionen im Kortex ermöglicht die Verwendung einer Dosierungsmetrik, die auf individuellen, kortikalen Stimulationsschwellen basiert. Eine präzise, individualisierte Dosierungsmetrik kann dazu beitragen, die Sensitivität und Spezifität von TMS signifikant zu erhöhen.

Eigenständigkeitserklärung

Ich versichere, dass ich die vorliegende Arbeit ohne unzulässige Hilfe Dritter und ohne Benutzung anderer als der angegebenen Hilfsmittel angefertigt habe. Die aus anderen Quellen direkt oder indirekt übernommenen Daten und Konzepte sind unter Angabe der Quelle gekennzeichnet.

Bei der Auswahl und Auswertung folgenden Materials haben mir die nachstehend aufgeführten Personen in der jeweils beschriebenen Weise unentgeltlich geholfen:

- PD Dr. habil. Thomas R. Knösche: Interpretation der Analysen.
- Prof. Dr. Gesa Hartwigsen: Interpretation der Analysen.
- Dr. Konstantin Weise: geteilte Autorenschaft der Publikationen präsentiert in Kapitel 3 und 5. Teile, die maßgeblich auf Dr. Weises Arbeit beruhen (*sensitivity and uncertainty analyses*; *fractional anisotropy parametrization*), wurden nicht in diese Thesis integriert. Gemeinsame Diskussion der Ergebnisse und Implementierung des *curve-shift approaches*. Implementierung des *mesh refinements*.
- Jing Ying: Gemeinsame Ausarbeitung des Experimentalparadigmas zur Lokalisation von Aufmerksamkeitsprozessen und Datenakquise (Kapitel 6, Outlook).
- Prof. Dr. Axel Thielscher; Prof. Dr. Jens Haueisen; Dr. Benjamin Kalloch; Anna L. Zier: Gemeinsame Diskussion der Ergebnisse und Formulierung der Publikationen (Kapitel 3, 4 und 5).

Weitere Personen waren an der inhaltlich-materiellen Erstellung der vorliegenden Arbeit nicht beteiligt. Insbesondere habe ich hierfür nicht die entgeltliche Hilfe von Vermittlungs- bzw. Beratungsdiensten (Promotionsberater oder anderer Personen) in Anspruch genommen. Niemand hat von mir unmittelbar oder mittelbar geldwerte Leistungen für Arbeiten erhalten, die im Zusammenhang mit dem Inhalt der vorgelegten Dissertation stehen. Die Arbeit wurde bisher weder im In- noch im Ausland in gleicher oder ähnlicher Form einer Prüfungsbehörde vorgelegt. Ich bin darauf hingewiesen worden, dass die Unrichtigkeit der vorstehenden Erklärung als Täuschungsversuch angesehen wird und den erfolglosen Abbruch des Promotionsverfahrens zu Folge hat.

Ole Numssen, Leipzig, 12.12.2022

Acknowledgements

Glossary

active A real TMS condition, $\rightarrow$ sham TMS. 2

BA1 Brodmann areal 1. Somatosensory cortex. 42, 67, 96

BA3 Brodmann areal 3. Somatosensory cortex. 15, 42, 67, 96

BA4 Brodmann areal 4. Primary motor cortex (M1). 9, 42, 67, 70, 74, 82, 96

BA4a Anterior (rostral) part of BA4, *"the new M1"*. 4, 10, 125

BA4p Posterior (caudal) part of BA4, *"the old M1"*. 4, 10, 125

BA6 Brodmann areal 6. Dorsal premotor cortex (PMd). 4, 9, 15, 42, 67, 70, 74, 82, 96

BA17 Brodmann areal 17. Primary visual cortex / extrastriate cortex. 9

Brodmann areal The standard cortex atlas based on cytoarchitecture. 9

MNI A set of standard template brains created by the Montreal Neurological Institute. 20, 71, 96, 98, 102, 130

NIfTI An image format for MRI data. Follows RAS world coordinate system. 95

sham A placebo TMS condition without any real stimulation, $\rightarrow$ active TMS. 2

Talairach A template brain space centered on the anterior commissure and posterior commissure. 20

Acronyms

ADM *musculus abductor digiti minimi*. 66, 68–74, 78, 81–84, 89, 107, 109, 125

AIC Akaike information criterion. 32, 43

aMT active motor threshold. 17, 18

AP action potential. 3, 8, 13, 14, 34

APB *musculus abductor pollicis brevis*. 66, 68–74, 78, 81–83, 89, 109, 125

CMAP compound motor/muscle action potential. 14

CoG center-of-gravity. 19, 125, 126

CSF corticospinal fluid. 15, 36, 99

DCS direct cortical stimulation. 127

DWI diffusion weighted image. 86, 87, 93, 94, 98

e-field electrical field. xxiii, 2–5, 11–13, 15, 17, 18, 20–25, 28–40, 44, 46–49, 51, 52, 54–59, 62–65, 67–70, 72–77, 79–82, 84, 86–94, 96–101, 107, 112–114, 116–121, 124–134, 136, 137, 146–148, 151

EEG electroencephalography. 15, 104, 127

EMG electromyography. 14, 19, 43, 63–66, 68, 71, 87, 89, 90, 103–105, 107, 108, 110–113

FDI first *dorsal interosseous*. 16, 17, 20, 34, 54, 55, 57, 66–74, 78, 81–84, 89, 102, 104, 107, 109, 110, 119, 121, 125, 129, 131, 132

FEM finite element method. 22, 23, 35, 66, 67, 89, 92, 113

fMRI functional magnetic resonance imaging. 20, 97, 130, 135, 136

GM gray matter. 15, 36, 37, 86, 96, 98, 99

I/O curve input-output curve. 29–33, 37, 39, 41, 43, 44, 46, 55, 56, 62–64, 68, 75, 84, 87, 89, 107, 114, 120, 124, 126, 128, 130, 131, 133, 134

IPL inferior parietal lobe. 131–134

IPL$_{left}$ left inferior parietal lobe. 130, 131, 133

IPL$_{right}$ right inferior parietal lobe. 134–136

ISI inter-stimulus interval. 19, 41, 46, 52, 55, 67, 81, 103, 108

M1 primary motor cortex. xi, xxiii, 4, 9, 10, 13, 15, 17–19, 24, 25, 28, 29, 31, 34, 37, 39–42, 44–47, 49, 50, 53–56, 58, 67–70, 74, 81, 82, 87, 88, 96, 99, 108, 124, 125, 128, 129, 131

M1$_{hand}$ hand area of the primary motor cortex. 9, 10, 38, 130

M1$_{left}$ left primary motor cortex. 130–133

M1$_{right}$ right primary motor cortex. 130–133

MEP motor evoked potential. 4, 9, 14–16, 19, 20, 24, 25, 28–34, 39–41, 43–47, 54–56, 58, 62–68, 71, 79, 82, 86–90, 103, 106, 107, 109, 110, 114–117, 121, 124–127, 129, 131–133, 137

MR magnetic resonance. 10, 15, 19, 22, 94, 98

MRI magnetic resonance imaging. xi, xxv, 22, 35, 36, 67, 86, 87, 90, 93–95, 98, 125

MSO maximum stimulator output. 17, 18, 24, 31, 35, 41, 82, 117, 118, 121, 130, 131

MT motor threshold. 16–18, 24, 29, 52, 81, 116, 121, 124, 126, 129, 133

NIBS non-invasive brain stimulation. 2, 3, 5, 9, 13, 21, 25

NRMSD normalized root-mean-square deviation. 75, 78, 79, 84, 115

PM premotor cortex. 9, 42

PMd dorsal premotor cortex. xi, 4, 10, 14, 15, 37, 67, 69, 70, 74, 96

PMdc caudal PMd. 9, 10, 125

rMT resting motor threshold. xxiv, 17, 18, 41, 54, 55, 63, 67, 68, 80–83, 86, 87, 104, 106, 107, 117–119, 121, 126, 129–133

ROI region of interest. xxv, 32, 33, 37, 49, 64, 68, 69, 86, 87, 96, 97, 100, 101, 113–115, 131

rTMS repetitive TMS. 12–14, 18, 24, 135

Contents

Figures

List of Tables

List of Code Listings

"One of the first things taught in introductory statistics textbooks is that correlation is not causation. It is also one of the first things forgotten."

–Thomas Sowell

Chapter 1
Introduction

1.1 Motivation

The human brain, *our* brain, constitutes our selves and gives rise to perceptions of the world around us. Despite all efforts, its functional architecture remains to be discovered to the greater parts. For centuries, invasive-, ablation- and disease-based brain research drove these efforts, only until recent advances finally enabled high-resolution, in-vivo insights into the processing of unaltered, intact brain tissue. Not interfering with the brain tissue before or during data acquisition rendered modern neuroscientific research possible: by allowing to test a vast manifold of hypotheses experimentally.

However, this dogma resulted in a fundamental shortcoming: a mere *correlative nature* of inference. In contrast, an upcoming set of neuroscientific methods allows for *causal inference on structure-function relationships* (Siddiqi et al., 2022a), with the disadvantage of low spatial resolution: non-invasive brain stimulation (NIBS), with its most prominent representative: transcranial magnetic stimulation (TMS). In addition, despite its widespread application in clinical and research environments, currently no robust model predicts the TMS-induced effects on functional processing within the cortex (Sasaki et al., 2018). Even within a single subject, for the very same cortical target, TMS may exhibit reduced (*inhibited*) or increased (*facilitated*) cortical activity after stimulation – or no change at all (Ziemann & Siebner, 2015; Bergmann et al., 2016; Sasaki et al., 2018). Naturally, this lack of predictability introduces high levels of unexplained variance and, thus, small effect sizes at the group-level. Driving this uncertainty has been a binary understanding of the experimental factor *TMS*: active stimulation versus sham stimulation. In reality, cortical stimulation follows a finely-grained continuum across a wide range of temporospatial electromagnetic field exposure. Only through recent methodological advances the mode of action of TMS, the induced electrical field (e-field), can realistically be estimated for individual head geometries and stimulation conditions.

However, it had to be shown that e-field modeling not only provide a plain quantification of cortical stimulation exposure but, instead, that e-field modeling can help explain TMS effects on the human brain. Finally, a framework using e-field modeling to substantially add to the understanding of the functional underpinnings of our brain itself remained to be proposed. This shall be done in this thesis.

Over time, neuroscientific concepts have become more abstract, as did the statistical methods we use to test our hypothesis. And data got big. This complexity, these vastly increased degrees of freedom, urgently call for a paradigm to robustly test the *causal relationships* between cortical tissue and behavior – with *high resolution*, on the *subject-level*.

NIBS approaches are, in principle, capable of providing these precise insights, but current experimental paradigms and statistical techniques need to exploit their potential sufficiently. I combined state-of-the-art e-field modeling approaches and a novel, applicable experimental framework to leverage the available methodological and computational infrastructure to overcome these limitations.

1.2 Aims

With this thesis, I put forward a concept to integrate results from realistic e-field modeling with a behavioral outcome to allow for the identification of cortex-level stimulation effects.

The fundamental goal of the work presented in this thesis is two-fold:

(a) Development of a methodological concept to robustly locate functional representations in the cortex with TMS on the subject-level.

(b) Development of an experimental framework implementing such a cortical mapping approach in a reliable and applicable manner.

For the most part, processing in the brain is implemented via inter-neuronal communication. Locally, neurons aggregate information from multiple inputs and transmit the result via electric signals (action potentials, APs) to downstream neurons. TMS can hijack this electric communication with a short electromagnetic pulse by directly evoking action potentials due to a local change in membrane potential. [1] However, due to technical limitations, the TMS-induced e-field is not focal enough to allow the differentiation of close cortical spots per sé but instead covers significant parts of the cortex with gradient intensities.

---

[1]In this work, I focus on the above-threshold effects of TMS.

The fundamental idea of the work presented here is to combine multiple stimulation sites to assess the cortical activation function between induced e-field and observable outcome. I will show how combining multiple induced e-fields with the evoked responses can precisely identify a structure-function relationship on the cortex – and eliminate irrelevant regions.

As a first step, a novel experimental and methodological approach is implemented to leverage information from multiple stimulation sites to locate cortical representations of finger muscles. This proof-of-concept parallels and advances previous TMS mapping approaches and closely follows assumptions about neuronal activation curves. In the second step, I advance this novel mapping approach to allow its usage in real-life research and clinical environments. This adaptation includes a simplified experimental design and a generalized statistical approach with higher discriminatory power. Despite being developed within the human primary motor system, this mapping approach shall yield a principled approach to generally map cortical functions. As an outlook, I will provide first results that map functions of higher cognition, in this case, attentional processes, on the subject-level. In addition, a dosing metric that relies on individual cortical field thresholds is derived from this cortical mapping approach, and its superiority to current dosing schemes is illustrated.

1.3 Contributions

1.3.1 Scientific contributions

- A novel paradigm to identify structure-function relationships with TMS based on cortical stimulation effects
- Identification of the gyral rim of the PMd (dorsal premotor cortex; BA6) as the effective stimulation site for motor evoked potentials (MEPs) as opposed to M1 (primary motor cortex; BA4a/BA4p).
- Identification of the e-field magnitude $|E|$ as the driving factor for effective cortical stimulation as opposed to tangential ($E_{\parallel}$) and normal ($E_{\perp}$) components.
- Identification of individual-specific cortical e-field thresholds to TMS.
- A novel TMS dosing method relying on individual cortical e-field threshold to

minimize the across-subject variance of stimulation effects.

1.3.2 Methodological contributions

- A production-level toolchain covering data acquisition, post-processing, functional localization, and individual e-field-based dosing. With Dr. Konstantin Weise and Dr. Benjamin Kalloch.
- Prospective position/orientation optimization based on e-field simulation, available via the SimNIBS package.
- *pyNIBS*: a Python package to link e-field simulations of NIBS experiments with behavioral outcomes to allow functional localization. With Dr. Konstantin Weise and Dr. Benjamin Kalloch.
- *MagicPy*: A Python-based tool to control MagVenture stimulator devices.
- *IMporter*: A tool to import pre-computed coil positions/orientations into Localite TMSNavigator sessions. With Dr. Benjamin Kalloch.

1.4 Thesis layout

The second chapter presents a concise background about the foundations of this thesis: This includes an overview of the modes-of-action of TMS, current best practices of TMS application, and a short introduction to cortical neurons and inter-neuronal communication. I further provide details on the e-field modeling part due to the importance of the e-field estimations for the presented mapping approach.

In the third chapter, I introduce a proof-of-principle to locate cortical muscle representations in the primary motor cortex based on cortical input-output curves. I compare this method to classic and modern mapping procedures and show its superiority concerning cortical resolution. Multiple fitting families are compared by means of their computational cost and potential information gain. Lastly, I present an experimental validation scheme and its results.

An optimized version of this initial approach is presented in the fourth chapter. Here, I aimed for a highly practicable experimental design by allowing quasi-random stimulation conditions to increase variance between local e-field vectors. I modified the previous analysis strategy into one generalized linear model. Two quantification

schemes are presented to address different goal functions, i.e., accuracy versus precision.

The fifth chapter contains a peer-reviewed, production-ready implementation of this improved mapping approach. This chapter thoroughly explains the experimental part and all analytical steps, including the analysis code.

In the final, sixth chapter, the mapping procedure is revisited to discuss its gain for the neuroscientific and clinical community. I present how my cortical localization scheme may be generalized to map higher cognition. In addition, I demonstrate how to use this mapping approach to derive an individual, physiologically plausible dosing metric to boost TMS effect sizes, both on the single subject- and the group-level.

Chapter 2
TMS – state-of-the-art

Transcranial magnetic stimulation (TMS) is one of the few techniques allowing non-invasive super-threshold stimulation of the human cortex. A short electromagnetic pulse depolarizes cortical neurons in a delimited area and, thereby, interferes transiently and directly with their information processing. This induced change in brain processing renders causal inference about structure-function relationships within the healthy human brain possible. But in contrast to these potentially strong and direct effects of TMS, results on the group and on the subject-level often remain elusive (Hannah et al., 2016; Siddiqi et al., 2022b).

Despite its broad and ever-increasing application in research and clinical environments (McLean, 2019; Zheng et al., 2020), the TMS community lacks integration of technological advances and scientific discovery and, thus, does not tap the full potential of TMS. Below, I present short introductions into the relevant methodological backgrounds upon which the remainder of this thesis will rely and build to create such an integrative approach to TMS.

2.1 Cortical organization

2.1.1 Cortical neurons and information processing in the human cortex

An simplistic characterization of the human cortex could differentiate two fractions: extracellular space and intracellular space, partitioned by cortical neurons. The membrane potential, i.e., an electric potential difference between intra- and extracellular space, is actively maintained by ion pumps within the cell's membrane.
Information, in this case, incoming action potentials (APs) from pre-synaptic neurons, is integrated across time and space via local changes in membrane potential. Eventually, the membrane is locally depolarized to the degree that evokes an AP. This AP can travel along the neuron's axon to transmit to the dendrites of connected downstream neurons. This electrical mode of action of interneuronal communication is targeted by TMS (see below).
A slightly less over-simplistic characterization could differentiate types of neurons

---

Chapter image depicts the setup of one of the first electromagnetic brain stimulation experiments (Magnusson & Stevens, 1914), reproduced from Walsh and Pascual-Leone (2003).

across the cortex with different physiological properties. Same-type neurons cluster in space, creating cortical layers (Hagan et al., 2012) that allow defining cortical parcellations based on the *cytoarchitecture* (Brodmann areal; BA; Brodmann, 1909). Prominent NIBS targets include primary cortical regions, which are closely connected to sensory or motor systems; here, stable and accessible outcome measures exist, for example, phosphenes for primary visual cortex (V1/BA17) stimulation (Thielscher et al., 2010) and motor evoked potentials (MEPs) for motor cortex (subsubsection 2.2.3.1) stimulation.

2.1.2 Cytoarchitecture of the human motor cortex

Of the many cortical regions involved in motor control, only two possess direct cortico-motor-neurons: the primary motor cortex (M1; BA4) and the premotor cortex (PM; BA6; Dum & Strick, 2004). These projections from the cortex to lower motor neurons in the spinal cord to motor units in the muscles' bellies allow high-speed information transfers. M1 and PM represent the body's motor system in a somatotopic manner – the *homunculus*. Traditionally understood as one complete representation within M1 (Penfield & Rasmussen, 1950), this concept has been challenged in various ways, from proposals for one somatotopic map spanning all cortical motor subregions (Graziano et al., 2002) to multiple maps within M1 (Huber et al., 2020).

The distinction of the motor system into M1 and PM was initially based on cytoarchitectonic markers, for example, the lack of cortical layer IV, the *granular* layer, in M1 compared to other regions of the cerebral cortex (Geyer et al., 2000). A more finely-grained and functionally specific differentiation of M1 and PM has been put forward (Rizzolatti & Fabbri-Destro, 2009) based on a multi-method approach, including invasive and non-invasive brain stimulation. Currently, six subregions of the motor system have been demarcated with significant inter-individual variance. Of these, only the caudal PMd (PMdc) and the hand area of the primary motor cortex (M1$_{hand}$) are further described here due to their proximity to one another and their importance in TMS research (Siebner et al., 2022).

HAND AREA OF THE PRIMARY MOTOR CORTEX (M1$_{hand}$). This area is situated within the posterior sulcal wall of the precentral gyrus. It was further differentiated

into two subregions based on cytoarchitectonics (Geyer et al., 1996) and via projection profiles to corticospinal motorneurons (Witham et al., 2016). Fast, monosynaptic cortico-motorneuronal connections exist only in the anterior part (BA4a, the "*new M1*"), whereas slower downstream connections via interneurons predominate in the posterior part (BA4p, the "*old M1*") of $M1_{hand}$.

Cytoarchitectonically, M1 can be distinguished from PMd due to differences in neuronal density in multiple layers and myelinization and by larger layer V pyramidal cells (Geyer et al., 1996; Glasser & van Essen, 2011; Preuss et al., 1996). These difference in neuronal structures of BA4p and $M1_{hand}$ is paralleled by a lower cortical stimulation threshold for direct microstimulation (Graziano et al., 2002).

CAUDAL PMD (PMDC). Also known as *F2*, PMdc is located directly anterior to M1 at the gyral rim and the gyral crown of the precentral gyrus. Striking similarities between human and non-human primates have been shown for the cytoarchitectonic and functional organization of PMd. Direct electrical stimulation and TMS experiments identified the PMdc's relevance for direct hand muscle contractions and for more complex tasks (Rizzolatti & Fabbri-Destro, 2009).

THE HAND KNOB. Parts of M1/BA4a, together with PMdc, form the *hand knob* (Dubbioso et al., 2021). This functionally defined area is often referred to as *the* cortical region relevant for single-finger muscle control without further differentiating between M1 in PMd (Rossini et al., 2015). Due to its prominent Ω or ϵ shape (Yousry et al., 1997), this area can be easily identified on structural MR images. The hand knob is the main target to assess individual stimulation thresholds TMS (see below).

DOWNSTREAM CONNECTIVITY TO MOTOR UNITS. An action potential from the motor cortex reaches a muscle fiber within 20 ms (Müller & Ziemann, 2007). This fast transmission is possible due to an optimized, monosynaptic cortico-spinal pathway, which is uniquely found in primates. Upper motor neurons, for example, Betz cells, are located within the motor cortex and terminate on α-motor neurons (lower motor neurons) in the spinal cord (Florman et al., 2013). The axon of any lower motor neurons might terminate on multiple muscle fibers to innervate them concurrently (see subsubsection 2.2.3.1). This pathway forms the primary source to control skeletal muscle activity.

2.2 Transcranial magnetic stimulation

2.2.1 Physical background

TMS is based on the principle of electromagnetic induction to generate an electric current within the cortical sheet (Barker et al., 1985). Specifically, a capacitor in a stimulator device is charged and subsequently discharged through the TMS coil, which is positioned on the head surface of a volunteer above the cortical stimulation target. This short and strong current I yields a time-varying magnetic field $\vec{B}$:

$$\vec{B}_P = \frac{\mu_0}{4\pi} \int_W \frac{I d\boldsymbol{l} \times \hat{\boldsymbol{r}}}{|\boldsymbol{r}|^2} \qquad \text{Biot-Savart law} \quad (2.1)$$

where:
$\vec{B}_P$ = magnetic flux density at point P,
μ_0 = magnetic constant,
W = path along the wire,
I = electrical current in W,
$d\boldsymbol{l}$ = infinitesimal segment of W,
$\boldsymbol{r}$ = displacement vector from $d\boldsymbol{l}$ to point P,
$\hat{\boldsymbol{r}}$ = unit vector from $d\boldsymbol{l}$ to point P.

The magnetic field subsequently causes an electrical field (e-field) in the conductor, which in this case is the head of the volunteer:

$$\nabla \times \vec{E} = -\frac{\partial \vec{B}}{\partial t} \qquad \text{Faraday's law of induction} \quad (2.2)$$

where:
$\vec{E}$ = electric field strength,
$\nabla \times$ = curl,
$\vec{B}$ = magnetic flux density,
t = time.

This simplified view identifies three important relationships:

- $|\vec{E}|$ decreases in a quadratic manner with distance (r^2 in eq. 2.1)
- $|\vec{E}|$ is proportional to the (local) conductor permeability (μ in eq. 2.1)
- $\vec{E}$ is dependent on the rate of change of Φ (eq. 2.2)

Magnetic flux densities in human TMS studies reach up to approximately 2 T, and peak slew rates reach to about $170\,A\,\mu S^{-1}$ (Hallett, 2007; Thielscher & Kammer, 2002), depending on the utilized hardware. Realized cortical field strengths are often below $200\,V\,m^{-1}$.

2.2.2 Stimulation parameters

Various parameters define a specific TMS application, covering the spatial, temporal, and intensity domain.

PULSE SHAPE AND STIMULATOR INTENSITY. The stimulator device defines the magnitude of the current I sent through the TMS coil and its temporal rate of change. In general, a higher rate of change, i.e., a shorter pulse width, leads to a larger realized $\vec{E}$ (cf. eq. 2.2). Two types of pulse shapes with different modes-of-action on the neuronal level are widely used in TMS experiments: *bi-phasic* pulses, i.e., a full oscillation of I, and *mono-phasic* pulses, i.e., a half oscillation with a steep rise and a slow decline. Here, bi-phasic pulses were used due to more robust stimulation effects of the motor cortex across different TMS coil orientations (Davila-Pérez et al., 2018; Kammer et al., 2001)

COIL TYPES. The TMS coil is positioned tangentially on the subjects' head surface, in classical TMS experiments as close as possible to the cortical target to maximize the neuronal stimulation exposure. The shape of the primary e-field E_{prim}, for example, its focality and spread, is defined by geometric and electric properties of the coil winding or windings. Here, so-called *figure-of-eight* coils (Epstein, 2012) were employed in this work. This coil type contains a set of two inversed coil wirings that sit side-by-side in the TMS coil housing to generate a comparatively focal e-field hotspot under the center of the coil (see subsection 2.3.5 and Ueno et al., 1988).

STIMULATION PROTOCOLS. TMS protocols are divided into *single-pulse* and *repetitive TMS (rTMS)* protocols. *Single-pulse* refers to applying TMS pulses at a

frequency below 1 Hz. *Repetitive TMS* covers different protocols from simple, uniform *bursts*, for example, 5 pulses á 10 Hz (Bergmann et al., 2016) to longer (30 s – several minutes) and more complex patterns (e.g., theta burst TMS; cTBS; Huang et al., 2005). Some of these patterns build on findings from direct stimulation of excised cortical tissue in animals, for example, long-term potentiation/depression (LTP/LTD; Clapp et al., 2012).

In general, single-pulse TMS can be used to map primary cortical regions like the primary motor cortex (M1) or the primary visual cortex (V1). In contrast, rTMS protocols are utilized to target areas of higher cognition (Pascual-Leone et al., 1999) because prolonged disruption of neuronal processing is necessary to yield behavioral results.

2.2.3 Biophysiological effects

TMS is part of the superthreshold stimulation NIBS techniques. The induced e-field, i.e., the *secondary* e-field, in the cortex can directly elicit action potentials (APs) in groups of neurons as long as the potential difference between intra- and extracellular space (*membrane potential*) is increased above the activation threshold (see section 2.1). This threshold varies within the temporal domain, depending on the current intrinsic excitability of the neuron, e.g., whether it is in the refractory period or close to an AP (Bergmann et al., 2012). In addition, the threshold also differs in the spatial domain across the different parts of a single neuron; In general, highly myelinated axons are more susceptible to TMS than less myelinated parts (Hannah & Rothwell, 2017). Finally, the local orientation of a neuron in relation to the local e-field gradient (see subsection 2.2.1) is critical for either local depolarization or local hyperpolarization. In combination, these factors lead to distinctively different activations patterns across neuronal types, cortical layers, and, most probably, cortical regions. Simulation studies have identified the primary activation of layer 5 pyramidal cells and interneurons in layers 2/3 of the primary motor cortex (Aberra et al., 2020). To effectively reach cortical targets, often situated several centimeters below the head's skin surface, a certain stimulator intensity is necessary. Due to the cone-shaped spatial profile of the induced e-field (see subsection 2.2.1) an increased stimulation depth is always accompanied by an increased spatial spread in the other two dimensions as well, decreasing the stimulation's focality. Importantly, APs

propagate transsynaptically to connected neurons, potentially affecting local and distal (*remote effects*; Paus, 2005) neuronal circuits.

In summary, a single TMS pulse can elicit APs from multiple neurons, but the specific activation pattern depends on a complex spatiotemporal interaction between TMS hardware and tissue.

Motor evoked potentials

The motor evoked potential (MEP) is a muscle response evoked by cortical stimulation: When a TMS pulse depolarizes cortical neurons, for example, in PMd, descending volleys travel through downstream connections (see subsection 2.1.2) to skeletal motor units. Each motor unit might depolarize (motor unit action potential, MUAP) with some temporal variation across motor units (Siebner & Rothwell, 2003). The MEP is the compound motor/muscle action potential (CMAP) of all activated motor units, measured via electromyography (EMG).
While, in principle, TMS can elicit MEPs in any muscle, most often, finger muscles of the dominant hand are targeted. Effective stimulation of these muscle representations is possible with comparatively low stimulation intensity (see below and Di Lazzaro et al., 2004) due to their large and superficial position on the gyral crown or rim of the motor cortex. MEPs are an objective and quantitative metric to measure super-threshold stimulation of the involved cortical regions (Pellegrini et al., 2018).

2.2.4 Safety and adverse effects

Inducing strong currents in brain tissue comes with several health concerns that must be addressed and monitored. The super-threshold nature (subsection 2.2.3) of TMS can induce seizures and syncopes due to the synchronized depolarization of a large set of neurons. The pool of TMS volunteers should be carefully selected based on their medical records if possible. Exclusion criteria should include all risk factors that increase the likelihood of seizures, for example, family history, brain damage, and drug setting to minimize the occurrence probability of these adverse effects, In addition, stimulation parameters have been extensively reviewed to identify the boundaries of safe TMS application. The application of single-pulse TMS is considered safe, whereas, for the application of rTMS protocols, specific guidelines
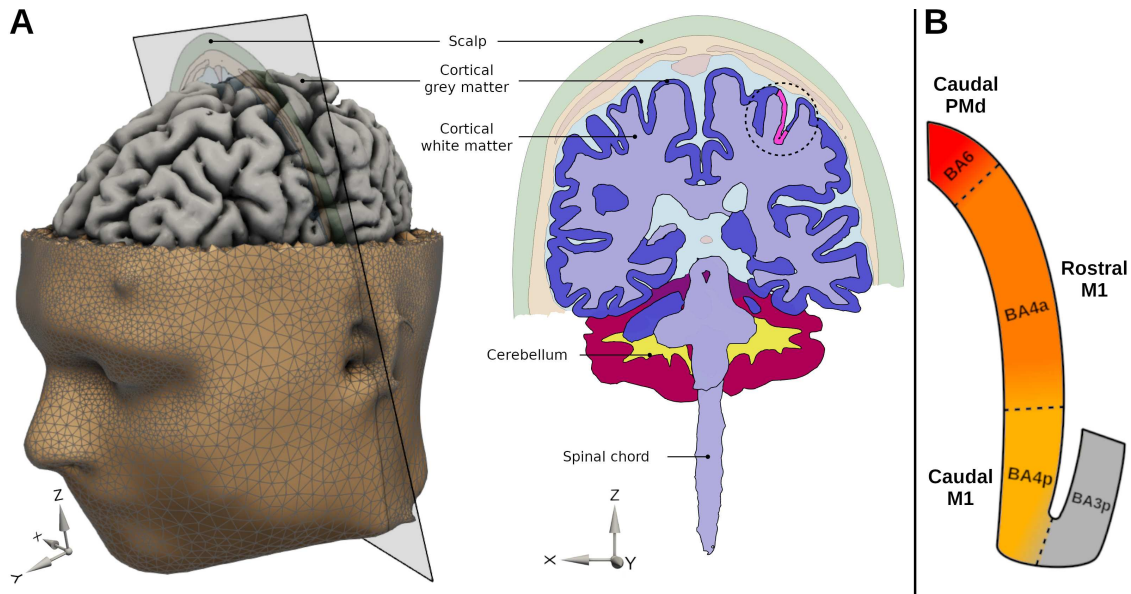
Figure 2.1: Individual head models allow precise e-field computation.
A) left: high-resolution head model constructed from structural MR images with exposed cortical gray matter (GM) surface. The mesh structure, i.e., nodes and triangles, is overlaid on the skin surface (left). The opaque slice through the motor cortex (left) is projected into 2D (right). Right: axial slice to visualize the major tissue types. Pink gray matter region: primary motor cortex (primary motor cortex and dorsal premotor cortex), covering the handknob area. B) Both, dorsal premotor cortex (PMd) and primary motor cortex (M1) provide downstream connections towards motor units and, thus, are possible TMS targets to elicit motor evoked potentials (MEPs). BA3 - BA6: alternative nomenclature based on cytoarchitecture. Handknob inset adapted from Weise & Numssen et al. (2020)[1].

exist for different combinations of stimulation parameters (Rossi et al., 2009). In general, higher stimulation intensity and higher stimulation frequency increase the probability of adverse effects. In current safety regulations (Rossi et al., 2021; Rossini et al., 2015), the stimulation intensity is individualized based on the motor threshold to adjust for individual differences, like skull- and CSF-thickness (see below for limits of this approach). Under these safety regulations, the rate of TMS-induced seizures is remarkable low ($\sim 1/100\,000$ sessions for individuals without risk factors).

The second set of potential adverse effects, including heating and dislocation, stem from the interaction between the induced e-field and third-party products, for example, EEG electrodes, deep brain stimulation devices, or cochlea implants.

---

[1]Throught the thesis I provide all first authors for shared-first publications.

Finally, each TMS pulse is accompanied by a distinctive acoustic artifact due to a rapid deformation of the TMS coil during the pulse. This artifact, up to 140 dB depending on coil type and stimulation intensity (Koponen et al., 2020), can introduce lasting hearing damage and even hearing loss, both in volunteers and in experimenters. To guard against this hearing protection, e.g. earplugs, must be used throughout any TMS experiment.

In summary, the strong electromagnetic TMS pulse introduces relevant risk factors. Following current safety guidelines (Rossi et al., 2021) guards effectively against adverse effects, especially for healthy volunteers employed in this work.

2.3 Current best practices of TMS

2.3.1 Dosing

The main lever to standardize stimulation across subjects in a study is the TMS dosing, i.e., the individualization of cortical stimulation exposure (Rossi et al., 2009). Optimally, the stimulation intensity is individually selected so that

- the targeted neuronal populations are effectively stimulated,
- surrounding cortical regions are not affected,
- stimulation exposure is the same across subjects,
- no adverse effects (see subsection 2.2.4) arise.

Motor threshold

The motor threshold (MT) was an early concept to estimate the individual stimulation threshold for TMS, and it (or one of its derivatives) is still the method of choice for most TMS studies (Beynel et al., 2019). Its underlying idea is to assess the individual stimulation threshold with an objective measurement: the intensity needed to elicit motor potentials (MEPs; see subsubsection 2.2.3.1). In addition, by defining the MT as the lowest threshold to elicit MEPs, this threshold yields a sufficient margin to safely apply TMS in healthy subjects (see subsection 2.2.4; Rossi et al., 2009).

While a motor threshold can, in principle, be determined for any body muscle (see below), most often, the first *dorsal interosseous* (FDI) muscle, i.e., the abductor

muscle of the index finger, of the dominant hand is chosen (S. M. Krieg et al., 2017, Supplemental Material). This criterium is a conservative choice as the thresholds are generally lower for upper limb muscles (Rossi et al., 2009) and lower within the dominant hemisphere (Hammond, 2002).

Two versions of the MT exist, depending on whether the targeted muscle (e.g., FDI) is at rest (resting motor threshold, rMT) or actively contracted (active motor threshold, aMT). Due to its wide adoption in current TMS research, I focus on rMT.

The MT for an individual is given in % of the maximum stimulator output (MSO) and, thus, is only valid for a specific TMS system (stimulator device, coil, extension cables). Importantly, the cortical e-field exposure, which is the underlying mode of action of TMS, is not directly quantified by the MT. Nevertheless, in most TMS experiments, the MT is used as the stimulator intensity for the targeted cortical area, often outside the motor cortex. This application of a stimulator intensity metric (versus a cortical stimulation intensity metric) introduces two major sources of variance: i) The neuronal e-field thresholds might differ between M1 and the cortical target. For example, differing neuronal e-field thresholds can arise due to different prevalences of neuron types. So far, lacking knowledge about the primary neuronal targets of TMS renders this possibility elusive. ii) The same stimulator intensity can yield different cortical e-field strengths at different stimulation targets. The local anatomy, i.e., the distribution of different tissue types, strongly influences the spread of the induced e-field. Most often, differences between M1 and the stimulation target have been approximated via the scalp-cortex distance (see below), i.e., the distance of the cortical target to the coil center on the skin surface.

Distance-adjusted motor threshold

An early heuristic to adjust the MT to different anatomical characteristics between the M1 area and the stimulation target had been put forward by Stokes et al. (2005). Since individual e-field estimations were not readily available in 2005, Stokes and colleagues measured the resting motor thresholds (rMTs) as a proxy for different scalp-cortex distances. Subsequently, a simple linear model ($MT = a + m * dist$) was fitted to the data to quantify the effect of scalp-cortex distance. Interestingly, a highly significant fit ($p < 0.001, R^2 = 0.97$) was identified, which robustly predicted

the rMT: $rMT = 1.3 + 2.9 * dist$. This linear relationship contrasts with expectations based on the quadratic decline of the e-field over distance. Based on these results, the so-called *Stokes algorithm* has been employed by many studies to equalize difference cortical depths:

$$MT_{adj} = MT + m * (D_{target} - D_{M1}) \qquad \text{Stokes algorithm} \quad (2.3)$$

where:

MT = motor threshold in %MSO,

MT_{adj} = adjusted motor threshold in %MSO,

m = spacial gradient; most often $m = 3$ is used,

D_{target} = scalp-cortex distance in mm at cortical target,

D_{M1} = scalp-cortex distance in mm at M1.

Caveats

Several factors impede the power of rMT and aMT to assure between-subject-comparability of the cortical stimulation intensity:

- The motor threshold is assessed in terms of the stimulator output, whereas the mode of action of TMS is the cortical e-field.
- The relationship between motor cortex excitability and other cortical regions is unknown.
- The relationship between single-pulse thresholds and rTMS thresholds is unknown.
- The classic motor threshold hunting is a manual procedure, thus relying on experimenter skills to find the optimal stimulation solution (see below).

2.3.2 Motor threshold hunting

The process to determine the motor threshold (MT) is formalized as the *motor threshold hunting* procedure (Rossini et al., 1994): single pulses are delivered to the motor cortex, and consecutive muscle innervation is observed. Due to its wide

acceptance, I only outline the *5–10–Rothwell* (Rothwell et al., 1999) method:
The TMS coil position and orientation is manually optimized until an optimal
combination is found, i.e., yielding minimal stimulator intensity, to generate mus-
cle innervation. Nowadays, muscle innervation is measured via electromyography
(EMG) surface electrodes to objectively quantify muscle activity by their electric
activity (Kleim et al., 2007).

2.3.3 Structure-function mapping techniques for the motor cortex

The motor cortex has been a major target for TMS mappings due to its simple cortico-
muscular downstream pathways and the existence of a quantitative outcome measure:
the MEP. However, no consensus exists about the best practices of motor mapping
techniques – except for using neuronavigation systems to track the TMS coil with the
help of subject-specific structural MR images. A recent meta-analysis (Sondergaard
et al., 2021, Supplemental Material) identified 130 TMS motor mappings studies:
96 different motor mapping techniques were employed (own analysis). Within the
34 neuronavigated mappings, 31 different mapping paradigms were applied. Almost
all mappings (e.g., Van De Ruit et al., 2015; Ngomo et al., 2012; Kleim et al.,
2007; Neggers et al., 2004) defaulted to a pre-experimentally generated coil grid on
the skin surface above M1. This grid defined all coil positions (and, less often, coil
orientations) to be tested. Grid sizes covered 5x5 to 10x10 sampling locations with a
typical spacing of 1 cm to 2 cm between grid points (Kraus & Gharabaghi, 2015,
2016; Mathew et al., 2016). At each grid position, one or multiple single TMS pulses
were delivered at a fixed stimulation intensity, and the EMG signal is recorded. These
factors, covering grid properties, i.e., number of positions and grid resolution, coil
orientation, and pulse configuration (pulse shape, intensity, number of pulses, ISI),
varied across studies. Most often, the center-of-gravity (CoG) approach was used to
estimate the cortical origin of the MEPs. Here, the grid locations are weighted by
their MEP amplitude to identify the location of the coil position that produced the
maximum MEPs.

Importantly, this procedure can only provide information about an optimal coil
location – in contrast to identifying the cortical representation of the examined
function, in this case, the MEP. The identified location on the head's skin surface is
often projected orthogonally downwards onto the gray matter surface to estimate

the cortical origin of MEPs. In few cases, the induced e-field is computed and used for an approximate cortical localization instead of a mere projection (Pitkänen et al., 2017; Laakso et al., 2018). In total, methodological shortcomings and considerable differences in the experimental realizations yield imprecise and variable mapping results, with intraclass coefficient correlations for the FDI muscle as low as 0.14 (Sondergaard et al., 2021, Supplemental Material).

2.3.4 Target selection for higher cognitive domains

TMS studies of higher cognition most often do not functionally define the cortical target based on stimulation results (Bergmann et al., 2016), but instead rely on other modalities, for example, with an fMRI realization of the functional domain of interest. Only recent advances increased the mapping resolution and regional specificity to map language processing with TMS by introducing a sound statistical approach to exploit the modulation of single-trial reaction times (Sakreida et al., 2018, 2019). Nevertheless, this approach has only been used to yield group-level mapping results. In addition, individual TMS targets are often based on group-level or meta-analytical (fMRI) results instead of individual pre-TMS localization (Hartwigsen et al., 2013). This procedure introduces several shortcomings for the TMS study implementation and subsequent interpretation:

- Correlative brain activation results, for example, from fMRI, do not necessarily coincide with the optimal neuronal targets for TMS (Rossini et al., 2015).
- Functional alignment: Group-level results only provide average activation peaks and may miss individual activation peaks (Hartwigsen & Bzdok, 2018; Braga & Buckner, 2017).
- Structural alignment: The transformation between group-level brain templates, i.e., MNI or Talairach templates, and single-subject brain anatomy yields considerable variance (Wu et al., 2018).

Together, these factors add considerable uncertainty about the adequateness of the individual cortical targets, negatively affect group-level effect sizes, and impede the interpretation of null results.
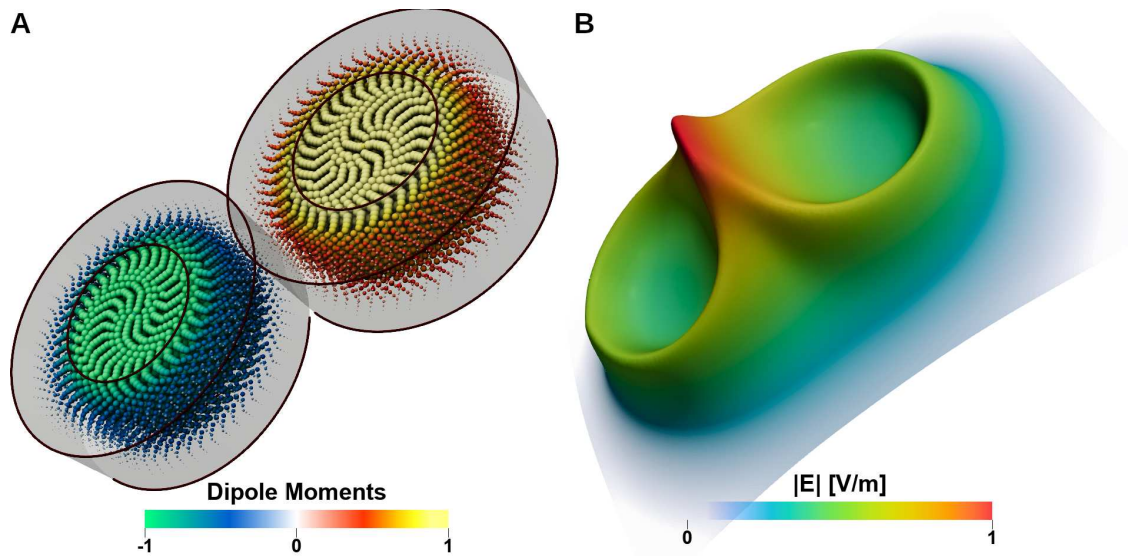
Figure 2.2: Coil model and e-field simulations of a figure-of-eight TMS coil.
A figure-of-eight TMS coil generates a comparatively focal e-field $\vec{E}$ that peaks under
the center of the coil. A) Prototypical figure-of-eight TMS coil model with casing (gray)
and magnetic dipoles used for computation of B. Size and color: dipole moment. B)
The magnitude of the e-field, $|E|$, 2 cm below coil housing. Field strength is color- and
height-coded. The simulation was performed with an arbitrary stimulator intensity.

2.3.5 Modeling the induced e-fields

NIBS e-field simulations can be employed either prospectively, for example, to select a
specific coil position with optimal target stimulation, or retrospectively to individually
quantify the realized induced e-fields (Hartwigsen et al., 2015). Four sources cover
the necessary information to conduct e-field simulations for TMS:

 i) TMS coil geometry
 ii) Individual brain and head anatomy of the stimulated tissues
 iii) Coil position and orientation during stimulation
 iv) TMS pulse information

i) Models for most of the commercially available TMS coils are freely available (Drakaki
et al., 2021; Deng et al., 2013). These coil models are often realized as magnetic
dipole models to precisely cover the model-specific properties (cf. Ravazzani et
al., 1996). See Figure 2.2 for an exemplary coil dipole model. In short, the coil is
discretized into subregions, and a dipole is placed in each subregion, weighted by

the subregion size and the enclosed current (Thielscher & Kammer, 2002; Saturnino, Puonti, et al., 2019). Already about 200 magnetic dipoles suffice to yield a high e-field accuracy (Gomez et al., 2020).

ii) While spherical head models have been used until recently (Nummenmaa et al., 2013), state-of-the-art approaches include the individual head anatomy (Thielscher et al., 2015). By this, the tissue-specific conductivities and anisotropy from fiber bundles can be individually addressed to yield realistic estimations of the induced e-fields (Thielscher et al., 2011; Saturnino, Thielscher, et al., 2019). Based on structural MR images, the subject's head is segmented into several tissue types, from five (*headreco*; Nielsen et al., 2018) to fifteen (*charm*; Puonti et al., 2020) tissue types. See chapter 3 and chapter 4 for details on the imaging sequences used in this work. Here, the toolbox SimNIBS (www.simnibs.org; Saturnino, Madsen, & Thielscher, 2019; Thielscher et al., 2015) has been used, both for segmentation and calculation of the induced e-fields via the finite element method (FEM). Other approaches to numerically determine the induced e-field exist, including the boundary element method (BEM) and the finite difference method (FDM), and are not covered here. Based on the segmentation information, a high-resolution, three-dimensional mesh is constructed (the *head model*, Figure 2.1) to discretize the computation of the electromagnetic fields via FEM. In the utilized software versions (3.1, 3.2.5, 4.0a), the solver uses FEM with superconvergent patch recovery (Zienkiewicz & Zhu, 1992) to determine the e-fields. Throughout the work presented here, individual head models were constructed for five different tissue types with the following conductivities: $\sigma_{scalp} = 0.465\,\mathrm{S\,m^{-1}}$, $\sigma_{skull} = 0.001\,\mathrm{S\,m^{-1}}$, $\sigma_{GM} = 0.275\,\mathrm{S\,m^{-1}}$, $\sigma_{WM} = 0.126\,\mathrm{S\,m^{-1}}$, $\sigma_{CSF} = 1.654\,\mathrm{S\,m^{-1}}$, in line with Thielscher et al. (2011) and Wagner et al. (2004).

iii) During stimulation, the TMS coil and the subject's head is tracked via an online tracking system (*neuronavigation* system; Ruohonen & Karhu, 2010). The tracking allows both, the precise approach of precomputed coil positions/orientations (*prospective e-field calculations*; Zmeykina et al., 2020), and the recording of coil positions and orientations for post-hoc e-field computations (*retrospective e-field calculations*; Kuhnke et al., 2017). The subject's head is co-registered to their individual structural MRI scan. Subsequently, the structural scan and the head model are co-registered as well if they don't share the same spacial alignment,

allowing the transition from one coordinate space to another.

iv) TMS e-field calculations can be separated into a spatial and a temporal dimension: This enables computation of the e-field for only the spatial information (coil model and its position and orientation) and subsequently incorporate pulse and intensity information, given by $\frac{\triangle I(t)}{\triangle t}$ (Saturnino, Madsen, & Thielscher, 2019).

By integrating these four information sources, the induced e-field can be computed for any coil position and orientation: The primary e-field E_{prim} is determined by the coil's magnetic field. In this work, it was pre-computed once in terms of the magnetic vector potential A and mapped to the FEM mesh for each coil position and orientation to speed up the calculations. Accordingly, the primary e-field is given by $-\frac{\triangle A}{\triangle t}$, which is $E_{prim} = -j\omega A$ in the frequency domain after Fourier transformation, where $\omega = 2\pi f$ is the angular frequency of the bi-phasic TMS pulse. The electric potential ϕ in the mesh nodes was calculated by solving the Laplace equation $\nabla \cdot ([\sigma]\nabla\phi) = 0$ using FEM, considering anisotropic conductivity tensors $[\sigma]$ inside each element together with the boundary conditions given by the law of current conservation $\nabla \cdot J = -[\sigma]\nabla(j\omega A + \nabla\phi) = 0$. After calculating the secondary e-field $E_{sec} = -\nabla\phi$, the total induced e-field is given by $E = E_{prim} + E_{sec} = -j\omega A - \nabla\phi$. See Windhoff, Opitz, and Thielscher (2013, Supplemental Material) and Saturnino, Madsen, and Thielscher (2019) for details of the FEM solver.

2.4 Current challenges of TMS

The huge potential of TMS is – currently – impeded by the high variability of the individual stimulation responses (Sasaki et al., 2018), reducing effect sizes and hampering straightforward interpretations on the group- and on the subject-level alike. Besides several other factors, for example, state-dependency of neuronal circuits (Bergmann et al., 2012), two main factors drive this variability:

i) The currently applied TMS dosing strategy does not yield consistent cortical stimulation intensities across brain regions and subjects.

ii) The currently applied TMS targeting does – at least in the cognitive domain – not safely identify the correct individual cortical targets.
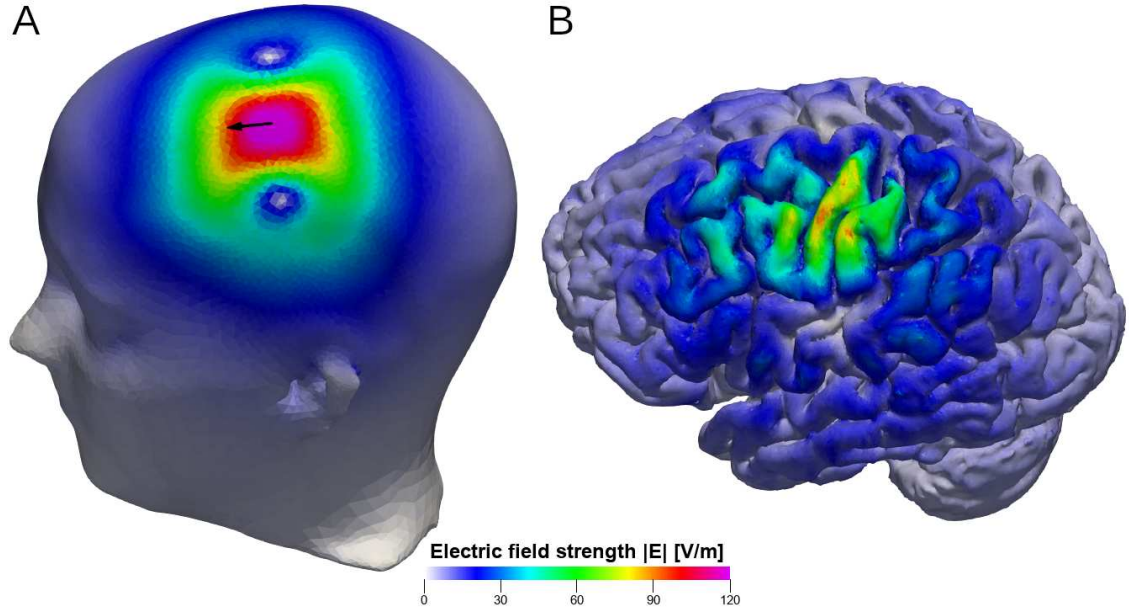
Figure 2.3: Realistic e-field calculation for M1 stimulation. A) Electric field magnitude $|E|$ on the skin surface. Black arrow: TMS coil direction. The figure-of-eight shape of the TMS coil (here: MagVenture MCB-F65) is clearly visible, yielding a field peak under the center of the coil. E-field discretization is based on the head model resolution (here: $\sim 1.3 * 10^6$ triangles). B) Electric field magnitude from the same simulation as A) $|E|$ on the gray matter surface. The steep decline of $|E|$ over the distance to the coil leads to stronger stimulation exposure of superficial cortical regions. The induced e-field is highly autocorrelated. The head model construction and simulation were done with SimNIBS 4.0 for 50 %MSO. The TMS coil was placed above the left M1 region.

i) Current TMS dosing strategies (see subsection 2.3.1 & subsection 2.3.2) rely on the motor threshold (MT): The minimum stimulator intensity to yield MEPs at M1 is used to stimulate the target brain region outside of the motor system as a heuristic to standardize stimulation exposure across subjects (see subsubsection 2.3.1.3). However, due to differences in gyrification and head anatomy, the same stimulat*or* intensity yields significantly different stimulat*ion* intensities across the cortex within a single subject. Adding to this, rTMS effects like facilitation and inhibition are known to be stimulation intensity-dependent – the same TMS protocol applied to the same subject and target may yield opposite effects for different stimulation intensities (Sasaki et al., 2018). Thus, a physiologically plausible dosing metric would not standardize the stimulat*or* intensity but the cortical stimulat*ion* intensity based on an individual cortical e-field threshold.

ii) TMS targets for higher cognition are often based on correlative, group-level results, and thus potentially missing the individual cortical representation (see subsection 2.3.4). In general, current experimental designs do not locate cortical regions involved in a cognitive task on the individual level.

Together, TMS studies of higher cognition cannot validly differentiate between null-results stemming from a suboptimal target selection, from over- or understimulation due to poor TMS dosing, or due to a genuine, non-involvement of the cortical region of interest in the task processing. In summary, a dosing metric that relies on the underlying mode of action of TMS, the induced e-field on the individual level, is currently lacking. To assess this cortical stimulation threshold, for example, for M1 neurons eliciting MEPs from a specific muscle, precise localization of this muscle's representation is inevitable. An individual mapping technique to allow mappings of cognitive function on the individual level would add significantly to the NIBS field and to neuroscience in its entirety.

CONDITION I

CONDITION 2

CONDITION N

MEP [MV]

STIMULATOR INTENSITY [% MSO]

THE CONGRUENCE FACTOR

$\Delta E_{2,I}$

$\Delta E_{N,I}$

MEP [MV]

E [V/M]
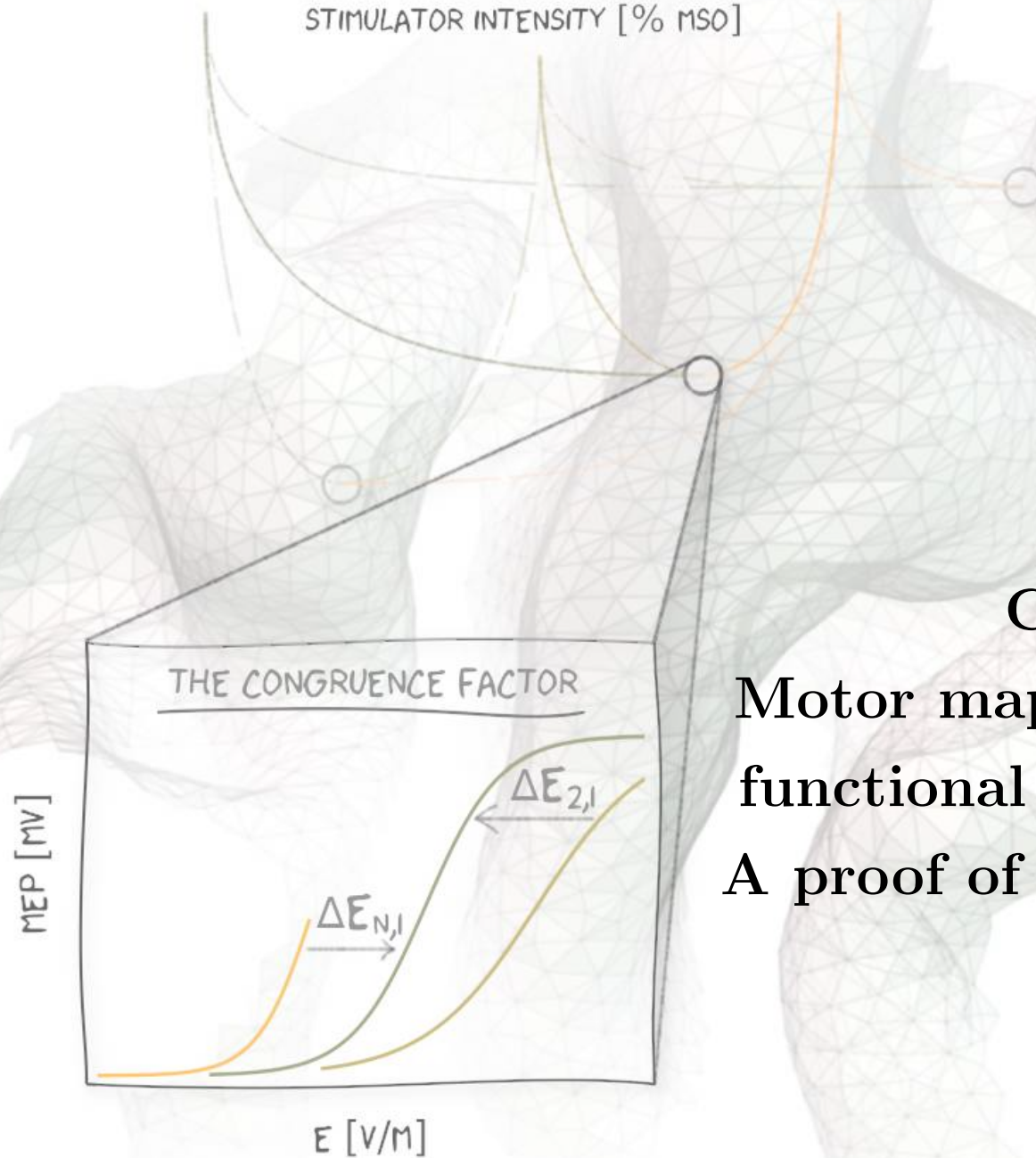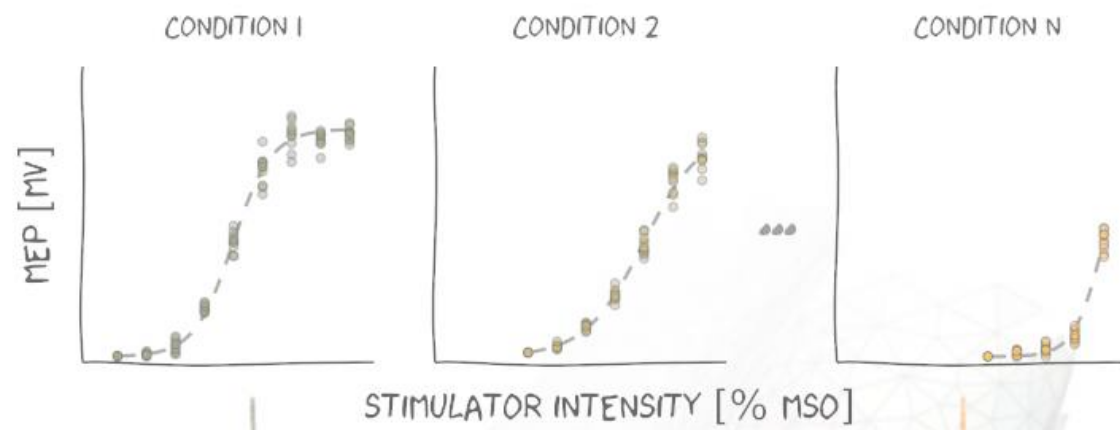
Chapter 3
Motor mapping via functional analyses: A proof of principle

3.1 Overview

In this chapter, I present a first approach to map functions to cortical locations by linking TMS-induced e-fields to an evoked response. First, I outline the rationale of the mapping approach and place it within the existing literature (section 3.2). Second, I introduce a novel metric (section 3.3) to quantify relationships between cortical stimulation exposure and the physiological effect: the *congruence factor*. Locations with high congruence likely house the neural populations linked to the observed MEP. Third, the experimental design to elicit and measure MEPs (section 3.4) and the methodological prerequisites are described. This section involves individual head- and TMS coil models and the differential equations to determine the electric e-fields at the cortex. The congruence factor is then applied to experimental data from 15 healthy subjects in the fourth part (section 3.5) to locate muscle representations in M1 individually. Subsequently, a validation experiment was carried out to thoroughly put the mapping approach to the test (section 3.6).
This chapter closes with a critical evaluation (section 3.7) of the proposed mapping approach to identify unique contributions and potential future improvements.

3.2 Introduction

TMS exposes large parts of the cortex to a complex, subject-specific e-field, rendering the identification of structure-function relationships based on TMS-evoked responses non-trivial. Only recent methodological advances have allowed computing these unfocal e-fields in a realistic and fine-grained manner, allowing to objectively quantify the electrical stimulation of the cortex for any given stimulation site and subject. MEPs scale with stimulation exposure (see subsubsection 2.2.3.1), i.e., MEPs scale with the excitation of the cortical neurons driving the MEPs. Hence, the functional relation $f(E) = MEP$ between the e-field at this specific cortical location and the MEP amplitude is independent of the TMS coil position/orientations (experimental *conditions*) that generated the e-field. Together, the cortical origins of the MEPs can be identified by testing for this stability across stimulation conditions.
Similar rationales have been applied previously, although these implementations

have been considerably restricted. Bungert et al. (2016) tried to locate muscle representations in M1 utilizing the motor threshold (MT) assessed with different TMS coil orientations. Similarly, Laakso et al. (2018) conducted MEP studies with different TMS coil positions and a single coil orientation. Both studies follow a similar rationale to identify cortical origins of TMS-evoked responses via the relationship between cortical field exposure and observed response. However, they remain restricted in several relevant aspects. First, all analyses were performed on the group-level, whereas the functional organization of M1 significantly varies across subjects. Second, it remains unbeknownst how many coil positions/orientations suffice to yield correct localization results; in addition, no selection criteria for coil positions/orientations have been provided. Third, neither study validated the localization results. Finally, the restriction to change the coil positions or the coil orientations potentially led to undersampling of the parameter space.

The approach presented here significantly advances these earlier implementations: i) Information from both, coil position and coil orientation, is exploited. ii) The entire input-output curve (I/O curve) between e-field and MEP (see Figure 3.2) across a wide range of cortical stimulation strengths is used to quantify the relationship between stimulation and response. iii) Cortical localization is possible on the single-subject-level to assess individual structure-function relationships.

So far, knowledge about the specific neuronal structures effectively targeted by TMS, including insights about the driving e-field component, is very limited. Accordingly, the e-field magnitude $|E|$, the e-field's normal component $E_\perp$, and the e-field's tangential component $E_\parallel$ were tested against each other.

3.3 Cortical localization via the congruence factor

This novel cortical mapping concept (see Figure 3.1) is based on three assumptions:

i) a function $f(E) = MEP$ describes the relationship between a component of the e-field and the TMS-evoked motor response (MEP amplitude) for any given muscle at its M1-muscle representation (Weise et al., 2020; Goetz et al., 2019);

ii) the same local e-field vector can be achieved with the combination of different TMS coil position, orientations, and stimulator intensities;
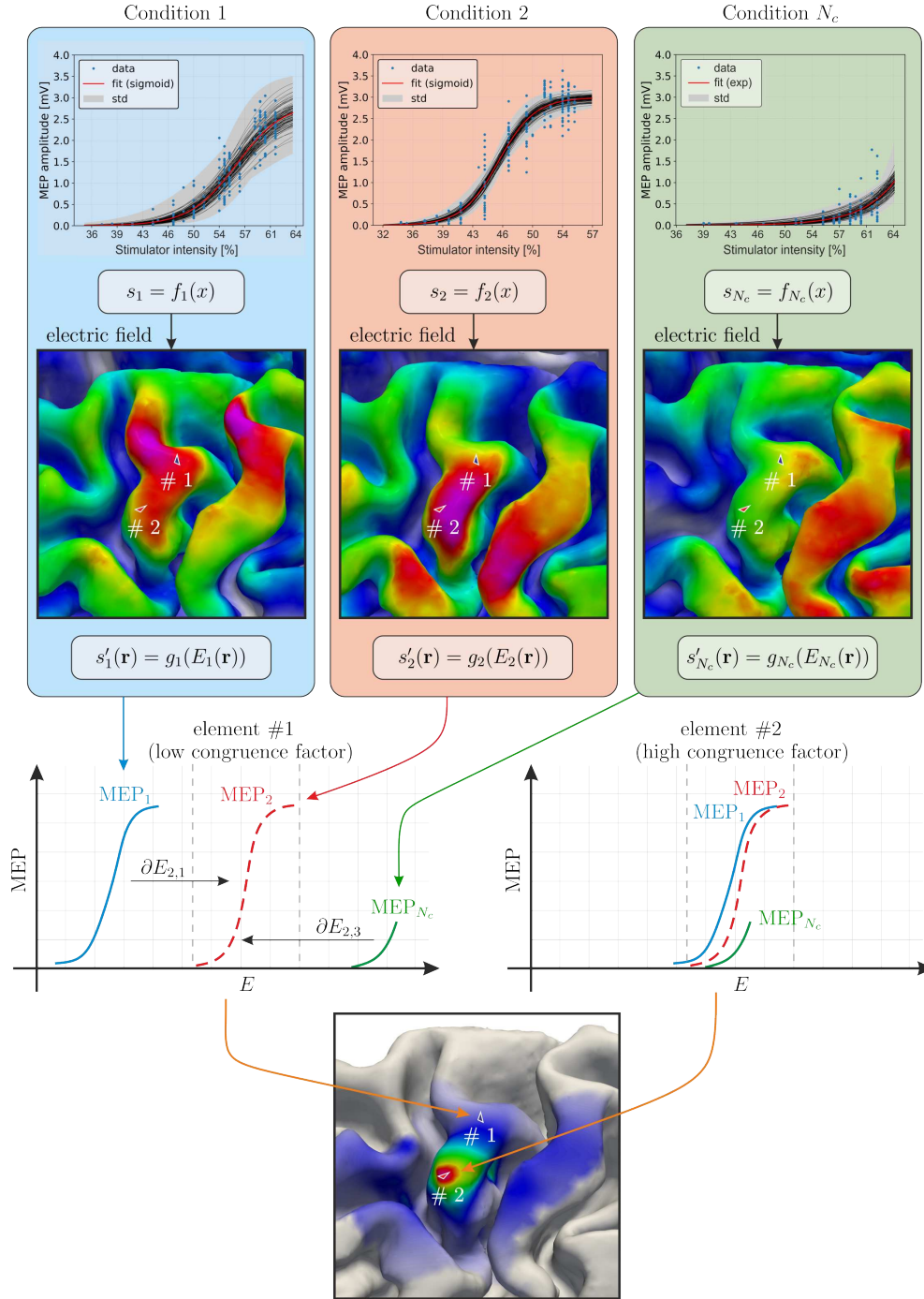
Figure 3.1: Pinpointing cortical muscle representations with TMS. The congruence factor exploits a stable relationship between cortical e-field and motor evoked potential (MEP) for all stimulation conditions at the cortical MEP origin. I/O curves are transformed to element-wise E–MEP-curves using e-field modeling (see text). The element-wise congruence factor quantifies the shift necessary to maximally overlap all E–MEP-curves. Figure published initially in Weise & Numssen et al. (2020).

iii) only one cortical representation per muscle exists in M1 and can be targeted by TMS (Aberra et al., 2020; Siebner, 2020).

With these assumptions, the cortical site effective stimulation can be pinpointed via *cortical I/O curves*. These I/O curves relate the local e-field within the cortex to the measured MEP and can be computed for each part (e.g., *voxel*) of the brain. Here, I/O curves were assessed for a set of coil positions and rotations, where each I/O curve was computed from a wide range of stimulator – and accordingly – stimulation intensities (Figure 3.2, upper part). These measured I/O curves, relating stimulator intensity to MEP amplitude, were transformed to E-MEP curves, i.e., *cortical I/O curves* relating the e-field at a single cortical location to MEP amplitude. This transformation into the E-MEP space equals a transition from stimulat*or* intensity to cortical stimulat*ion* intensity (Figure 3.2, middle part). At the true cortical MEPs origin, only the local e-field is relevant to determine the MEP amplitude (assumptions i & ii). Therefore, all cortical I/O curves are expected to show the same relationship (e.g., slope) at the true cortical origin (assumption iii). Due to the spatial autocorrelation of TMS-induced fields (see Figure 2.3), neighboring cortical elements will show similar but reduced levels of congruency between I/O curves. Each cortical I/O curve can be fitted via various function types. For example, a fully sampled I/O curve would follow a sigmoidal shape, whereas sampling only the left half of the function would yield an exponential shape.

The e-field distribution throughout the brain was computed as a function of %MSO (maximum stimulator output) using the numerical techniques described below, setting $100\,\%$MSO to a change of the coil current of 143 A/µs for the specific stimulator-coil combination. Due to the local linear relationship between the e-field strength and stimulator intensity, the E-MEP curves were shifted and scaled versions of the measured I/O curve, with different shift and scale parameters for each coil position. Hence, the function types of each I/O curve and their corresponding E–MEP curves are similar (i.e., sigmoidal, exponential, or linear). E-MEP curves can be determined for all components of the e-field vector ($|E|$, $E_\perp$, $E_\parallel$) or, in principle, any other derived quantities thereof. Here, sigmoidal functions fitted in a least-square sense:

$$s_i(x) = \frac{a_i}{1 + e^{-b_i(x - x_{0,i})}} \qquad\qquad (3.1)$$

where:

a_i = saturation amplitude,

b_i = slope,

$x_{0,i}$ = turning point.

If only a part of the I/O curve could be determined experimentally, a sigmoidal function could not be reliably fitted, and an exponential or linear function was used instead. Optimal model selection was performed using the Akaike information criterion (AIC; Akaike, 1974). This allows the computation of a position-wise *congruence factor* $c(r)$, which quantifies the similarity between the E-MEP curves of the different experimental conditions (Figure 3.2, bottom part). The agreement between different I/O curves was quantified by computing the inverse variance of the optimal shifts τ_i with $i = 1 \dots N_c$ of the N_c I/O curves across the experimental conditions:

$$c(r) = \left(\frac{1}{N_c} \sum_{i=2}^{N_c} \frac{(\tau_1(r) - \tau_i(r))^2}{\bar{E}^2(r)} \right)^{-1} \qquad \text{Congruence factor (3.2)}$$

where:

N_c = total number of curves,

r = cortical position / cortical element,

τ = optimal shift,

$\bar{E}(r)$ = average e-field quantity at location r.

The congruence factor $c(r)$ was calculated for each element in the cortical region of interest (ROI) by determining the inverted variance of the τ_i, additionally weighted by the averaged, squared $|E|$ (or $E_\perp$, or $E_\parallel$) at this location: $\bar{E}^2(r)$. Hence, the congruence factor quantifies a relative similarity between the E-MEP relationships of

the different experimental conditions, independent of the scale of the e-field. Higher similarity between curves leads to higher inverse variance. The optimal shifts τ_i were obtained by determining the individual locations where the overlap against a reference curve, e.g., the first E-MEP curve, is maximized, see Appendix A, Listing A.1.

As a result, the problem of determining the congruence factor turns into many optimization problems calculating the shifts τ_i for each condition and in each element in the ROI:

$$min_{\tau_i}||S_{REF}(E(r)) - S_i(E(r) - \tau_i)|| \tag{3.3}$$

where:
S_{REF} = reference curve,
S_i = I/O curve to compute τ_i for.

This method is very generic due to its independence of the function type used to fit the I/O curves.

3.4 Materials and methods

3.4.1 Subjects

Fifteen healthy, right-handed participants (seven female, age 22 to 34 years) with an average laterality quotient of 92.93 LQ ± 10.66 LQ according to the Edinburgh Handedness Inventory (Oldfield, 1971) were recruited. Subject inclusion was in accordance with the published safety guidelines for TMS studies (Rossi et al., 2009; Rossini et al., 2015). Written informed consent was obtained from all participants prior to the examination. The study was performed according to the guidelines of the Declaration of Helsinki and approved by the local Ethics committee of the Medical Faculty of the University of Leipzig. TMS pulses were applied with a MagPro X100 stimulator (MagVenture, firmware Version 7.1.1) and CB-60 figure-of-eight coils, guided by a neuronavigation system (software: Localite, Germany, Sankt Augustin; camera: Polaris Spectra, NDI, Canada, Waterloo).

3.4.2 Hardware setup

See Figure 3.2 for the experimental setup. MEPs were recorded from the subjects'
right index finger with one surface electrode positioned over the first *dorsal in-
terosseous* (FDI) muscle belly and one at the proximal interphalangeal (PIP) joint.
The electrodes were connected to a patient amplifier system (D-360, Digitimer Ltd.,
UK, Welwyn Garden City; bandpass filtered from 10 Hz to 2 kHz), which was con-
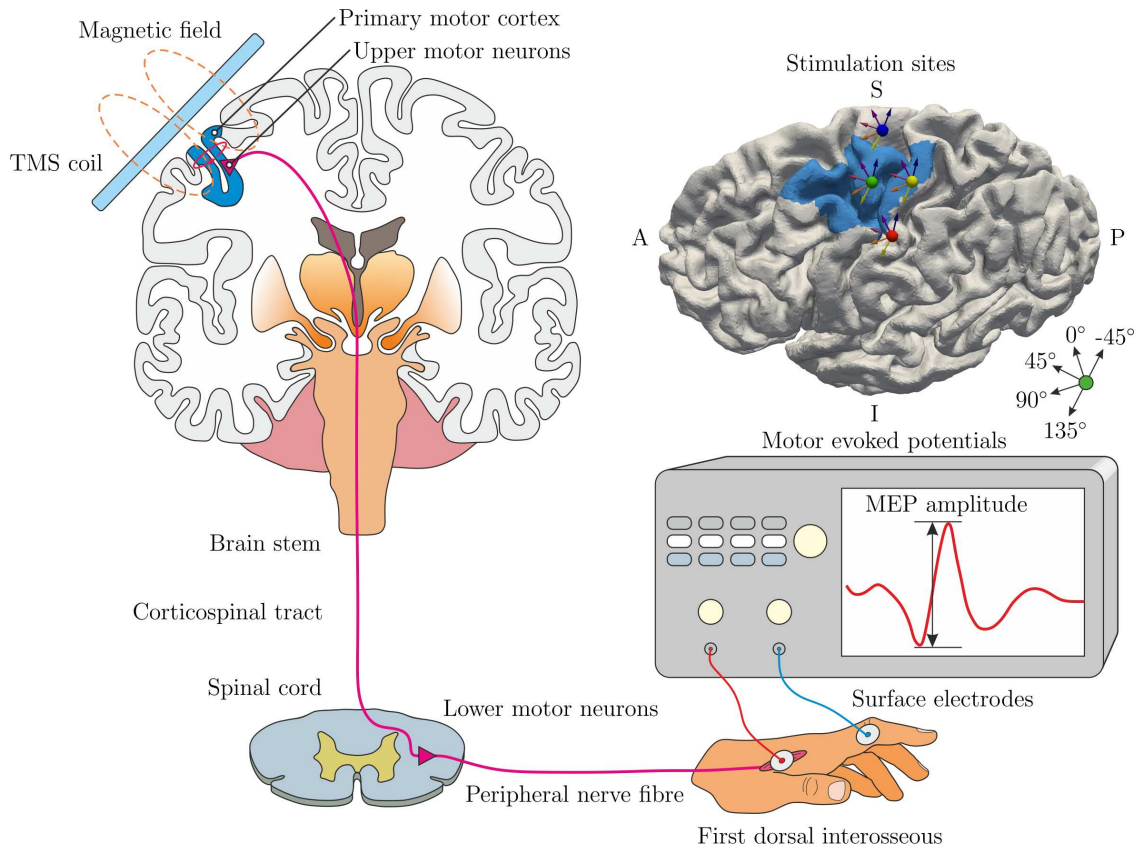
Figure 3.2: Experimental procedure of the TMS MEP experiments. Top left:
The TMS coil is positioned on the scalp over the primary motor cortex (M1). A time-
varying current in the coil generates a time-varying magnetic field, inducing an e-field in the
subject's head and brain. This e-field depolarizes upper motor neurons with corticospinal
efferents. Bottom: action potentials (APs) from upper motor neurons excite lower motor
neurons in the spinal cord and subsequently APs in the first *dorsal interosseous* (FDI) hand
muscle. Sum potentials (motor evoked potentials (MEPs), MEPs) are recorded using a
classical belly tendon montage. Top right: exemplary cortical surface with region of interest
(blue), with the coil positions (spheres) and orientations (arrows) for 20 experimental
conditions. Figure published initially in Weise & Numssen et al. (2020).
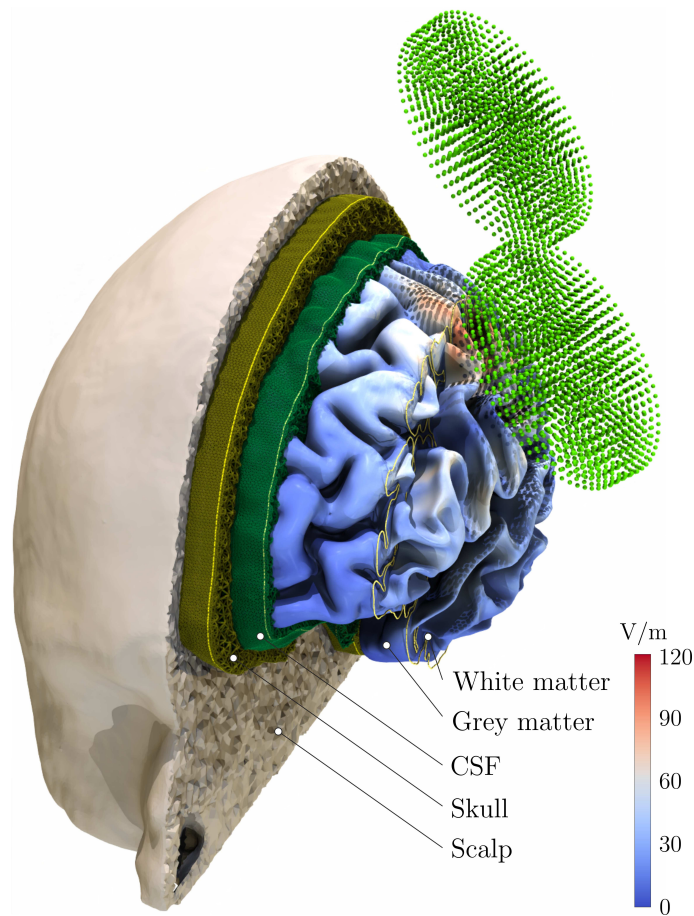
Figure 3.3: Individual head model to compute TMS-induced e-fields. This high-resolution head model consists of $1.26 * 10^6$ nodes and 7.12^6 tetrahedra elements and is based on structural MRI scans. The TMS coil is modeled using 4440 magnetic dipoles (green spheres) with optimized dipole moments positioned in five layers. The gray matter surface is color coded with the magnitude of the induced e-field at a realistic stimulation intensity (60 %MSO). Figure published initially in Weise & Numssen et al. (2020).

nected to a data acquisition interface (Power1401 MK-II, CED Ltd., UK, Cambridge, 4 kHz sampling rate). Electromyography recording was performed with Signal (CED Ltd., version 4.11).

3.4.3 Numerical simulations of the induced e-field

The calculations of the e-field were conducted with SimNIBS v3.0 (Thielscher et al., 2015) using high-resolution anisotropic finite element method (FEM). An exemplary head model is shown for one subject in Figure 3.3.

The individual head models were generated from MRI data using the pipeline described elsewhere (Windhoff et al., 2013), employing FreeSurfer (Dale et al., 1999; Fischl et al., 1999, surfer.nmr.mgh.harvard.edu) and FSL (Woolrich et al., 2009; Smith et al., 2004; Jenkinson et al., 2012, fsl.fmrib.ox.ac.uk/fsl/fslwiki/FSL). The head models were composed of $\sim 1.3 * 10^6$ nodes and $\sim 7 * 10^6$ tetrahedra with an average volume of $0.28 \, \text{mm}^3$ in the cortex. T1 and T2 images were used for segmenting the main tissues of the head: scalp, skull, gray matter (GM), white matter (WM), and corticospinal fluid (CSF). Diffusion-weighted images were used to reconstruct the conductivity tensors in the WM using the volume-normalized mapping approach (Güllmar et al., 2010).

To this end, the following structural images were acquired with a 3 Tesla MRI scanner (Siemens Verio or Skyra) and a 32 channel head coil:

i) T1-weighted: MPRAGE with 176 sagittal slices, matrix size = 256 x 240,
   voxel size = 1 x 1 x 1 mm^3, flip angle 9°,
   TR/TE/TI = 2300/2.98/900 ms (Repetition Time, Spin echo, Inversion Time).

ii) T2-weighted: 192 sagittal slices, matrix size = 256 x 258,
    voxel size = 0.488 x 0.488 x 1 mm^3, flip angle 120°,
    TR/TE = 5000/395 ms.

iii) diffusion MRI: 67 axial slices, matrix size 128 x 128,
     voxel size = 1.71875 x 1.71875 x 1.7 mm^3,
     TE/TR 80/7000ms, flip angle 90°,
     67 diffusion directions, b-value = 1000 s/mm^3.

An additional b0 image with reversed encoding direction was acquired and used during calculating the conductivity sensors for eddy current correction and distortion correction.

The T1 image was also used for neuronavigation during TMS. If adequate scans, i.e., with age less than one year, already existed in the in-house image database, these were utilized. All TMS coils were individually modeled by magnetic dipoles based on X-ray images. Differences between left and right wirings of several millimetres and of about 2°–5° were observed and accounted for. Each coil model consisted of 4500 magnetic dipoles in five layers in the coil plane. Their magnitudes were determined from the enclosed current. Details on the e-field modeling are provided in Chapter 2,

subsection 2.3.5.

Individual coil positions and orientations relative to the subject's head were saved by the neuronavigation system for each TMS pulse. Throughout the experiment, the TMS coil touched the subject's scalp, with a small bias due to hair. In some cases, slight distances between the coil and head surface of about $0.5\,\text{mm}$ to $2\,\text{mm}$ were observed and accounted for in the subsequent modeling steps. While stimulating, the center of the TMS coil always touched the head surface to reduce these small errors, presumably caused by inaccuracies in the neuronavigation and the head surface reconstruction. These coil configurations were used for the e-field calculations in SimNIBS. A region of interest (ROI) was defined with FreeSurfer covering the somatosensory cortex, M1, and the dorsal premotor cortex (PMd). The mask was based the FreeSurfer average template and transformed to each subject's brain space.

The following analyses were performed on the midlayer between the outer surfaces of the GM and WM compartments to avoid boundary effects of the e-field due to conductivity discontinuities. The e-field interpolation followed the procedure described in Saturnino, Madsen, and Thielscher (2019) to determine the e-field at the nodes within gray matter and computed the e-field at the gray matter center using linear interpolation. See Figure 3.4 for the magnitude $|E|$, the normal component $E_\perp$, and the magnitude of the tangential component $E_\parallel$ of the e-field at the midlayer surface for three different coil positions and orientations in one exemplary subject. The different e-field distributions are shown in the highlighted ROI for the different experimental conditions.

3.4.4 The sign of the e-field's normal component

The direction of the normal component of the e-field along the pyramidal apical dendrites is likely to influence the activation of the neurons. For a particular voxel, the normal e-field component might point outwards (positive) for some stimulation conditions and inwards (negative) for others. As a consequence, the curves for the negative and positive ranges must be analyzed separately, and their congruencies must be merged afterward. In order to preserve the sign information of the normal component $E_\perp = E * n$, the e-field axis of the I/O curve (Figure 3.1) was extended into the negative domain. In the present study, the more effective posterior-anterior
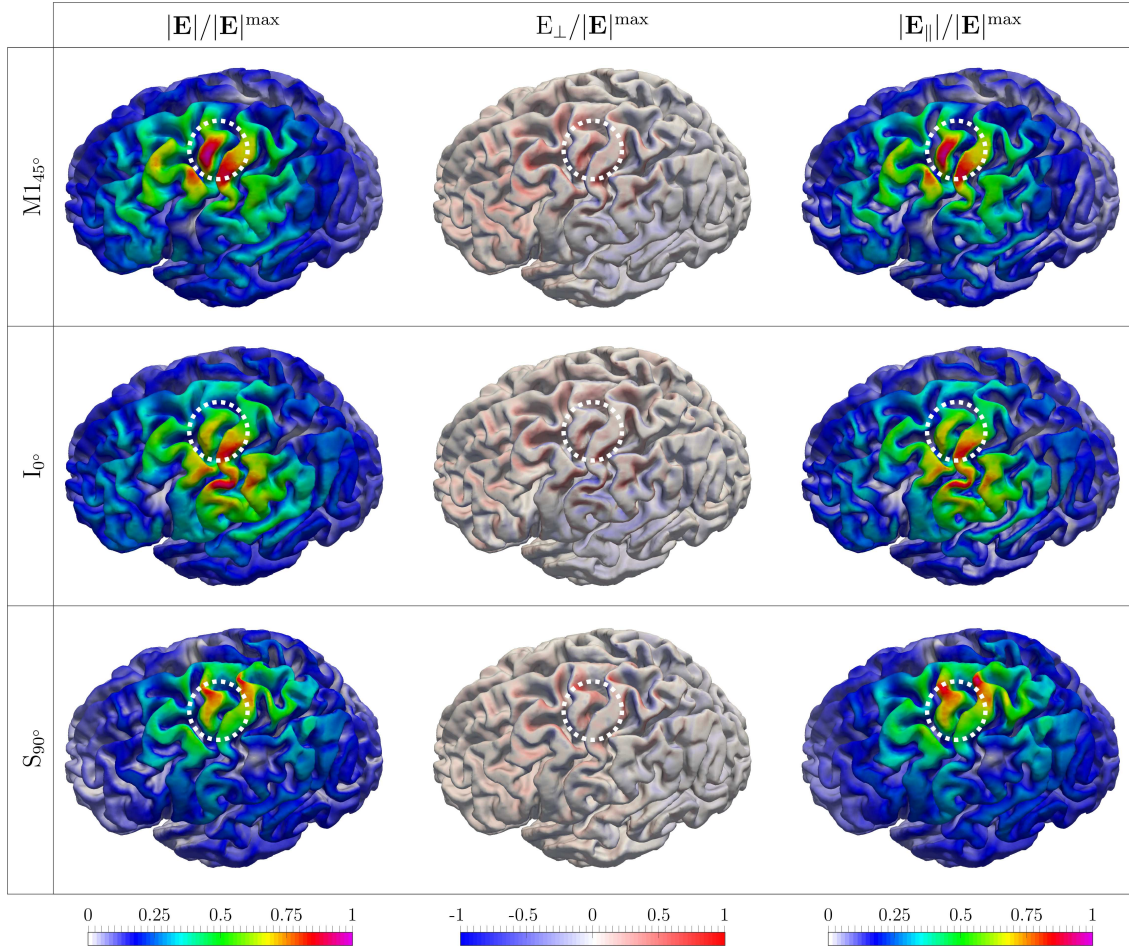
Figure 3.4: The three e-field components yield different spacial profiles. Normalized strengths of e-field components. Left: overall magnitude of the e-field $|E|$; center: normal component $E_{\parallel}$; right: magnitude of the tangential component $E_{\perp}$ for one exemplary subject. Rows: Three different coil positions/orientations (see text). White circle: the hand area of the primary motor cortex ($M1_{hand}$). E-field strengths are normalized across components to facilitate visual comparison of spatial distribution. Figure published initially in Weise & Numssen et al. (2020).

stimulation (PA) direction was used, with the stimulator's current direction never reversed. Therefore, for a particular voxel, $E_{\perp}$ might point outwards (positive) for some conditions and inwards (negative) for others. In consequence, the curves for the negative and positive ranges must be analyzed separately to assess the congruence factor. This differential analysis is illustrated in Figure 3.5 for one cortical element. The congruence factor for $E_{\perp}$ is given by the inverse of the average of the accumulated

squared deviations between both domains (see Equation 3.2):

$$c(r) = \left(\frac{1}{N_c} \left[\sum_{i \in I^-} \frac{(\bar{\tau}^-(r) - \bar{\tau}_i(r))^2}{\bar{E}_-^2(r)} + \sum_{j \in I^+} \frac{(\bar{\tau}^+(r) - \bar{\tau}_j(r))^2}{\bar{E}_+^2(r)} \right] \right)^{-1} \tag{3.4}$$

where:

I^- = I/O-curves in the negative e-field domain,

I^+ = I/O-curves in the positive e-field domain,

$\bar{\tau}^-$ = average τ of fits from I^-,

$\bar{\tau}^+$ = average τ of fits fom I^+.

By separating positive and negative e-field normals neural populations can be located with a direction-dependent response behavior to e-field exposure. This shift approach for the computation of the congruence factor is advantageous if the experimentally determined I/O curves capture only a linear or exponential part of the relationship between the e-field and MEP amplitude.

However, if each E-MEP curve can be represented as an analytical sigmoidal function (eq. 3.1), parameterized by its turning point $X_{0,i}$, the shifts τ_i are directly given by $\tau_i = x_{0,i} E_i(r)$ and the computationally expensive optimization from Equation 3.3 may be replaced by a more efficient one. This approach is advantageous in terms of computational cost and is preferred in the current study if all I/O curves are modeled by sigmoidal functions.

3.4.5 Group-level analyses

To allow insights into the cortical organization on group-level, the individual brain-anatomies have to be transformed into a common space. As the standard FreeSurfer average template (FsAverage) suffers from several malformed elements at M1, each roughly 20 times larger than average elements, I created a study-specific group template with FreeSurfer based on the 15 subjects examined here. In this iterative procedure, a randomly chosen subject was used as the initial template, and all other subjects were registered to this. In the second step, this template was updated based on all registrations. The third step comprised the registration of all subjects to

$$c = \left[\frac{1}{N_c} \left(\overbrace{\sum_{i \in \{1,2,5\}} \left(\frac{\overline{\tau}^- - \tau_i^-}{\overline{E}^-} \right)^2} + \overbrace{\sum_{j \in \{3,4,6\}} \left(\frac{\overline{\tau}^+ - \tau_j^+}{\overline{E}^+} \right)^2} \right) \right]^{-1}$$
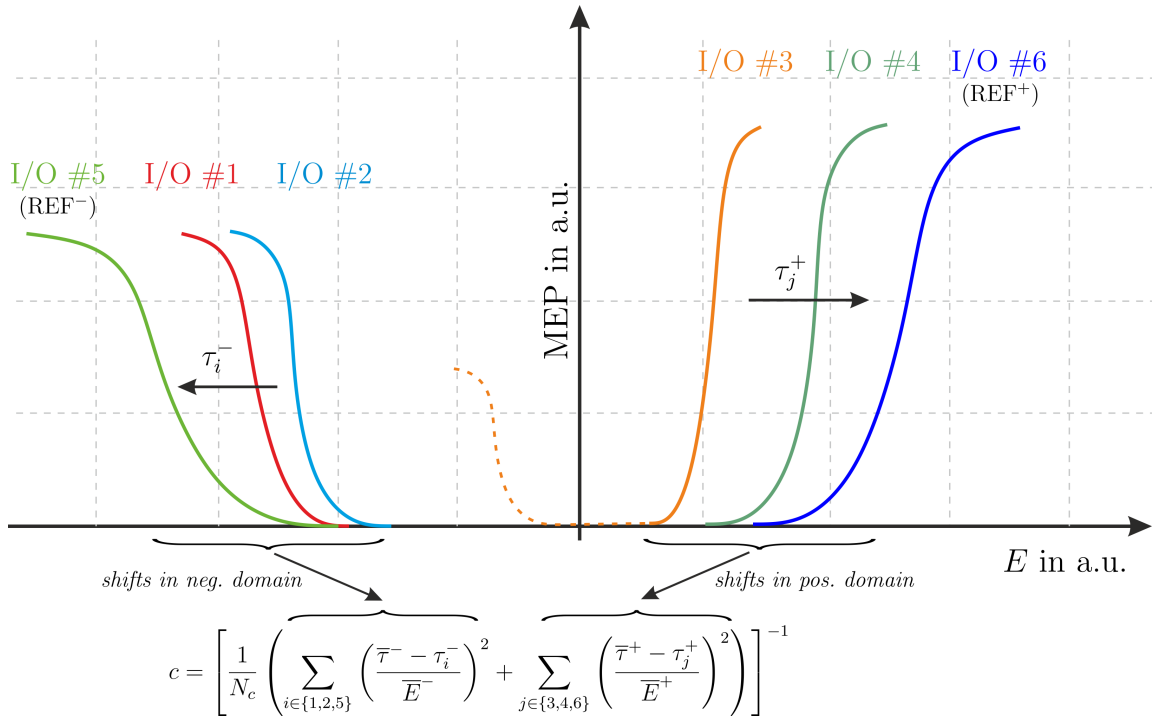
Figure 3.5: For $E_\perp$, the e-field's sign is included in the congruence calculation.
Six exemplary I/O curves are shown in the e-field space for one cortical element. Three
conditions (#1, #2, #5) yield negative, and three (#3, #4, #6) yield positive e-fields in
this particular cortical element. The accumulated squared deviation of the curve shifts is
determined separatedly for negative and positive e-fields (see Figure 3.1). The congruence
factor of the normal component is given by the inverse of the average between both domains.
Figure published initially in Weise & Numssen et al. (2020).

this updated template. The second and third steps were repeated to improve the
template.

3.5 Localization experiments

3.5.1 Data acquisition

Localization of the initial MEP target location was guided by individually trans-
formed M1 coordinates based on the standardized group coordinates from a meta-
analysis (Maykaa et al., 2006). These coordinates were transformed to the individual
subject's space by using the inverse of the normalization transformation in SPM

8 (Penny et al., 2011, www.fil.ion.ucl.ac.uk/spm/). With a standard threshold hunting procedure, rMT was manually approximated, and the corresponding coil position and orientation for each subject. As this coil orientation usually is about 45° towards the fissura longitudinalis, I call this $MT_{45°}$, the corresponding coil configuration $M1_{45°}$, and refer to the coil angle as 45° in the following (Brasil-Neto et al., 1992; Mills et al., 1992). $MT_{45°}$ was defined as the minimum stimulator intensity which evoked MEPs with an amplitude of at least $50\,\mu V$ in at least 5 out of 10 consecutive TMS pulses (Pascual-Leone et al., 1993; Rothwell et al., 1999; Conforto et al., 2004). In relation to $M1_{45°}$, five additional conditions with different coil positions and orientations (see Figure 3.6a,) were defined in the following way. In Experiment I, the TMS coil was positioned over M1 and 2 cm posterior (P). At both sites, three coil orientations with respect to $M1_{45°}$ were investigated, namely $M1_{0°}/P_{0°}$ (−45° from M145°), $M1_{45°}/P_{45°}$, and $M1_{90°}/P_{90°}$ (+45° from $M1_{45°}$), resulting in six experimental conditions.

Experiment II included three of the subjects from Experiment I. The number of conditions was increased to investigate further the influence of different coil positions and orientations on identifying the relevant cortical site. In addition to M1 and P, two more coil positions were included: 2 cm inferior and 2 cm superior to M1, respectively (Figure 3.6b). For each position, the number of coil orientations was increased to 5 (-90°, -45°, 0°, 45°, 90°) with respect to $M1_{45°}$, resulting in 20 experimental conditions.

In both experiments, single bi-phasic pulses with an inter-stimulus interval (ISI) of 5 s (Experiment I) or 4 s (Experiment II) were applied for each condition. The coil positions/orientations were recorded by the neuronavigation system. The MEPs were low-pass filtered with a 6th-order Butterworth filter with a cutoff frequency of 500 Hz. Afterward, the peak-to-peak amplitudes of the MEPs were calculated in a time window of 18 to 35 ms after the TMS pulse (see Figure 3.7a for an example MEP). Stimulator intensities were chosen to sample the complete I/O curve for each experimental condition unless 100 %MSO was reached before (Figure 3.7). The intensity was increased in steps of 2 %MSO or 1 % MSO, respectively, for intensity ranges of high I/O gradients (cf. Bungert et al., 2016). 3–5 TMS pulses were delivered for each intensity to determine an average MEP amplitude. Trials with coil position deviations of more than ±3 mm and orientation of more than ±5° with respect to any

axis were removed. See Figure 3.7b (blue dots) for a typical set of data points. The procedure was repeated in a pseudo-randomized order for all experimental conditions (i.e., for different coil positions and orientations).
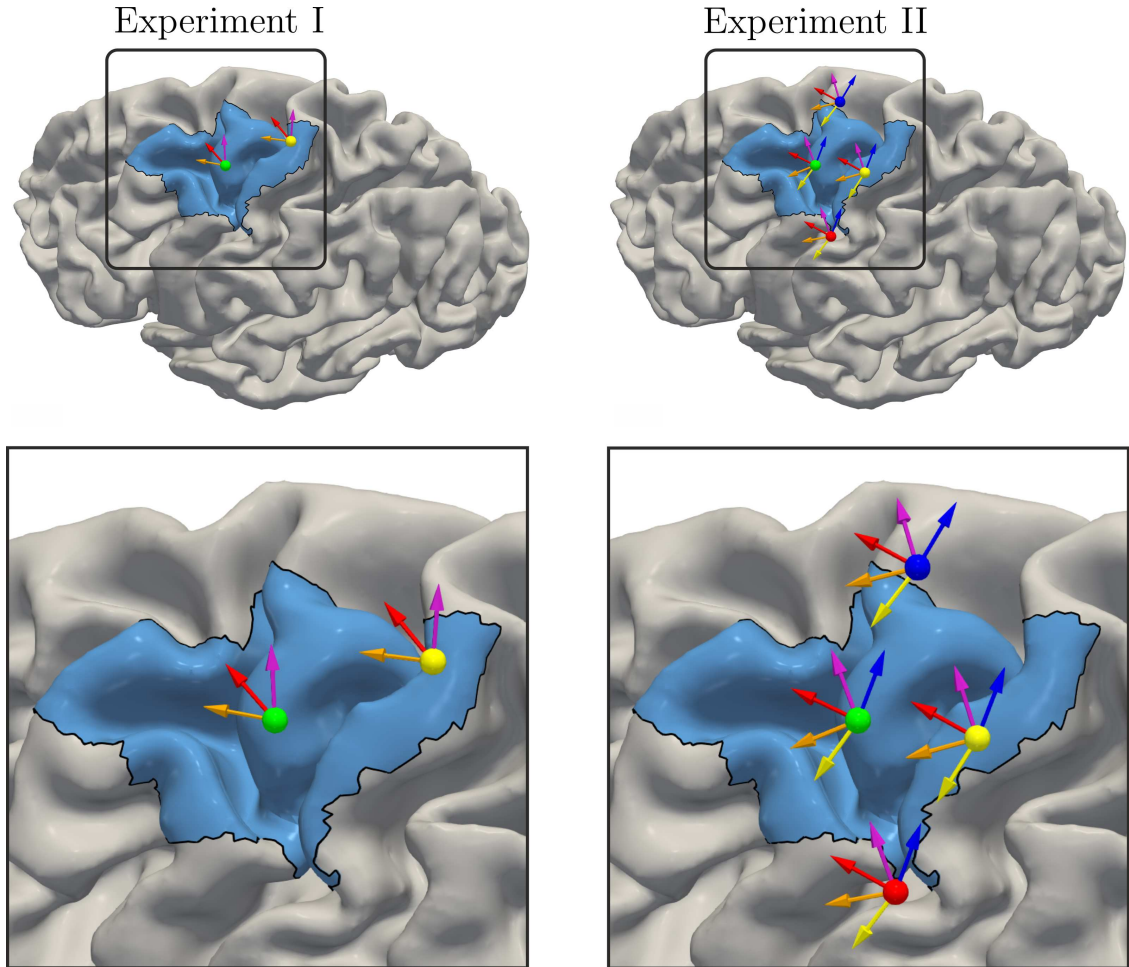
Figure 3.6: Coil positions/orientations used in Experiment I and II. Coil positions/orientations for subject Sub08. In Experiment I (left) two positions and 3 orientations were realized, yielding six experimental conditions. In Experiment II (right) the number of experimental conditions were increased to 20. For each experimental condition an I/O-curve was assessed. Blue area: region of interest, comprising the somatosensory cortex S (BA1, BA3), M1 (BA4), and the dorsal part of the premotor cortex (BA6). Figure published initially in Weise & Numssen et al. (2020).
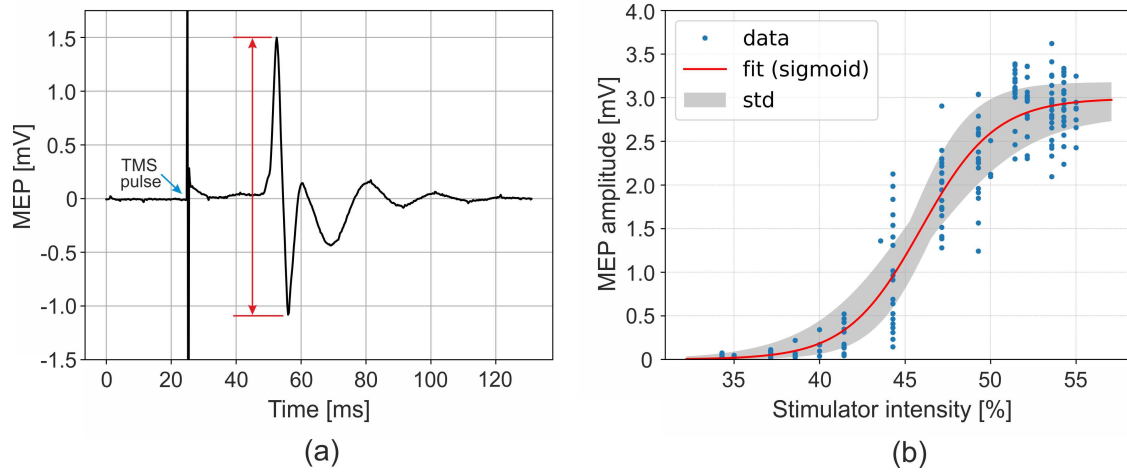
Figure 3.7: I/O-curves are assessed for each experimental condition. (a) electromyography (EMG) data for a single TMS pulse, including the stimulation artifact (blue arrow) and the muscle response. The motor evoked potential (MEP) is quantified via the peak-to-peak amplitude (red arrow) within 35 ms after the TMS pulse. (b) I/O curves characterize MEPs as a function of stimulator intensity for a single experimental condition. Blue dots: MEPs for different stimulator intensities. Red line: fitted analytical function. Depending on the Akaike information criterion (AIC), MEPs were fitted to sigmoid, exponential, or linear functions. Here: sigmoidal fit function. Figure published initially in Weise & Numssen et al. (2020).

3.5.2 Results

Below, I present the results from Experiment I (15 subjects and 6 experimental conditions, subsubsection 3.5.2.1) and Experiment II (3 subjects and 20 experimental conditions, subsubsection 3.5.2.2). The latter includes a permutation analysis to determine the minimum number of TMS conditions, i.e., coil positions and orientations, required to reliably identify the location of the cortical representation of the MEPs. Finally, the predicted cortical activation site were validated for the subjects in Experiment II (subsection 3.6.3) in a subsequent experimental session.

Experiment I (15 subjects, 6 experimental conditions)

An average of 981.6 ± 173.10[1] single pulses were applied per subject (163.6 ± 49.39 per coil position/orientation). Figure 3.9 shows the congruence factors of the group

---

[1]Throughout the thesis, I provide descriptive statistics as *mean $\pm$ standard deviation (SD)* unless noted otherwise.
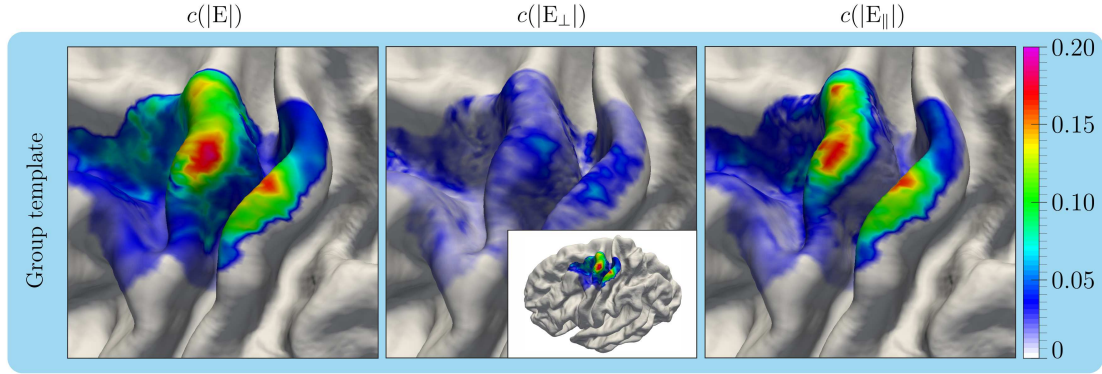
Figure 3.8: $|E|$ **and** $E_\parallel$ **yield congruence factor hotspots on the group-level.**
Congruence factors were calculated for the magnitude ($|E|$), the normal component ($E_\perp$), and the tangential ($E_\parallel$) component. On the group-level only $|E|$ and $E_\parallel$ yielded pronounced congruence factor hotspots. A secondary hotspot on the somatosensory cortex is present. Color: congruence factor. Figure published initially in Weise & Numssen et al. (2020).

average (a) and the 15 individual subjects (b). The e-field distributions of all conditions were determined for each subject and combined with the fitted MEP curves using the optimal curve shift approach because not all MEP curves could be fitted to sigmoidal functions. In 6/15 subjects (marked with an asterisk, *), no I/O curve could be determined for the posterior coil position $P_{0°}$. Hence, the congruence factor was determined using only 5 of the 6 conditions. The congruence factor was calculated for the overall magnitude ($|E|$), the normal component ($E_\perp$), and the tangential component ($E_\parallel$) of the induced e-field. $|E|$ and $E_\parallel$ reached substantially higher congruence factors and smoother spatial distributions than $E_\perp$.

In general, a clear hotspot for $|E|$ and $E_\parallel$ could be identified in the hand knob area of M1 on the gyral crown of the average template (Figure 3.9). In 7/15 subjects (Sub01–Sub07, highlighted in Figure 3.9 in green), clear and unique hotspots were found on the gyral crowns in the hand knob area. In 4/15 subjects (Sub08–Sub11, Figure 3.9, yellow background), a second hotspot was found in the somatosensory cortex. In 4/15 subjects (Sub12–Sub15, Figure 3.9, orange background), a single hotspot in the somatosensory cortex was found. I reasoned these unrealistic localizations in groups 2 and 3 happened due to array ambiguities, i.e., spurious overlaps, of the realized e-fields and the missing I/O curve of condition $P_{0°}$, in 2/4 and 3/4 subjects of the two groups, respectively. Maximum values of the congruence factors substantially differ
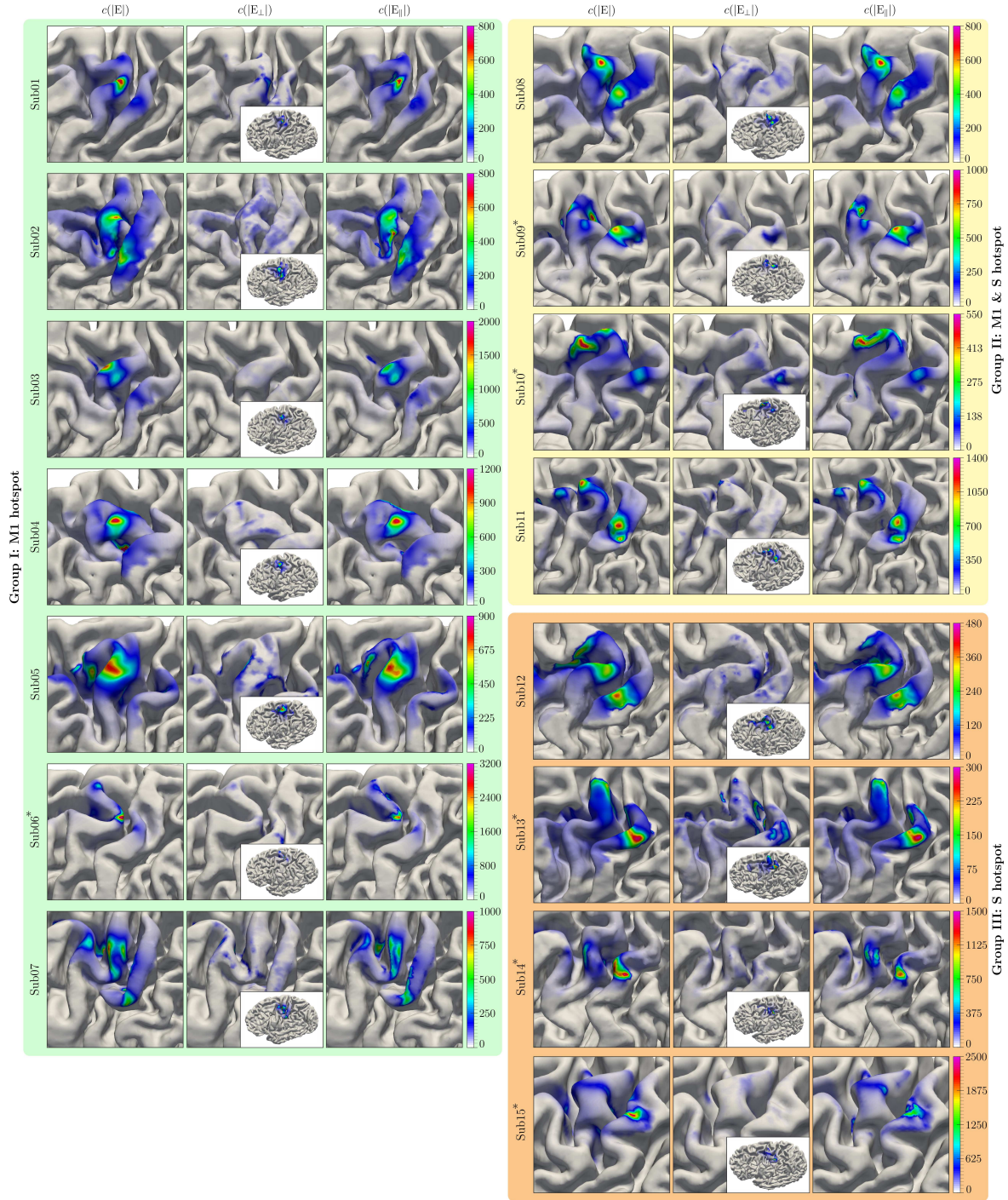
Figure 3.9: Experiment I identified a clear M1 hotspot in 7/15 subjects.
Congruence factors were calculated for the magnitude ($|E|$), the normal component ($E_\perp$), and the tangential ($E_\parallel$) component. 7 subjects show unique hotspots in M1 (green); 4 subjects show hotspots in M1 and the somatosensory cortex (yellow); 4 subjects show hotspots in the somatosensory cortex only (orange). *: no MEPs for condition $P_{0°}$. Color: congruence factor. Figure published initially in Weise & Numssen et al. (2020).

across subjects, most probable because differences in near-zero variances among I/O curves result in large differences of their inverse, that is, the associated congruence factors. I expected that additional experimental conditions, i.e., more coil positions and orientations, improve the results of the congruence factor toward more plausible hotspot locations in the M1 hand knob area.

This hypothesis was investigated in Experiment II with one subject from each results group (Sub01, Sub08, and Sub12) by increasing the number of coil positions and orientations from 6 (respectively 5) to 20 (see Figure 3.9 b).

Experiment II (3 subjects, 20 experimental conditions)

This experiment was conducted with an extended set of coil positions and orientations (Figure 3.6 b). For each subject, 20 e-field profiles were calculated and combined with the obtained MEP curves to determine the congruence factor maps. An average of 1831.3 ± 300.52 single pulses were applied per subject (85.84 ± 17.19 per condition). In this experiment, all I/O curves could be fitted to sigmoidal functions, which avoids the computationally expensive optimization step from Equation 3.3 by directly using the variance of the turning points. Applying 2000 single pulses with $4\,\mathrm{s}$ ISI alone takes about 2.5 hours; additional time for subject preparation, changing the coil position and orientation, potential pauses due to coil heating, rest periods for the subject, etc., may lead to experiment durations of 5 hours or more. Since this would not be feasible in everyday (clinical) applications, I investigated how the congruence factor convergences depending on the number of experimental conditions. This convergence study enabled me to determine an optimal number and selection of coil positions/orientations to reduce the experimental effort.

3.5.3 Permutation analysis

Consequently, a permutation study was performed for each subject by determining the congruence factor for all combinations of $k = 2 \dots 20$ available experimental conditions. The total number of considered conditions was $\sum_{k=2}^{20} \binom{20}{k} = 1,048,555$. I quantified the focality of each congruence factor map by determining the area with $c > 30$. This threshold was chosen based on the permutation results to allow comparability between the combinations and subjects. The smaller this area, the

more concentrated the map is. That is, the more uniquely the relationship between e-field and MEP could be determined.

The results of the permutation study are shown in Figure 3.10 for one exemplary subject (Sub01). The results for the remaining subjects were similar (see Appendix B, Figure B.2 – Figure B.3). I expected a lower cross-correlation across the condition-wise e-fields would allow for a higher discriminative power in the determination of the stimulation site. This was confirmed by the analysis in Figure 3.10a, showing a correlation of $r = 0.57; p \ll .001$ between the size of the hotspot area and the cross-correlation of the e-fields over all k.

In addition, the correlation between the resulting hotspot area size and the cross-correlation of the e-fields was stronger for low k (Figure 3.10b, correlation coefficients). The hotspot's median area converges when increasing the number of conditions. Moreover, the spread of the area decreases by adding more information to the congruence factor calculation. Importantly, the smallest areas (lower dashed line in Figure 3.10b) indicate that some condition combinations for ≤ 5 result in similar or even smaller areas than for $k \leq 20$. The existence of these optimal condition combinations suggests that the cortical activation site can be determined with relatively few measurements by selecting optimal coil positions and orientations. The relationship between the cross-correlation of the e-fields and the number of conditions k is shown in Figure 3.10c. Cases resulting in the smallest 5th percentile of the hotspot area are shown as thin lines in the shaded area, corresponding to those shown in Figure 3.10b. As expected, these cases are concentrated in regions of low cross-correlation.

The data was further analyzed to identify which condition combinations were especially informative and produced focal hotspots (Figure 3.10d). This analysis was performed for $k = 6$. The selection of each condition and its co-occurrence with other conditions was accumulated across all condition combinations, which are part of the smallest 5th percentile of the hotspot area (gray shaded area in Figure 3.10b). I found the co-occurrence not to be random and combinations neighboring M1, i.e., inferior, superior, and posterior coil positions, were selected more often than M1 coil positions. The corresponding coil orientations differ considerably and co-occurrences of $S_{90°}$, $S_{135°}$, $I_{45°}$, and $I_{135°}$ stand out. Moreover, posterior conditions occurred more frequently in combination with $S_{90°}$, which further confirms the need for highly varying e-field distributions. This behavior was even more pronounced for
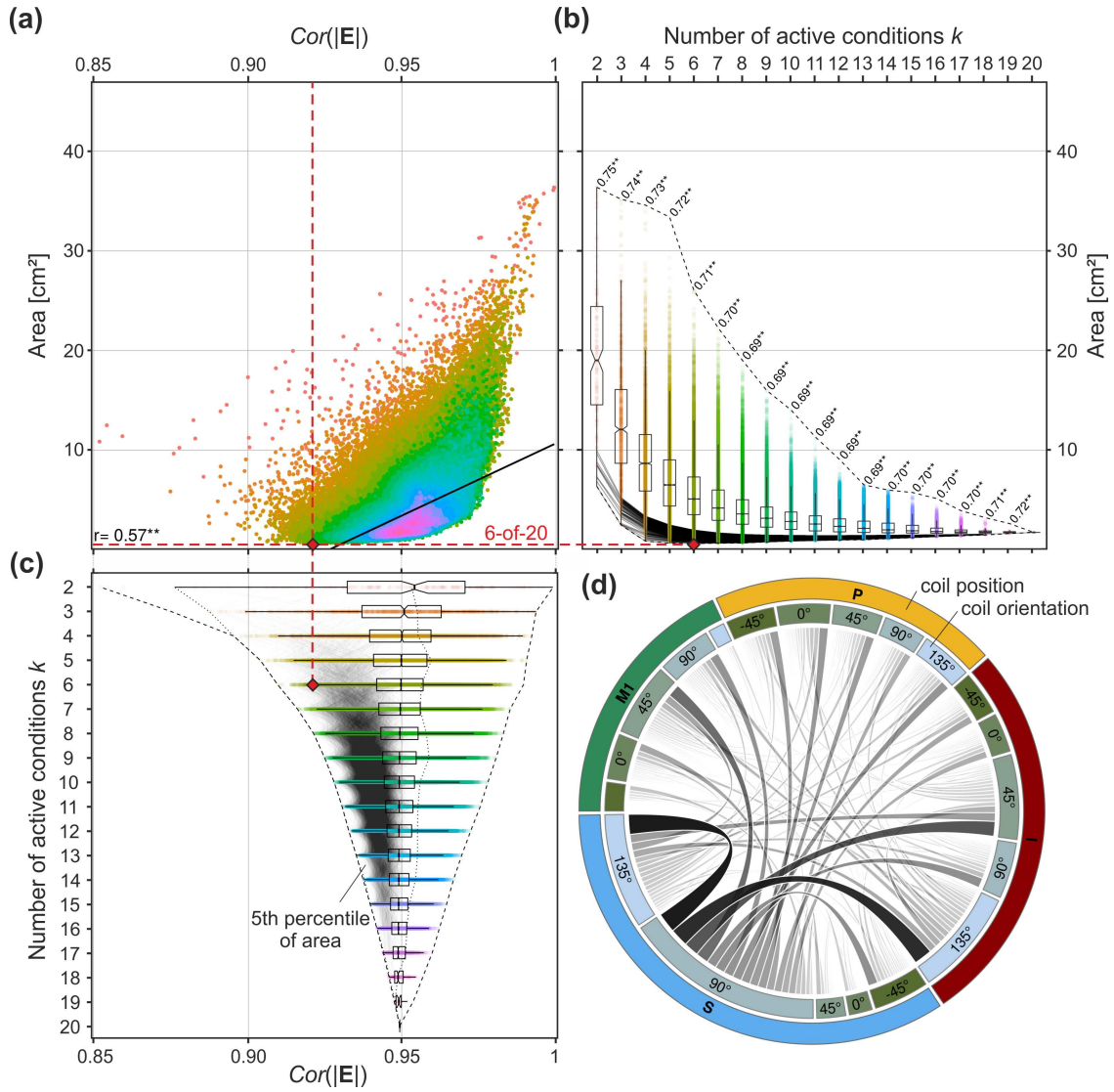
Figure 3.10: De-correlated e-fields yield a better localization (Sub08). The relationship between e-field correlation and localization precision (*hotspot area $c > 30$*) analyzed via permutation analysis. For each $k = 1 \ldots 20$, $\binom{20}{k}$ localizations were determined. Red lines: The six conditions yielding optimal localization. Their cross-correlation $r = 0.921$ is lower than 75 % of all solutions. (a) Cross-correlation of $|E|$ versus hotspot area. Color: Number of conditions k. The correlation between hotspot size and e-field cross-correlation for all $k = 20$ is $r = 0.57$; $p \ll .001$ (black line). (b) Hotspot area of the congruence factor decreases with more conditions k. Boxes: 25 % to 75 % quantiles. Numbers: Correlation between hotspot size and e-field cross-correlation. **: $p < .01$, Bonferroni corrected. Gray lines: 5th percentile of best k. Dashed lines: full results range. (c) Relationship between e-field cross-correlation and number of conditions k. Gray lines: 5th percentile of the best combinations. (d) Pairs of coil positions (outer) and orientations (inner) from 5th percentile of all combinations ($k = 20$) yielding good localization (black lines in (b)). Figure published initially in Weise & Numssen et al. (2020).

subjects Sub08 and Sub12 (see Figure B.2 – Figure B.3).

Next, the condition combination yielding the most precise hotspot ($k = 6$) is described in more detail and compared to Experiment I and the full $k = 20$ result. Applying the method for 6 different coil conditions and orientations is also feasible, as the total experiment duration would not exceed one hour.

3.5.4 Conclusions

The congruence factor map for each subject (Figure 3.11) was normalized with respect to the individual maxima to allow across-subject comparability. For subject Sub01, Experiment I identified a unique hotspot in the M1 hand knob area. Experiment II reproduced this pattern, increased the focality, and reduced deflection on the somatosensory cortex, for the best 6 condition combination (6-of-20). Hence, for this subject, the coil positions of Experiment I were already sufficient to determine the activation site plausibly. The second subject belonged to the group with hotspots in both M1 and the somatosensory cortex (Experiment I). In Experiment II a single hotspot was found, limited to the M1 region, without any deflections in the somatosensory cortex. The M1 hotspot also shifted slightly inferiorly. The third subject belonged to the group showing a hotspot only in the somatosensory cortex in Experiment I. In Experiment II, however, the hotspot moved to M1.

This improvement in localization supports the assumption that the e-field profiles of Experiment I did not cover enough variance to localize the cortical muscle representation successfully. As indicated by the convergence results (Figure 3.10), adding the remaining conditions of Experiment II (20-of-20 case) does not yield any improvement for any of the three subject groups. For subject Sub01 (first row in Figure 3.11), the cross-correlation of the e-field distributions in the ROI was 0.951 for Experiment I, and 0.921 for Experiment II. For subject Sub08 (second row in Figure 3.11), the cross-correlation was 0.953 and 0.925 for Experiment I and II, respectively. The use of less correlating e-field distributions increased the quality of the cortical localization. Finally, for subject Sub12 (third row in Figure 3.11), the cross-correlations were nearly the same, with 0.951 and 0.953 from Experiment I to II, respectively. However, the improvement of the results indicates that the selected coil positions and orientations in Experiment II were more suitable for determining the congruence factor,
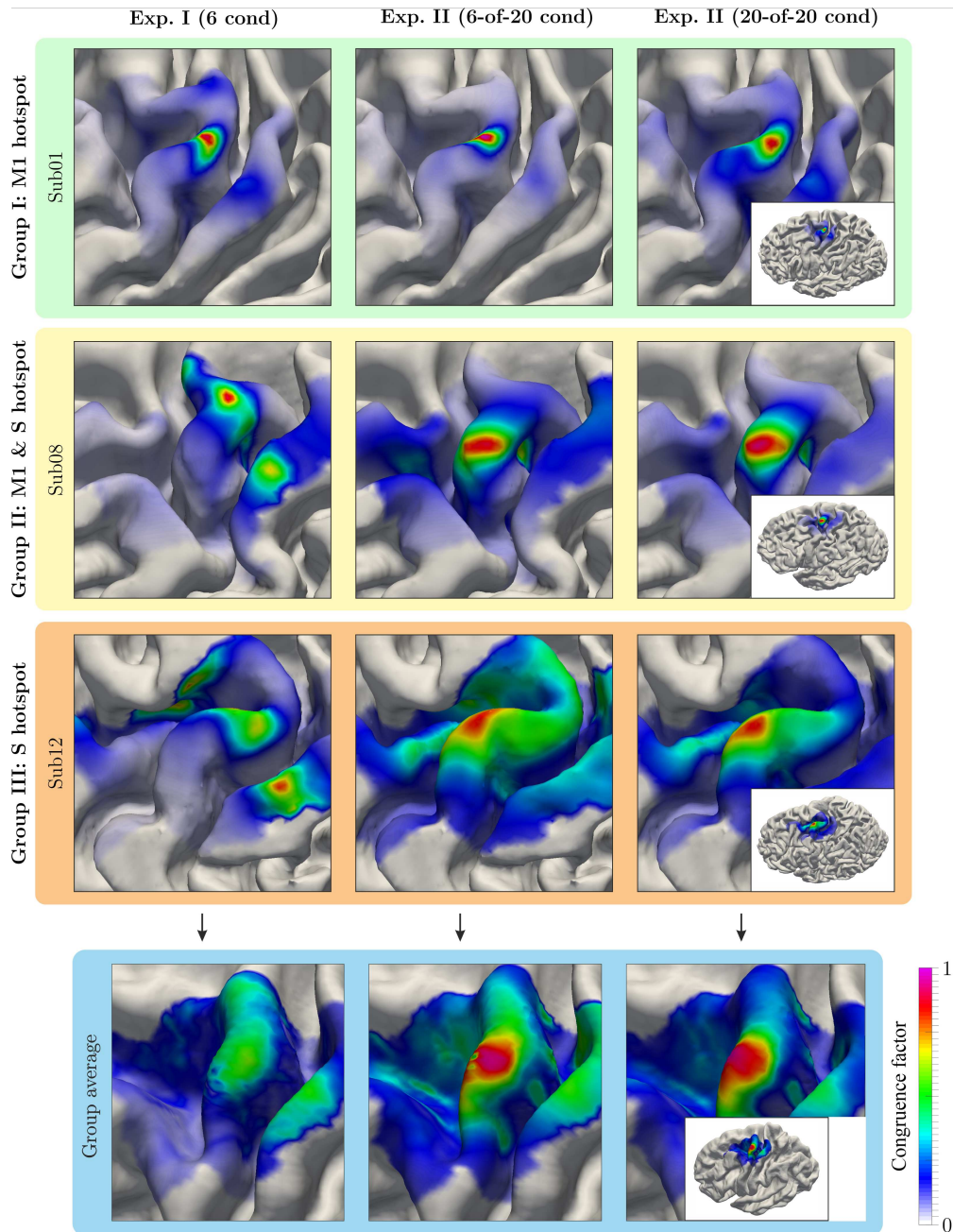
Figure 3.11: Six selected stimulation conditions yield a precise localization.
Six random experimental conditions (Experiment I, left) reach a sound localization only in some subjects (cf. Figure 3.1). 20 experimental conditions (Experiment II, right) always yield a single focal hotspot in M1. Reducing the number of conditions to six with similar location precision is feasible (center). Congruence factors are normalized per map. Subjects were chosen to cover all three result groups (M1 only, green; M1 and somatosensory cortex, yellow; somatosensory cortex only, orange; cf. Figure 3.9). Figure published initially in Weise & Numssen et al. (2020).
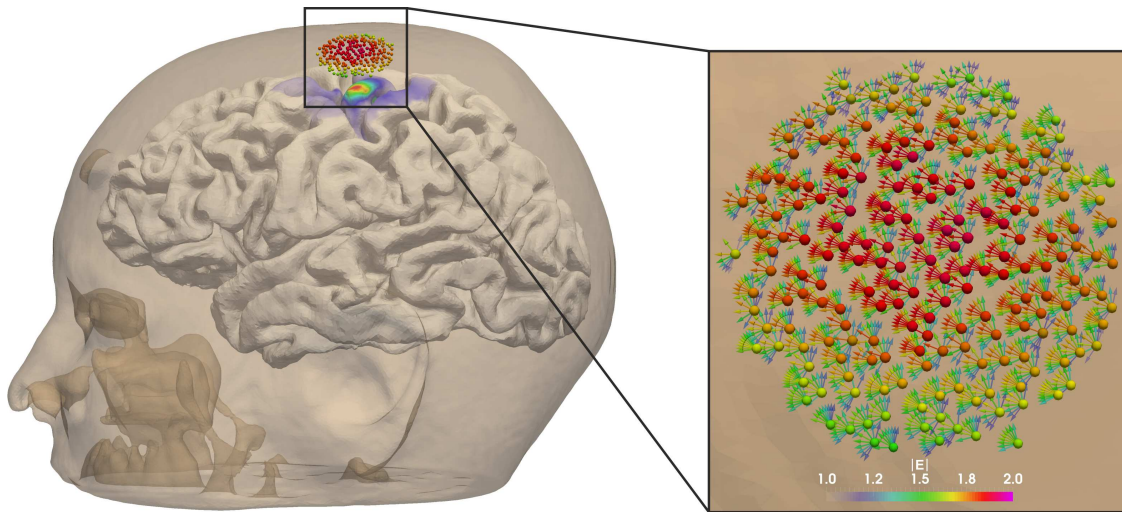
Figure 3.12: Search space to find the optimal coil position/orientation. For every coil position and orientation ($n \approx 4500$), the e-field magnitude $|E|$ was determined in the congruence factor hotspot, i.e., the cortical target of the validation experiment. Color: e-field magnitude $|E|$ in arbitrary unit at the cortical target. Figure published initially in Weise & Numssen et al. (2020).

resulting in a higher distinguishability between the cortical locations in Experiment I. The cross-correlation coefficient only partly reflects this property.

3.6 Validation experiment

3.6.1 Optimization of TMS coil position and orientation

To validate the estimated sites of effective stimulation in Experiment II, I determined the corresponding optimal coil position and orientation. This optimization was implemented by maximizing the e-field magnitude in the previously determined congruence factor hotspot for each of the three subjects.

An exhaustive search optimization procedure was performed to find this optimal coil position/orientation. First, I projected each congruence factor hotspot onto the skin surface. Second, I defined a dense circular grid (radius 20 mm, spacing 1.5 mm) of coil positions and orientations around this projected position (see Figure 3.12). Because the utilized TMS coil generates a symmetric e-field, 180°–pairs of coil orientations (e.g., 45° and 45° + 180° = 225°) generate the same magnitude distribution of the

induced e-field. Therefore, for the optimization, I only considered coil orientations with a positive component into the PA-45 direction so that all subsequently tested coil orientations were drawn from $(-90°, +90°)$ around the PA-45 orientation in 15° steps. The final search grid comprised about 4500 different coil configurations. Within this set of coil positions and orientations, I chose the coil position and orientation that produced the maximum e-field magnitude at the cortical target via a brute force approach. I implemented this optimization routine in SimNIBS v3.1.0 (see Appendix C, Listing C.1).

3.6.2 Data acquisition

If the determined congruence factor hotspot is indeed the origin of the observed effects, the MT must be lowest for the optimized coil position/orientation. Therefore, I experimentally compared the MTs obtained for these optimal coil configurations to those obtained for adjacent coil configurations. For MT determination, single bi-phasic pulses with 5 s ISI were applied.

3.6.3 Results

After determining the optimal coil positions and orientations for the three subjects from Experiment II, the predicted cortical activation site were validated as described previously. One of these subjects, Sub12 from group III (red group in Figure 3.11), was unable to participate in the validation study and was replaced with subject Sub15 from group III, and Experiment II was repeated for her. Using the predefined 20 conditions did not yield a single pronounced congruence factor hotspot for this subject. To increase e-field variance, different conditions at different positions and orientations were added, together with tilted coil positions (see Figure 3.13). I also determined the corresponding best 6-of-30 condition combination yielding similar results compared to the complete 30 condition analysis. The results are shown in Figure 3.14. Notably, all computationally determined optimal coil orientations were similar to the commonly used 45° angle towards the *fissura longitudinalis* (Brasil-Neto et al., 1992; Mills et al., 1992). By using the e-field magnitude, one cannot distinguish between opposite coil orientations. Therefore, the optimization space was restricted to ±90° around the PA-45 direction (see section 3.6).
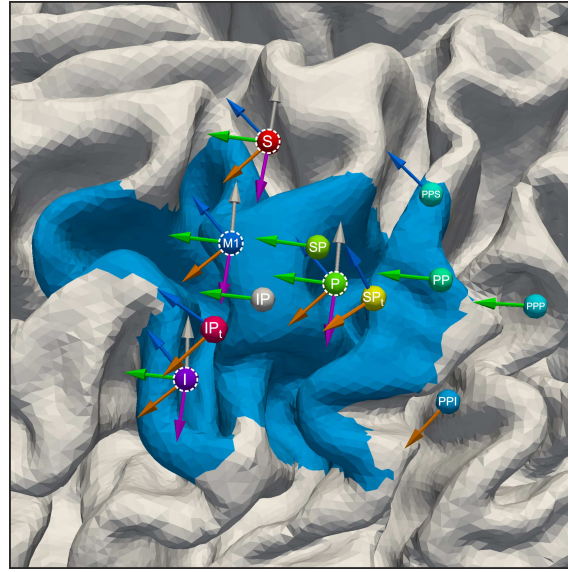
Figure 3.13: Precise localization for subject Sub15 required 10 additional sites.
S: superior (S), P: posterior, I: inferior with respect to M1. The 20 coil positions/orientations
sufficient for the other subjects are highlighted with a dotted white circle. The 10 additional
coil positions and orientations for Sub15 are positioned intermediate (e.g., IP for inferior
posterior) or more posterior to the 20 previous conditions (e.g., PP for posterior posterior).
T: tilted coil (see text). Figure published initially in Weise & Numssen et al. (2020).
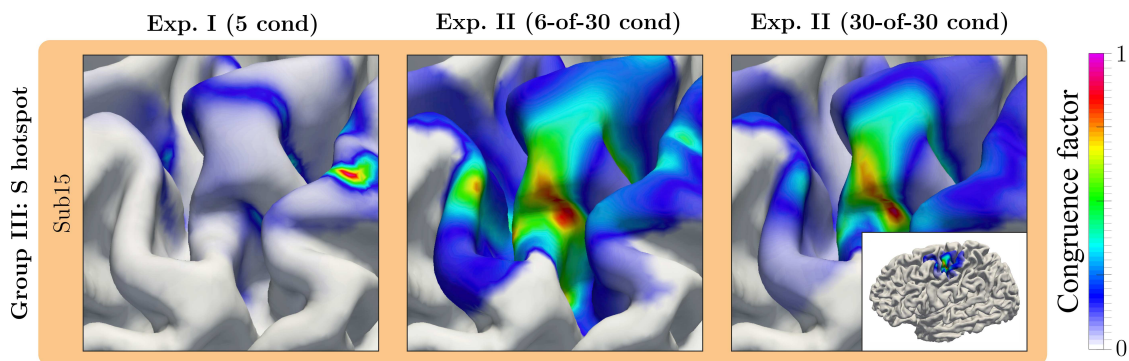
Figure 3.14: Sub15 replaced Sub12 in Experiment II. Both subjects (Sub12 and
their replacement, Sub15) were initially (Experiment I) assigned to group III – hotspot in
the somatosensory cortex. First column: Experiment I congruence factor results from 5
experimental conditions. Middle column: the 6-of-30 combination with the smallest hotspot
area from Experiment II. Right column: congruence factor map from all 30 experimental
conditions of study II. Figure published initially in Weise & Numssen et al. (2020).

In an additional validation experiment the rMTs were assessed for the calculated optimal coil configuration and for several adjacent positions and orientations. Based on the sensitivity of the rMT towards coil position and orientation, we chose spacings of about 7...10 mm in position and 30° for orientation between the tested configurations (see Figure 3.15). As shown in Figure 3.15, the rMTs were always lowest for the predicted optimal coil configuration. This succesful prediction of optimal stimulation conditions to target the FDI representation in M1 confirms the validity of the calculated congruence factor hotspots.

3.7 Critical evaluation and outlook

3.7.1 Summary

I introduced a novel approach to locate the cortical origins of a peripheral physiological response with transcranial magnetic stimulation (TMS) by linking the induced e-field to objective measurements of this physiological response. With this approach, the
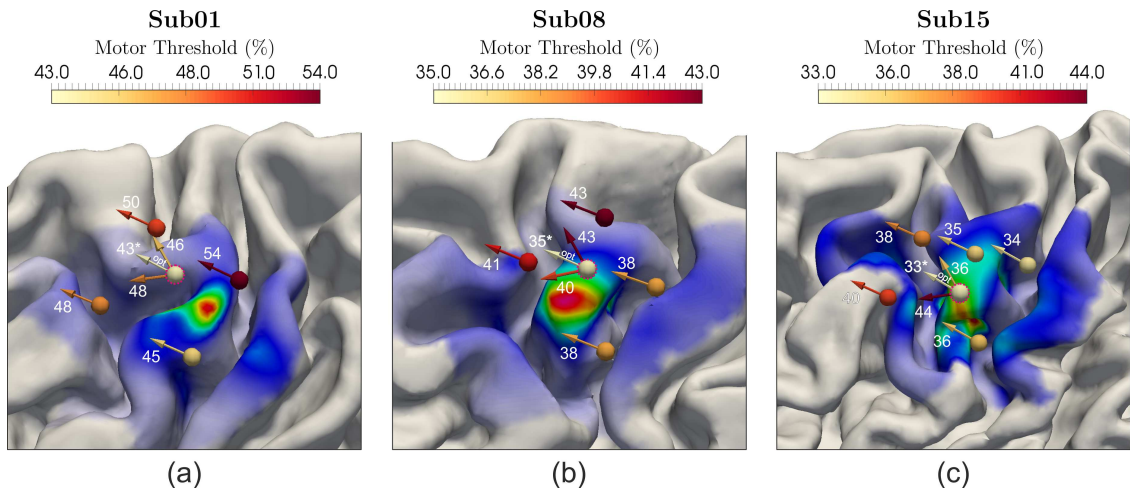
Figure 3.15: The experimental validation confirms cortical localization results. Resting motor thresholds (rMTs) for the pre-computed, optimal coil position (dashed circle, 'opt'; subsection 3.6.1, Figure 3.12 and neighbouring coil positions/orientations were assessed in a final experimental session. Numbers: rMT; the lowest stimulator intensity to elicited 5 of 10 consecutive MEPs with amplitudes >50 μV. Lowest rMTs (indicated with an asterisk) were found at the pre-computed, optimal coil position/orientation. Figure published initially in Weise & Numssen et al. (2020).

cortical muscle representation of the FDI muscle can be identified with single TMS pulses applied over the primary motor cortex. The overall magnitude $|E|$ and the magnitude of the tangential component $E_\parallel$ of the e-field were identified as the relevant quantities for modulating the observed effect.

The experimental validation of the predicted location of cortical muscle representation suggests that a reliable cortical localization can be obtained with relatively few trials or measurements per subject. Based on these results, I derived principles for the coil position selection to improve localization of TMS effects in future applications, both at the single subject- and group-level. In the first experiment, I/O curves for 6 conditions were acquired for fifteen healthy subjects. Three groups were identified with a hotspot at either the primary motor cortex only, the somatosensory cortex only, or both. A subsequent experiment showed that more experimental conditions improved the cortical localization significantly: for all subjects, the muscle representations were identified within M1.

A final validation study in three subjects confirmed that optimizing the TMS coil position and orientation by maximizing the e-field at the predicted cortical target indeed resulted in minimum rMTs. The congruence factor employed in this study quantifies the correlation between the measured physiological variable (here, the MEP) and the induced e-field profiles.

I conclude that this approach significantly improves the localization of effectively stimulated areas during TMS and may increase the power and reliability of the effects in future TMS studies at the individual level.

3.7.2 Limitations

When using short ISI like the 4 s used in Experiment II, potential carry-over effects might affect the IO relationships. In this study, the ISI was kept constant and the intensity of the TMS pulse was systematically increased in a monotonic manner. Therefore, the correlative relationship between e-field and MEP amplitude should remain unaffected, even if the absolute value of the MEP is changed. This assumption is corroborated by strikingly similar results of subject Sub01 with different ISIs (4 and 5 seconds in Experiments I and II, respectively) and confirmed by the successful validation study.

Another potential limitation arises from the inhomogeneous distribution of the MEP variance over the I/O curve, i.e., its heteroscedasticity. The variance is larger in the upper saturation portions than for the lower saturation portion of the curve (Figure 3.7), affecting the least-squares curve-fitting. As suggested elsewhere, a data transformation could mitigate this problem (Nielsen, 1996; Goetz et al., 2014).

The electric vector field is converted into a scalar to compute E–MEP curves. This conversion can be done by computing the magnitude in 3D ($|E|$), by computing the magnitude within the tangential plane ($E_\parallel$), or by projecting onto a particular direction, here, the cortex normal ($E_\perp$). In the latter case, the scalar value can be positive or negative due to the vector direction. Since only positive stimulator intensities were used here, each E–MEP curve based on the normal component covers either only positive or negative e-field values. As the activation function of cells may depend on the e-field orientation, positive and negative curves in one voxel cannot be compared directly and, thus, were analyzed separately (see subsection 3.4.4). A more rigorous solution would be to use positive and negative intensities (by reversing the current direction) to obtain complete E–MEP curves, which can be used to compute the congruence factor by using the shift approach in a straightforward way.

3.7.3 Linking the cortical localization to prior mapping studies

I argued that cortical locations with maximum congruence factors are reasonable candidates for functionally relevant cortical areas. This hypothesis has been confirmed with the validation study, which experimentally tested the identified cortical muscle representations. This cortical localization improved from higher variability between e-fields across all subjects whereas. Moreover, placing the TMS coil directly over M1 with a 45° orientation was – by far – not the most informative condition to add to the localization precision, though yielding the strongest e-field exposure at M1. These observations parallel the emergence of spurious second hotspots in the somatosensory cortex observed by Bungert et al. (2016), when applying TMS pulses selectively over M1, and Laakso et al. (2018), when orienting the TMS coil 45° towards the *fissura longitudinalis* (Brasil-Neto et al., 1992; Mills et al., 1992). Notably, I observed similar effects in Experiment I, when only five or six non-optimal experimental conditions were considered (subject groups II and III, Figure 3.11). Reducing the correlation of the e-fields across the tested positions and orientations

considerably enhanced the localization capabilities of this method in all subjects (Experiment II).

A permutation analysis supported this observation by identifying a considerably increased localization accuracy for higher variability between spatial patterns of the e-fields, using specific combinations of coil positions and orientations. Interestingly, previous studies that selectively incorporated the 45° coil orientation (corresponding to coil orientations $M1_{45°}$, $P_{45°}$, $S_{45°}$ in this study) towards the *fissura longitudinalis* (Laakso et al., 2018; T. D. Krieg et al., 2013; Salinas et al., 2011) appear to support sulcal wall activation by the normal component of the e-field. In contrast, studies testing different coil orientations (Bungert et al., 2016) highlight $|E|$ and gyral crowns (corresponding to coil orientations $M1_{-135°}$, $M1_{-90°}$, $M1_{-45°}$, $M1_{0°}$, $M1_{45°}$ in this study). Recent results from direct electric stimulation (Aonuma et al., 2018) support this identification of the gyral crown to house the cortical muscle representation of FDI, which contrasts with the conclusions from studies using only imaging techniques (Fox et al., 2004; T. D. Krieg et al., 2013). However, both TMS approaches share the major disadvantage of a low resolution that is insufficient to identify the relevant cortical patch. By changing both, i.e., coil position and orientation, congruence factors were low for the normal component of the e-field at the anterior wall of the central sulcus. Since low congruence factors highlight areas where the behavioral effect does not correlate with changes in the local e-field, these results indicate that the previously proposed stimulation mechanism by the normal component (Laakso et al., 2018; Fox et al., 2004; T. D. Krieg et al., 2013) cannot explain the observed effects for all experimental conditions.

In contrast, using the magnitude of the tangential component (and therefore also the overall magnitude) of the e-field yielded reasonable congruence factor maps. This finding suggests that the gyral crowns and upper parts of the sulcal wall are the most likely origin of the motor evoked potentials. Two prior studies have superimposed the calculated e-fields, either in an additive or multiplicative fashion, to locate the cortical position targeted by TMS (Opitz et al., 2013; Aonuma et al., 2018). Opitz et al. (2013) weighted the computed e-fields with the strengths of the observed effects and overlaid the e-fields in an additive fashion. In contrast, Aonuma et al. (2018) superimposed the e-fields in a multiplicative fashion after selecting the experimental conditions for which the observable effect exceeded a particular threshold. The latter

may be disadvantageous since only a small portion of the information contained in the measurement was used. Both methods approximate a covariance between the e-field strength and the MEP amplitude. However, the covariance not only depends on the correlative relationship between the two but also on the general magnitude of the e-field across conditions. This dependence on the local stimulation strength leads to a strong bias towards voxels which generally receive higher e-field strengths, i.e., on gyral crowns, for both approaches.

The validation study confirmed the general optimality of the PA-45 coil orientation towards the *fissure longitudinal* (Brasil-Neto et al., 1992; Mills et al., 1992). The slight deviations between the optima confirm the inter-individual variability in optimal coil orientation observed, for example, by Balslev et al. (2007) and Bungert et al. (2016).

3.7.4 Linking the localization results simulated neural excitation by TMS

Recent studies combined e-field simulations with compartment models of neurons. Seo et al. (2016) have proposed the initial segments of pyramidal cells in layers III and V as the sites of primary excitation by TMS. In contrast, Aberra et al. (2018) identified that the terminals of axon terminals, which are distributed in all directions around the axon, have the lowest thresholds. The collected results, namely high congruence factors of the overall magnitude and the magnitude of the tangential component of the e-field in the gyral crown and rim, support this notion based on experimental data. This is in line with predictions from previous (Silva et al., 2008; Salvador et al., 2011) and recent modeling studies (Aberra et al., 2020), providing a mechanistic explanation for the findings. Future studies may extend the congruence factor approach to more detailed neuronal models (Moezzi et al., 2018; Aberra et al., 2020) and tractography-based fiber tracts (De Geeter et al., 2014; Geeter et al., 2016).

3.7.5 Towards a clinically suitable TMS mapping procedure

To enable clinical applicability of the proposed method, for instance, in pre-surgical mapping, the experimental effort has to be reduced to a minimum while ensuring high reliability. The permutation analysis from Experiment II (Figure 3.10 – Figure B.3) revealed that six TMS conditions, at three locations around M1, with different

orientations, are sufficient to address the localization problem at hand. Notably, the actual condition combinations resulting in a minimum hotspot area differ strongly between subjects, most likely due to inter-individual differences in anatomy and functional brain organization. Whereas a high number of experimental conditions increases the stability and reliability of the solution, the resolution accuracy can also be impeded by introducing more measurement noise.

This influence of noise became evident in the permutation study, in Figure 3.10, where the minimal hotspot area had a minimum for $k = 6$ conditions and slightly increased for higher values of k. Increasing the e-field variability is a promising starting point for subject-specific optimization to determine the minimum number and selection of coil positions/orientations before the experiment.

3.7.6 Outlook

In summary, the presented mapping approach presents a novel and unique localization method for cortical muscle representations via the functional relationship between induced e-field and response. With the results presented above, I could establish an experimental paradigm and an analysis approach to render such an approach feasible. Finally, the extensive experimental validations confirm the correctness and the reproducibility of the cortical localization results. Although this method's number of necessary stimulations is comparatively low, its realization relies on specific coil positions and orientations throughout the experiment.

As a next step, I adapted the mapping approach to increase the experimental practicability and further reduce the number of necessary stimulations via higher efficiency. This advanced method is presented in the next chapter.
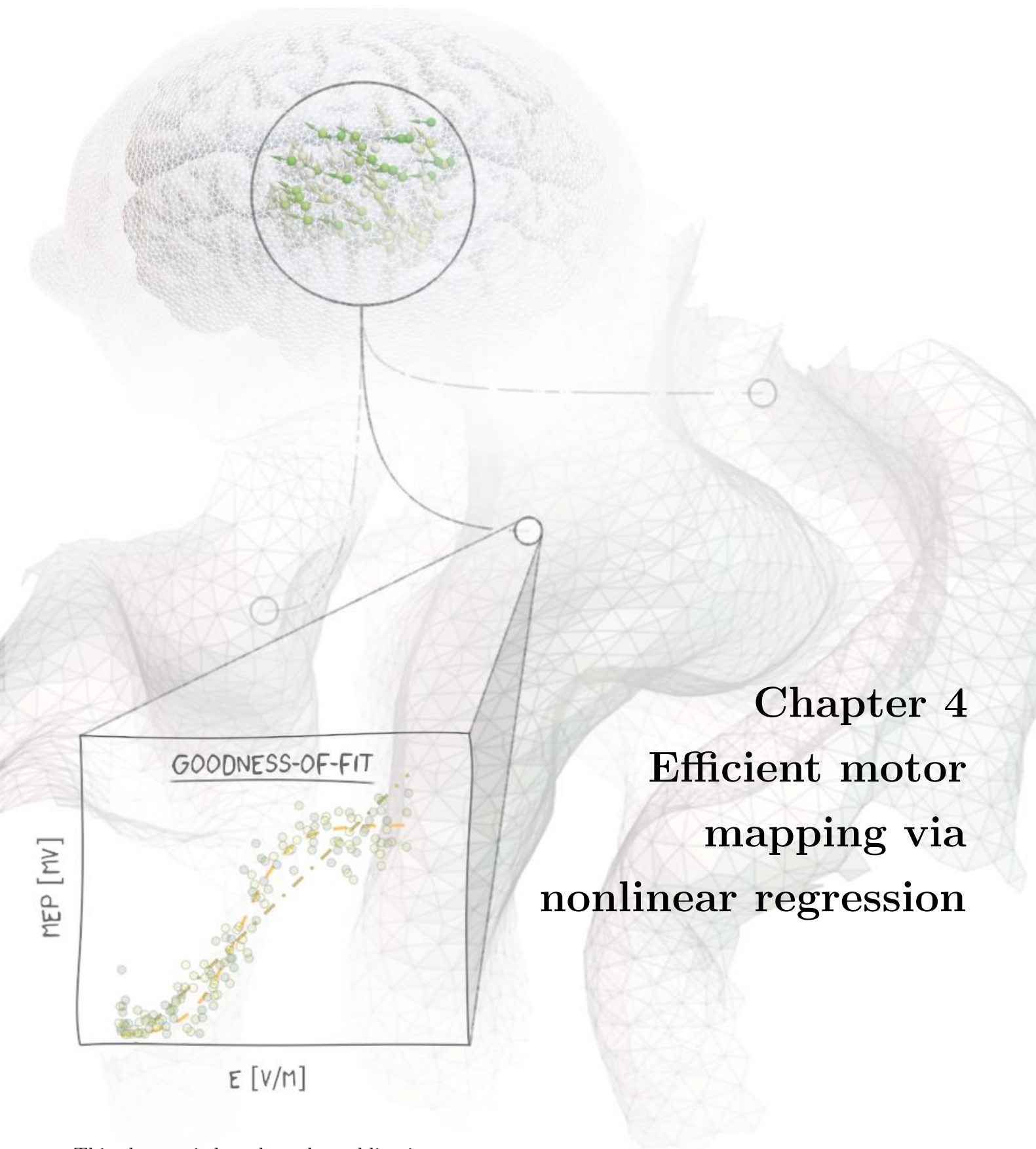
Chapter 4
Efficient motor mapping via nonlinear regression

GOODNESS-OF-FIT

MEP [MV]

E [V/M]

4.1 Overview

Above, I introduced an approach to exploit information from multiple TMS-induced e-fields to locate cortical muscle representation. This approach linked the electrical field (e-field) from a set of coil positions and orientations to a TMS effect, the motor evoked potential (MEP) amplitude, by cortical input-output curves. Six well-selected coil positions and orientations, resulting in about 600 TMS pulses, solved the localization problem.

Here, I substantially advanced this approach to allow arbitrary ('*quasi-random*') coil positions and orientations for each TMS pulse, thus providing a simple experimental realization. This integration of information from quasi-random stimulation sites decreased the required stimulations for reliable cortical localization. In 14 healthy subjects, this advanced localization paradigm was applied to identify the somatotopic organization of three hand muscles concurrently within one TMS experiment. The identified cortical muscle representations were validated in a second experimental session to show a successful distinction of different finger muscle representations at the subject-level. Based on an extensive convergence analysis, I provide metrics to evaluate the overall goodness of the cortical mapping procedure.

4.2 Cortical localization with the regression approach

The concept of the regression-based localization method is illustrated in Figure 4.1. Again, the cortical site of effective stimulation is identified by fitting cortical I/O curves, relating the local e-field to the MEP amplitude. Here, one I/O curve is fitted in each cortical element for all stimulations instead of assessing the congruence of multiple I/O curves from different coil positions/orientations (cf. chapter 3). These single I/O curves are then compared against each other by their goodness-of-fit. The goodness-of-fit would be highest at the cortical site housing the relevant neurons.

The cortical elements must be exposed to different stimulation profiles to allow a functional separation. Before (chapter 3), this was achieved via multiple fixed coil positions/orientations. Here, this variance is assured by stimulating at quasi-random coil positions/orientations.
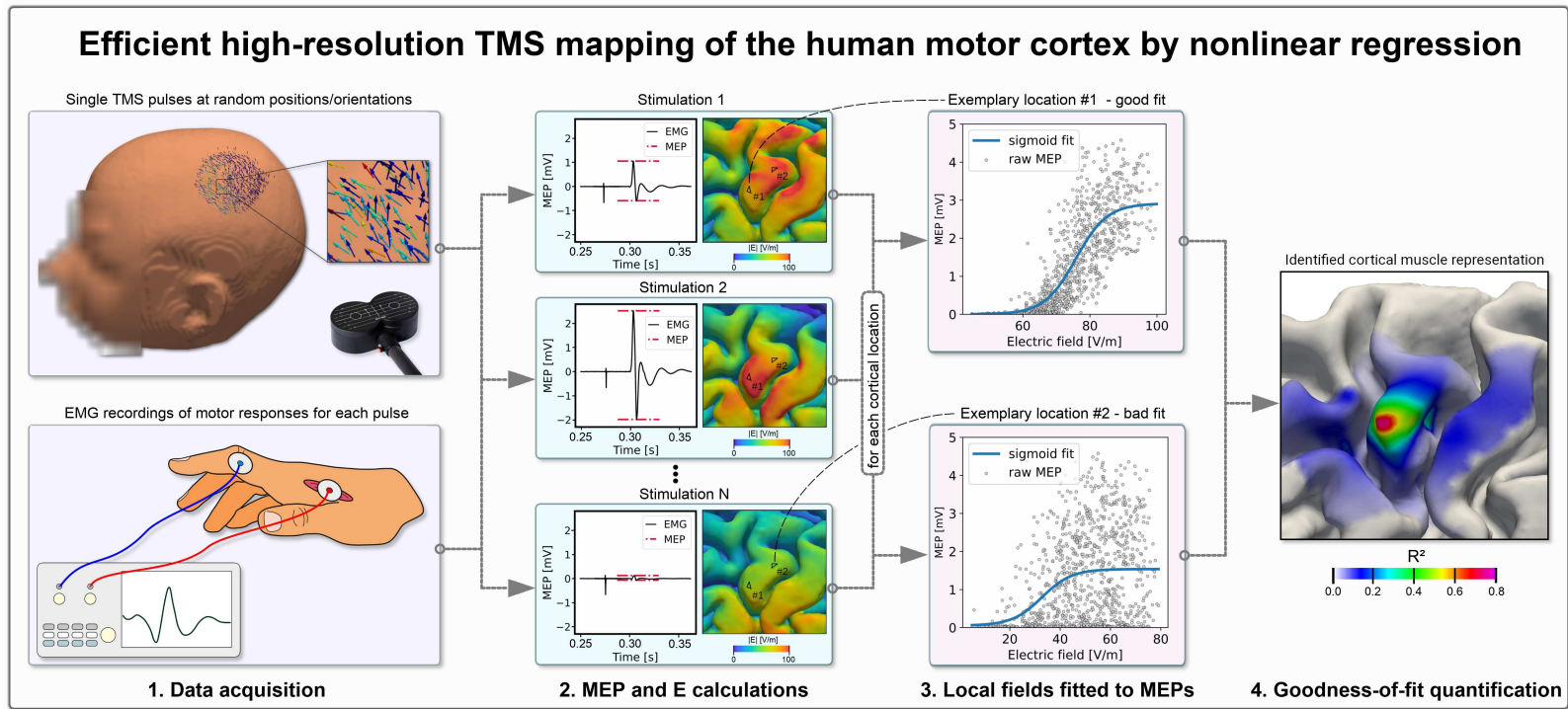
Figure 4.1: How to locate cortical muscle representations via local e-field-behaviour relationships.

1. Single pulse TMS is applied to the primary motor cortex region with random coil positions and orientations. The stimulator intensity is set to about 150 % of the individual resting motor threshold. All coil positions/orientations and the EMG data from one (or multiple) finger muscles are recorded.
2. MEP amplitudes from the EMG data and e-fields are computed for each stimulation.
3. For each cortical location (*element*), its e-field exposure, e.g., the e-field's magnitude $|E|$, is regressed on the MEPs. This is done for each muscle separately. A complete sampling of the I/O curve has to be assured to yield robust fits.
4. The goodness-of-fit map identifies the cortical muscle representation based on the R^2 score.

Figure published initially in Numssen, Zier, et al. (2021).

In addition, the I/O curve fitting can be performed with different functions, reflecting different biophysiological activation hypotheses. Below, I compare standard linear regression, nonlinear regression using a sigmoidal function, and nonlinear regression using a log-transformed sigmoidal function.

LINEAR REGRESSION. Here, a linear relationship between e-field intensity x_{ij} of stimulation i at the cortical element j and the MEP amplitude y_i is fitted:

$$\tilde{y}_{i,j} = \beta_{0,j} + \beta_{1,j}x_{i,j} \qquad\qquad i = 1, \ldots, N_{TMS}; j = 1, \ldots, N_{elms} \quad (4.1)$$

where:

i = stimulation number,
j = cortical element,
β_0 = y offset,
β_1 = slope,
x = cortical e-field strength $[\mathrm{V\,m}^{-1}]$,
N_{TMS} = total number of stimulations,
N_{elms} = number of cortical elements.

β_0 and β_1 are estimated in every ROI element j. This approach is the cheapest in computational cost but neglects the characteristic sigmoidal shape of the input-output curve observed in the motor cortex.

SIGMOIDAL REGRESSION. A sigmoidal input-output function provides more physiological plausibility:

$$\tilde{y}_{i,j} = y_0 + \frac{a_j - y_0}{1 + e^{-r_j(x_{i,j}-x_{0,j})}} \qquad\qquad i = 1, \ldots, N_{TMS}; j = 1, \ldots, N_{elms} \quad (4.2)$$

where:

$\tilde{y}$ = regressand for MEP amplitude [mV],
x_0 = turning point on the abscissa,
y_0 = y offset,
a = saturation amplitude,
r = slope.

I estimated y_0 from baseline EMG data without any stimulus (Alavi et al., 2019) to

reduce the number of free parameters to speed up the calculation.

LOG-TRANSFORMED SIGMOIDAL REGRESSION. EMG data from this domain is typically heteroscedastic, and log-transformation may be applied to equalize variance across the range of MEP magnitudes (Goetz et al., 2019, 2014; Peterchev et al., 2013; Nielsen, 1996). Here, a sigmoidal transformation was used to account for this:

$$log_{10}\left(\tilde{y}_{i,j}\right) = y_0 + \frac{a_j - y_0}{1 + e^{-r_j(x_{i,j} - x_{0,j})}} \qquad i = 1, \ldots, N_{TMS}; j = 1, \ldots, N_{elms} \quad (4.3)$$

The non-linear functions were fitted in every ROI element using the Levenberg-Marquardt algorithm. I assessed the element-wise goodness-of-fit by means of the coefficient of determination R^2:

$$R_j^2 = 1 - \frac{VAR(y - \tilde{y}_j)}{VAR(y)}, j = 1, \ldots, N_{elms} \qquad \text{Coefficient of determination} \quad (4.4)$$

where:

y = measured MEP amplitude,

$\tilde{y}$ = estimated MEP amplitude.

The better the fit, the closer R^2 is to unity.

The sign of the normal component depends on the e-field's direction. To prevent the confounding of differing neuronal activation mechanisms, positive and negative parts of the e-fields were analyzed separately. Specifically, an initial linear fit was performed in each element for both datasets, i.e., for positive and negative e-field components separately, to determine the slopes and associated p-values. Only datasets with a p-value < 0.001 and a positive slope for positive e-field components or a negative slope for negative e-field components were considered for further analyses. The dataset yielding the higher R^2 score was chosen for the final non-linear fit.

This method is principally equivalent to the curve shift approach proposed previously (chapter 3). However, in this approach, the curve-fitting is done element-wise in the E–MEP space leveraging information from every TMS pulse, in contrast to the condition-wise approach implemented before. The procedure yields one cortical map of R^2 scores per muscle, quantifying the probability of generating MEPs for each cortical element.

4.3 Materials and methods

4.3.1 Subjects

Fourteen healthy, right-handed participants (seven females, age 21–38 years) with an average laterality quotient of 95.28 ±7.93 according to the Edinburgh Handedness Inventory (Oldfield, 1971) were recruited. Subject inclusion was in accordance with the safety guidelines for TMS studies (Rossi et al., 2021). Written informed consent was obtained from all participants prior to the examination. The study was performed according to the guidelines of the Declaration of Helsinki and approved by the local Ethics committee of the Medical Faculty of the University of Leipzig.

4.3.2 Hardware setup

TMS pulses were applied with a MagPro X100 stimulator (MagVenture GmbH, Willich, Germany, firmware version 7.1.1) and an MCF-B65 figure-of-eight coil. Coil positioning was guided by a neuronavigation system (TMS Navigator, Localite, Germany, Sankt Augustin; camera: Polaris Spectra, NDI, Canada, Waterloo), and the coil position and orientation were saved for each stimulation.
Electromyography (EMG) data from three finger muscles were recorded from the subjects' right hand for each stimulation: from the *musculus abductor pollicis brevis* (APB; thumb muscle), first *dorsal interosseous* muscle (FDI; index finger muscle), and *musculus abductor digiti minimi* (ADM; little finger muscle), using a standard belly-tendon montage (Kleim et al., 2007). Electrodes were connected to a patient amplifier system (D-360, DigitimerLtd., UK, Welwyn Garden City; bandpass filtered from 10 Hz to 2 kHz), connected to an acquisition interface (Power1401 MK-II, CED Ltd., UK, Cambridge, 4 kHz sampling rate). EMG recording was performed with Signal (CED Ltd., version 4.11). Subsequently, the EMG data was low-pass filtered with a 6th-order Butterworth filter (cutoff frequency: 500 Hz). MEPs were calculated as peak-to-peak amplitudes from 18 ms to 35 ms after the TMS pulse.

4.3.3 Numerical simulations of the induced e-field

E-field calculations were conducted for each pulse (SimNIBS v3.1, Saturnino, Madsen, & Thielscher, 2019; Thielscher et al., 2015) with high-resolution anisotropic FEM.

MRI scans were acquired on a 3 T MRI scanner (Siemens Verio or Skyra) with a 32-channel head coil using the same acquisition parameters as before (subsection 3.4.3). T1 and T2 images were used for tissue-type segmentation. Conductivity tensors in gray and white matter were reconstructed from diffusion-weighted images using the volume-normalized mapping approach (dwi2cond, simnibs.github.io; Güllmar et al., 2010). Individual head models were generated using the headreco pipeline (Nielsen et al., 2018) utilizing SPM12 (www.fil.ion.ucl.ac.uk/spm/software/spm12; Penny et al., 2011) and CAT12 (www.neuro.uni-jena.de/cat; Gaser et al., 2022). The final head models were composed of $\sim 3.4 * 10^6$ nodes and $\sim 18.5 * 10^6$ tetrahedra (average volume: $0.15 \, \text{mm}^3$ in the cortex). Six tissue types were included with the same conductivity estimates as before (subsection 2.3.5). See above and Saturnino, Madsen, and Thielscher (2019) for FEM details.

A region of interest (ROI) was defined around the hand knob area (FreeSurfer, surfer.nmr.mgh.harvard.edu; Fischl et al., 1999; Dale et al., 1999) based on the FsAverage template. This covered parts of the somatosensory cortex (BA1, BA3), the primary motor cortex (M1, BA4), and the dorsal premotor cortex (PMd, BA6). The HCP-MMP parcellation was used (Glasser et al., 2016) to visualize the border between PMd and M1. All analyses were performed on the gray matter midlayer (halfway between gray and white matter surfaces).

4.4 Localization experiment

4.4.1 Data acquisition

Localization of the initial MEP target location was initially guided by group coordinates from Maykaa et al. (2006). The rMT for the FDI and the corresponding coil position (Yousry et al., 1997) was manually assessed to provide an initial estimation of the individual stimulator intensity needed to elicit MEPs. The rMT was defined as the minimum stimulator intensity yielding MEPs with an amplitude of at least $50 \, \mu\text{V}$ in at least 5 out of 10 consecutive TMS pulses (Rothwell et al., 1999). 900–1100 single bi-phasic pulses were applied per subject with a 5 s inter-stimulus interval (ISI). Coil positions and angles were quasi-randomly selected for each stimulation to sample from different e-field distributions and corresponding MEPs.

The coil center positions were restricted to a circular area of a $2\,\text{cm}$ radius around the estimated M1 location (Figure 4.1, left) and the coil rotation to approximately $\pm 60°$ relative to the computed optimal coil angle. The stimulation area definition proved sufficient to elicit large MEPs from the upper limit of the I/O curve at the estimated M1 stimulation site and small or no MEPs at the periphery for a fixed stimulator intensity.

About $150\,\%$ of the estimated rMT intensity was individually assessed to stay in a comfortable range. Experimenters were instructed to evenly sample the determined area such that all parts of the stimulated area were visited several times throughout the experimental session to guard against possible sequential effects. A second experimenter monitored the EMG signal from all three muscles to identify any muscle pre-activation, in which case the stimulation was paused.

4.4.2 Results

The induced e-fields varied considerably across coil positions and orientations on the pre-defined cortical ROI. Differential, i.e., uncorrelated stimulation patterns are neccessary to allow a separation of cortical elements based on the induced e-fields. However, due to the high auto-correlation of the e-field this condition can only be achieved to a certain degree. See Figure 4.2 for the correlation patters and cortical field exposures of an exemplary subject. For each subject, the cortical mapping was performed with linear, sigmoidal, and log-transformed sigmoidal functions to identify the cortical representations of APB, FDI, and ADM. Detailed results are presented in Figure 4.3 for one subject for the e-field magnitude $|E|$ and in Figure 4.4 and Figure 4.5 for the tangential component $E_{\parallel}$ and normal component $E_{\perp}$. The distributions of the normalized R^2 maps are highly similar across different fit functions. The computation time for sigmoidal mapping was significantly shorter than for mappings with log-transformed sigmoids. Thus, sigmoidal functions are used throughout the rest of the analyses as this function type provides a well-balanced compromise in terms of mapping accuracy and computation efficacy. Table 4.1 provides peak values for all methods and subjects.

Mapping results for all 14 subjects considering the e-field magnitude are shown in Figure 4.6. See Figure 4.7 and Figure 4.8 for the tangential and normal components,
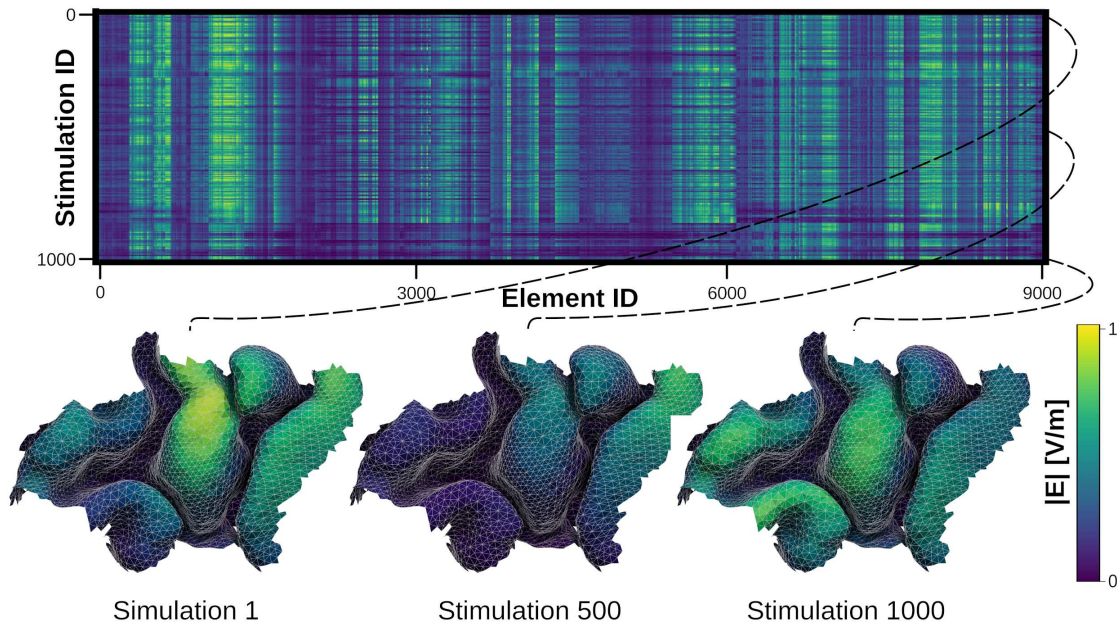
Figure 4.2: The quasi-random sampling yields de-correlated e-field data.
Top: Neighboring elements (columns) in the cortical region of interest (ROI) received similar e-field exposure for a single TMS pulse (rows) due to the e-field's auto-correlation. Stimulating with quasi-random coil positions and orientations introduced variance in the stimulation profiles between cortical elements across all stimulations (column vectors). Bottom: Cortical e-field exposure on the ROI used in the subsequent analyses for three exemplary stimulations (#1, #500, and #1000). Data is shown for an exemplary subject.

respectively. The R^2 hotspots are primarily located on the gyral crown and rim of the precentral gyrus. Representations of FDI and APB were found to be closer to each other than to ADM, which was generally situated superior to them. For one subject, the muscle representation was located in M1, whereas for 12 subjects, they were located in caudal PMd. See Table 4.2 for group average results. The localization based on the different e-field components identified similar cortical regions. The e-field's magnitude yielded significantly higher goodness-of-fit values than the tangential component ($Z = 249$, $p = 0.0113$) and significantly higher goodness-of-fit values than the normal component ($Z = 289$, $p = 0.0422$). For both comparisons, a Wilcoxon signed-rank test was performed due to the non-normality of the data.

Hysteresis effects (Möller et al., 2009) have been shown for repeated TMS pulses at the same stimulation site, potentially affecting the proposed method by introducing unexplained variance. Here, a post-hoc split-half test did not identify significant
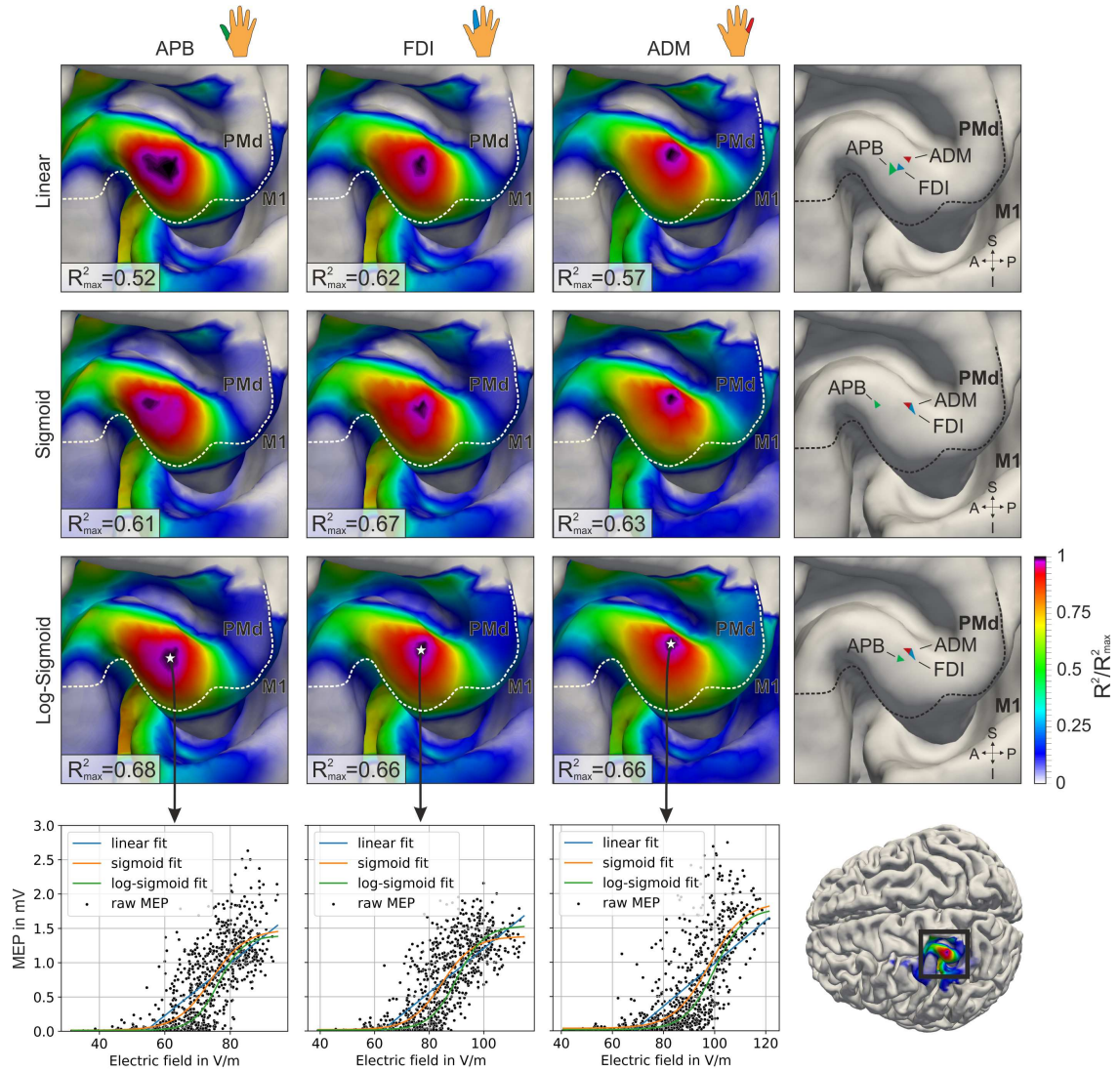
Figure 4.3: Log-sigmoidal fitting yields the optimal yield-cost trade-off.
Left columns: Normalized coefficients of determination (R^2) for APB, FDI, and ADM
muscle, respectively, from the magnitude of the e-field ($|E|$). Raw R^2_{max} values are between
0.3 (linear regression) and 0.7 (non-linear regression). Last column: The hotspots for the
three digit muscles. Rows: Mapping results for linear, sigmoidal, and log-transformed
sigmoidal functions yield similar shapes. The boundary between the dorsal premotor cortex
(PMd/BA6) and the primary motor cortex (M1/BA4) is determined with the HCP-MMP
atlas (dashed white line; Glasser et al., 2016). Bottom: Function fits for optimal elements
are characterized by a clear relationship between the induced e-field and the evoked motor
potentials. R^2 scores are normalized to the muscle-wise maximum value R^2_{max}. Single
subject results for subject S12. Figure published initially in Numssen, Zier, et al. (2021).

Table 4.1: Maximum R^2 values for three fit function types.

	APB			**FDI**			**ADM**		
Subject	lin	sig	log sig	lin	sig	log sig	lin	sig	log sig
S01	0.50	0.70	0.65	0.58	0.71	0.72	0.46	0.75	0.73
S02	0.31	0.38	0.57	0.44	0.56	0.65	0.35	0.49	0.61
S03	0.33	0.35	0.57	0.66	0.7	0.83	0.51	0.55	0.75
S04	0.32	0.34	0.52	0.39	0.52	0.65	0.35	0.47	0.63
S05	0.32	0.55	0.53	0.37	0.63	0.62	0.29	0.49	0.59
S06	0.55	0.69	0.76	0.64	0.76	0.78	0.46	0.58	0.75
S07	0.42	0.57	0.74	0.51	0.63	0.76	0.5	0.69	0.80
S08	0.41	0.58	0.76	0.51	0.70	0.67	0.24	0.44	0.71
S09	0.31	0.35	0.60	0.42	0.47	0.65	0.27	0.30	0.64
S10	0.41	0.58	0.59	0.42	0.59	0.58	0.37	0.59	0.60
S11	0.31	0.36	0.56	0.38	0.42	0.55	0.27	0.29	0.43
S12	0.52	0.61	0.68	0.62	0.67	0.66	0.58	0.64	0.66
S13	0.15	0.20	0.56	0.15	0.24	0.59	0.19	0.33	0.74
S14	0.56	0.66	0.71	0.62	0.72	0.79	0.63	0.72	0.78

Notes: For each mapping solution per subject, muscle, and fit function the maximum R^2 values are shown. For linear and sigmoidal functions the scores are calculated in the linear domain, and for the log-sigmoidal functions, in the log domain. lin: linear fit function. sig: sigmoidal fit function with y_0 parameter estimated from EMG noise floor. log sig: logarithmic sigmoidal fit function.

differences in the localization across experimental time, supporting the validity of the realized randomization procedure.

Table 4.2: Group-average localization results for three finger muscles.

Muscle	MNI x	MNI y	MNI z	Relative MEP	Absolute MEP
APB	-34.7 ± 2.51	-13.9 ± 3.12	66.5 ± 2.88	86 %	4.88 mV ± 0.59 mV
FDI	-34.1 ± 2.59	-14.3 ± 3.40	66.8 ± 3.00	100 %	5.68 mV ± 0.66 mV
ADM	-32.7 ± 3.77	-16.0 ± 3.30	68.0 ± 3.11	72 %	4.10 mV ± 0.59 mV

Notes: MNI coordinates in *mean* mm ± *SD*. Right columns: relative and absolute *mean* (± *SD*) of the maximum MEP across subjects 2–14. APB: thumb muscle, *musculus abductor pollicis brevis*. FDI: index finger muscle, first *dorsal interosseous*. ADM: little finger muscle, *musculus abductor digiti minimi*. MEP: motor evoked potential.
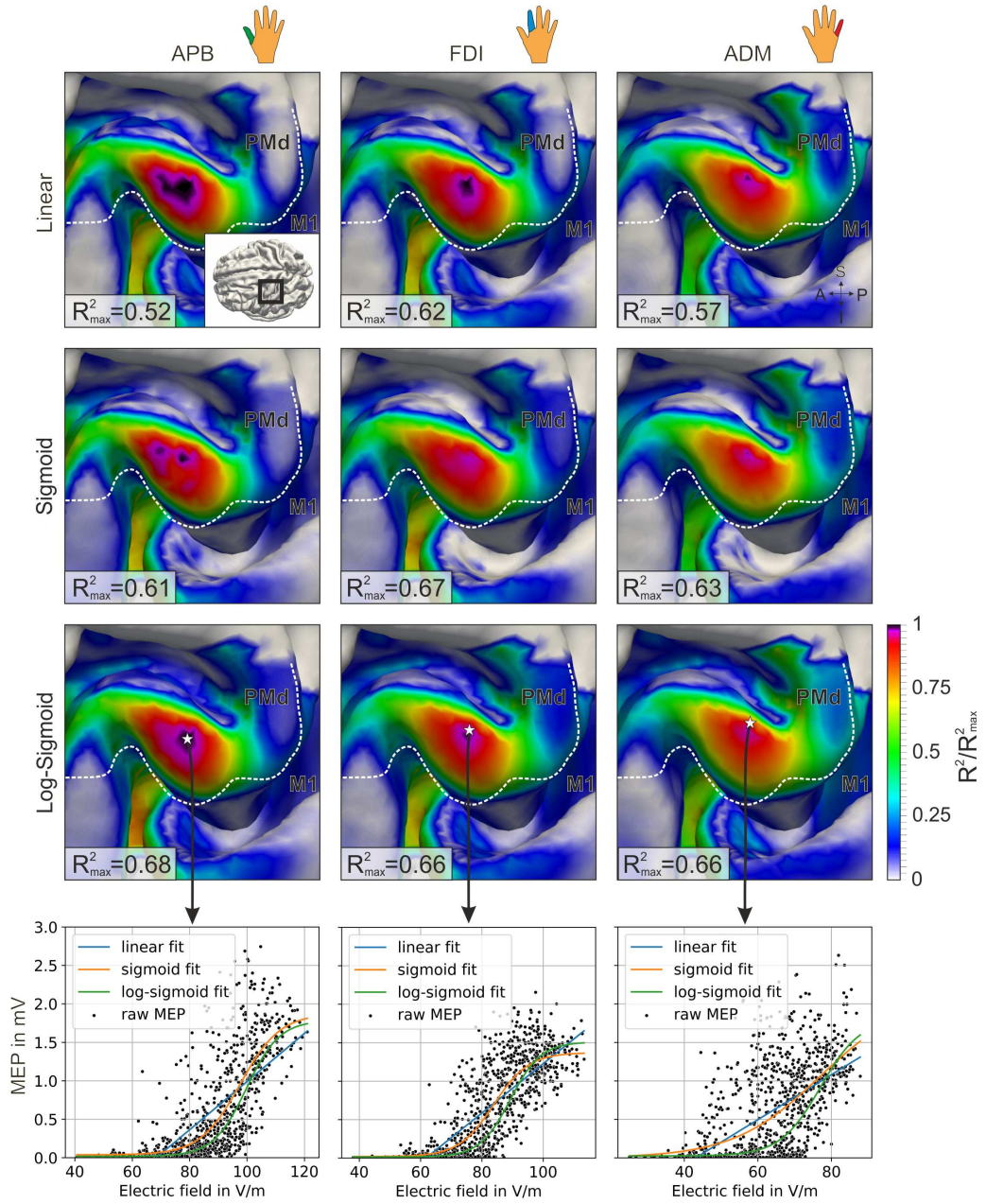
Figure 4.4: The tangential component $E_\parallel$ yields similar results as $|E|$.
Left columns: Mapping results for APB, FDI, and ADM, respectively, from the tangential component of the e-field ($E_\parallel$). The three fit functions (linear, sigmoidal, and log-transformed sigmoidal) yield similar shapes (rows). Overall, the results are qualitatively similar to results from the e-field's magnitude $|E|$. R^2 scores are normalized to the R_{max}^2 values given by the localization analyses using the e-field magnitude $|E|$. Single subject results for subject S12. See Figure 4.3 for details. Figure published initially in Numssen, Zier, et al. (2021).

Figure 4.5: The normal component $E_\perp$ does not yield precise localization. Left columns: Mapping results for APB, FDI, and ADM, respectively, from the normal component of the e-field ($E_\perp$). Across all function types (rows), the R^2 values are considerably lower than for $|E|$ and $E_\parallel$ results (c.f. Figure 4.3 and Figure 4.4). R^2 scores are normalized to the $R^2_{\max}$ values given by the localization analyses using the e-field magnitude $|E|$. Single subject results for subject S12. See Figure 4.3 for details. Figure published initially in Numssen, Zier, et al. (2021).
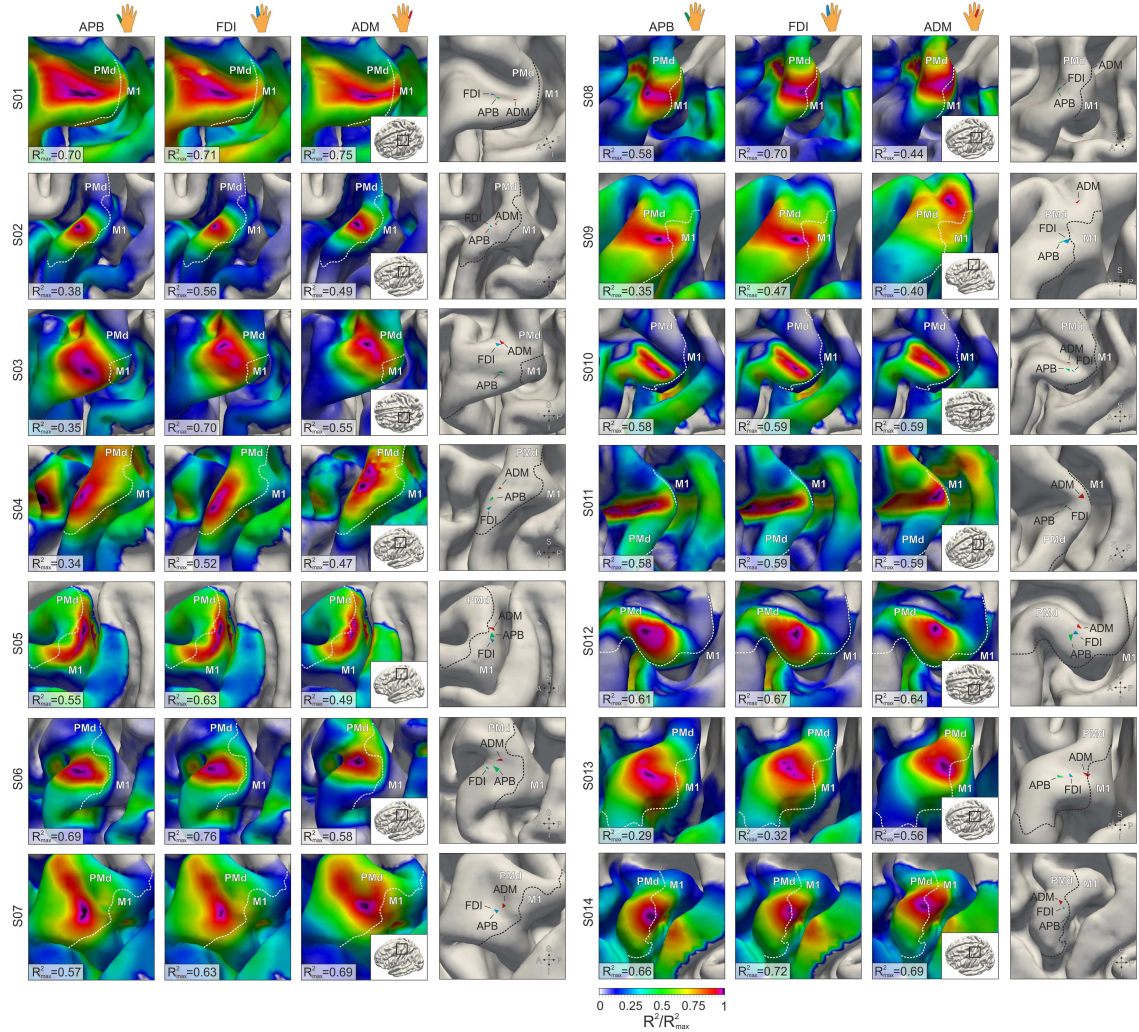
Figure 4.6: The e-field's magnitude identifies a cortical hotspot in PMd or M1. Localization results from all 14 subjects using nonlinear regression fitted with sigmoidal functions. First three columns: normalized coefficients of determination (R^2) for APB, FDI, and ADM, respectively, considering the magnitude of the e-field ($|E|$). Raw R^2_{max} values are between 0.4 and 0.8. Last column: the identified hotspots for the three digit muscles. Subject S01 was measured with random stimulation intensities instead of the fixed intensity used subsequently. The boundary between the dorsal premotor cortex (PMd/BA6) and the primary motor cortex (M1/BA4) was determined with the HCP-MMP atlas (dashed white line; Glasser et al., 2016). R^2 scores are normalized to the subject- and muscle-wise maximum R^2_{max}. Figure published initially in Numssen, Zier, et al. (2021).

4.5 Convergence analysis

4.5.1 Rationale

About 1000 pulses from quasi-random TMS coil positions and orientations were recorded per subject in the data acquisition presented above to assure a sufficient sampling of the I/O curve and to provide enough variance across cortical elements for a valid functional localization. Based on the correlation matrices of the induced fields (c.f. Figure 4.2) and the high auto-correlation of TMS-induced e-fields, this large number of stimulations most probable oversampled the achievable variance. However, this large dataset can be used as a *ground-truth* proxy when testing subsamples of the whole dataset to identify the minimum number of stimulation conditions that yield valid localization results. In addition, metrics can be derived from this permutation ananyses to estimate the overall goodness of a given localization experiment.

4.5.2 Metrics

I analyzed the convergence of subsets, from $n = 10$ to all available (900–1100) stimulations to identify the minimum number of pulses needed to localize cortical muscle representations. To approximate the robustness this convergence analysis was performed for 100 independent initializations for each subject. I assessed two metrics: i) the normalized root-mean-square deviation (NRMSD) as a measure of the overall similarity of the resulting cortical map and ii) the geodesic distance to quantify the accuracy of the hotspot identification. Convergence for both was quantified against the full set of stimulations (N) and against the previous solution from $(n-1)$ stimulations. The former yields a proxy for the (unknown) ground truth, whereas the latter quantifies the magnitude of change from one stimulation to the following. This stability measure can be used as a stop criterion during an online analysis and for post-hoc evaluations of a conducted mapping procedure.

The NRMSD between the R^2 map for n stimulations and the reference map R^2_{ref} was calculated as
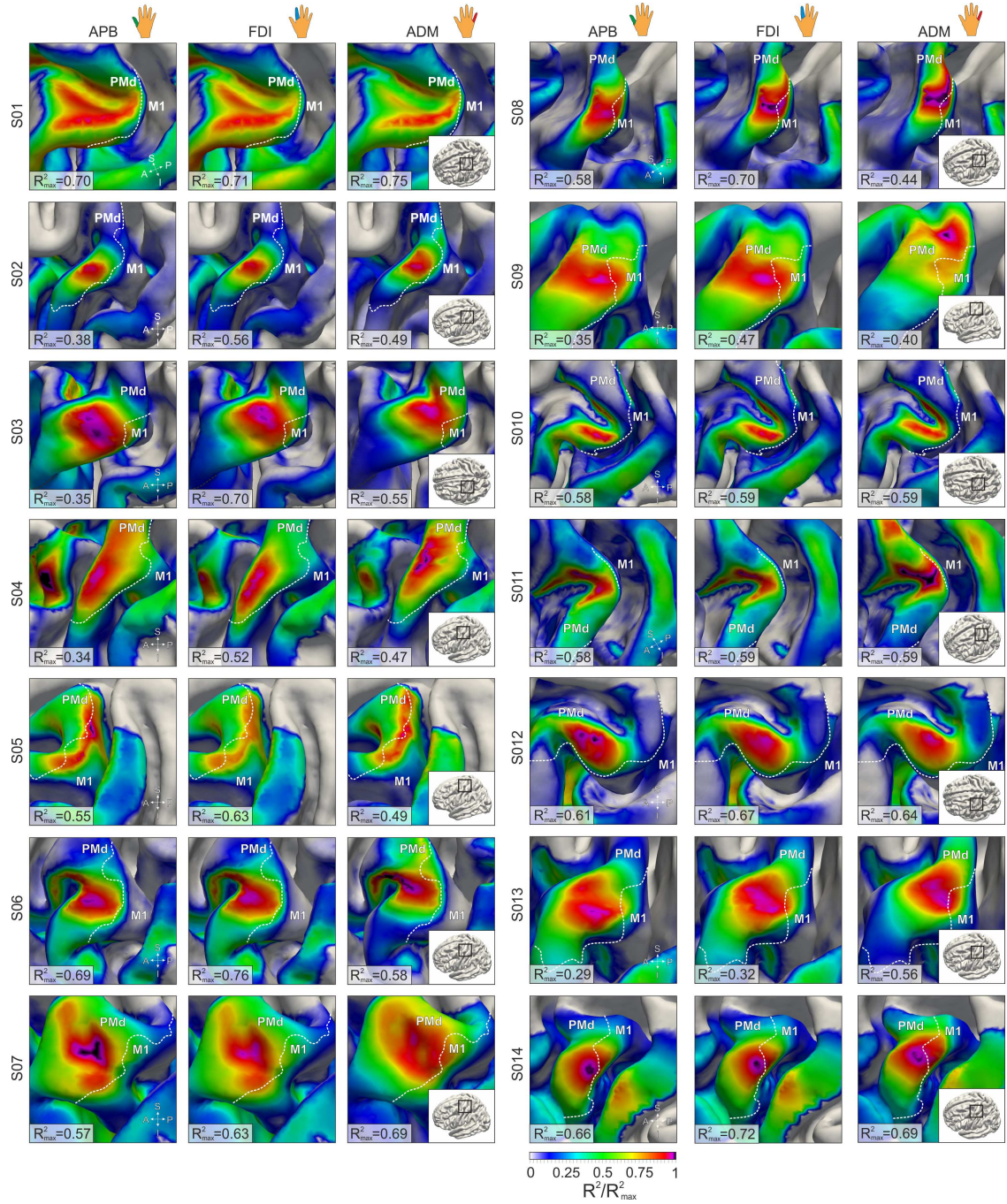
Figure 4.7: The tangential e-field component $E_\parallel$ yields similar hotspots as $|E|$.
In comparison to the localization results from $|E|$ (Figure 4.6), the tangential component
yields lower goodness-of-fit values across most subjects. R^2 scores are normalized to the
subject- and muscle-wise maximum $R^2_{\max}$ for the e-field magnitude (Figure 4.6). Figure
published initially in Numssen, Zier, et al. (2021).
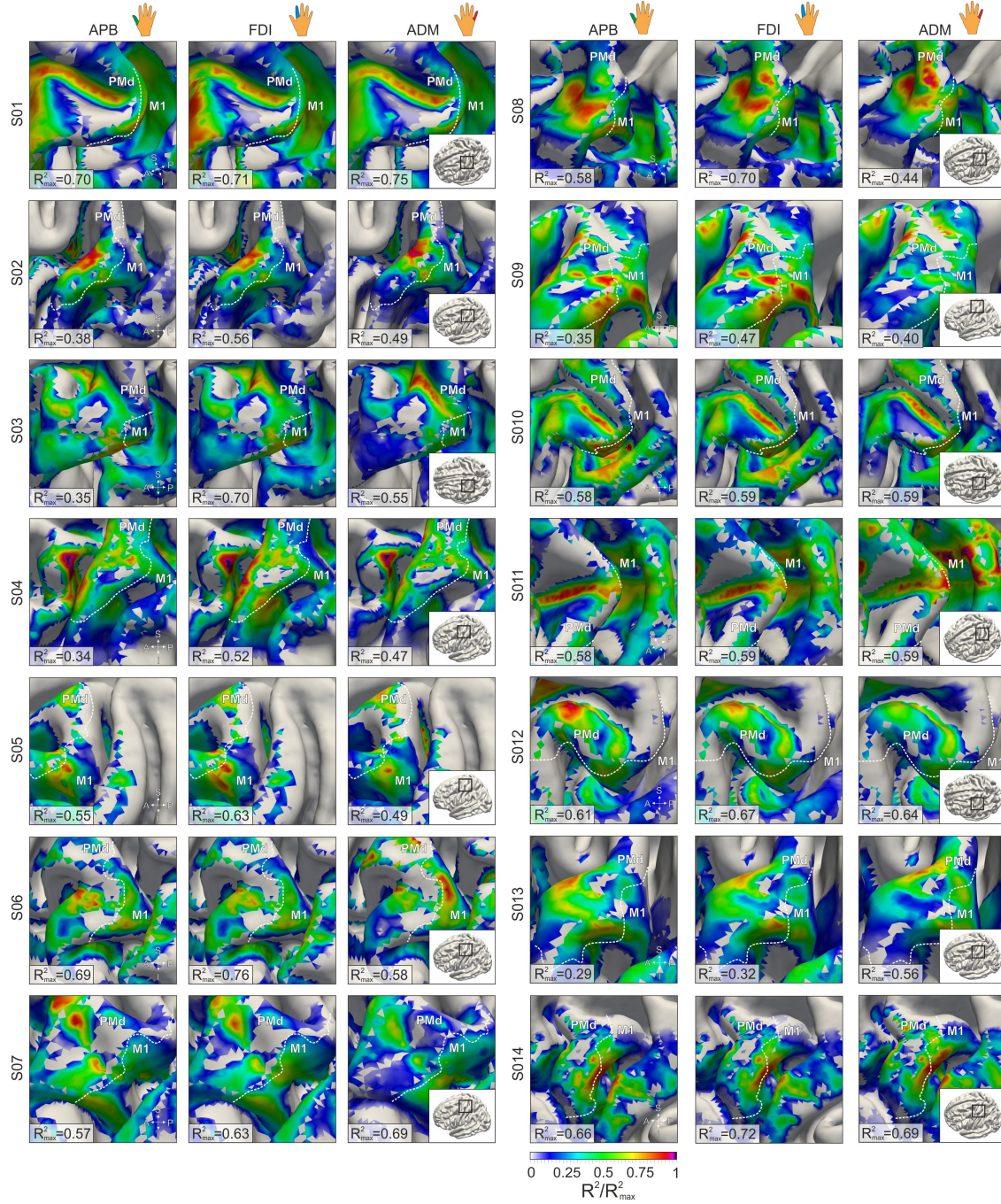
Figure 4.8: The normal component $E_\perp$ does not yield conclusive localizations. In comparison with localization results from both, $|E|$ and $E_\parallel$, the normal e-field component results in low goodness-of-fit values and an overall scattered cortical R^2 map. R^2 scores are normalized to the subject- and muscle-wise maximum R^2_{max} for the e-field magnitude (Figure 4.6). Figure published initially in Numssen, Zier, et al. (2021).

$$\epsilon_{n,ref}^{R^2} = \frac{\sqrt{\frac{1}{N_{elms}} \sum_{i=1}^{N_{elms}} \left(R_{i,n}^2 - R_{i,ref}^2\right)^2}}{max(R_{ref}^2) - min(R_{ref}^2)} \qquad\qquad NRMSD \ (4.5)$$

The geodesic distance ϵ_{ref}^{δ} was calculated with tvb-gdist 2.1.0 (github.com/the -virtual-brain/tvb-gdist). I performed non-parametric permutation tests across all stimulation subsets to estimate the generalizability of the localization method. These were performed against the full set of solutions. Based on this, the lower bound of the number of stimulations needed to reach <5 % error NRMSD could be derived. For the geodesic distance, a criterion of <5 mm was chosen.

4.5.3 Results

For 100 random sequences, I calculated the cortical mapping from $n = 10$ to all available stimulations ($N \approx 1000$). NRMSD and geodesic distance converged exponentially, tested against all available stimulations (n vs. N) and the previous solution (n vs. $n - 1$). The variance across these localizations was large only until $n \approx 50$ and afterward quickly decreased. Between subjects, the convergence properties are similar for the NRMSD metric (Figure 4.9) and more variable for the geodesic distance (Figure 4.10). Across subjects and metrics, localizing FDI was feasible with fewer stimulations than localizing APB and ADM. With non-parametric bootstrapping tests, I identified the number of pulses required to locate cortical muscle representations within a 95 % confidence interval. Tests were performed to compare against all stimulations as a proxy for the ground truth.

134, 113, and 110 stimulations are necessary for APB, FDI, and ADM, respectively, for the overall similarity of R^2 maps (NRMSD) to reach an error <5 %. This n vs. N threshold corresponds to NRMSD values of 2.0 %, 2.0 %, and 2.6 % (APB, FDI, ADM) for comparisons against the previous solution ($n - 1$).
Correct cortical targets can be pinpointed within 5 mm with 277, 185, and 338 (APB, FDI, ADM) stimulations as quantified by the geodesic distance. This n vs. N threshold corresponds to 0.36 mm, 0.37 mm, and 0.40 mm distance when compared against the previous solution (n vs. $n - 1$).
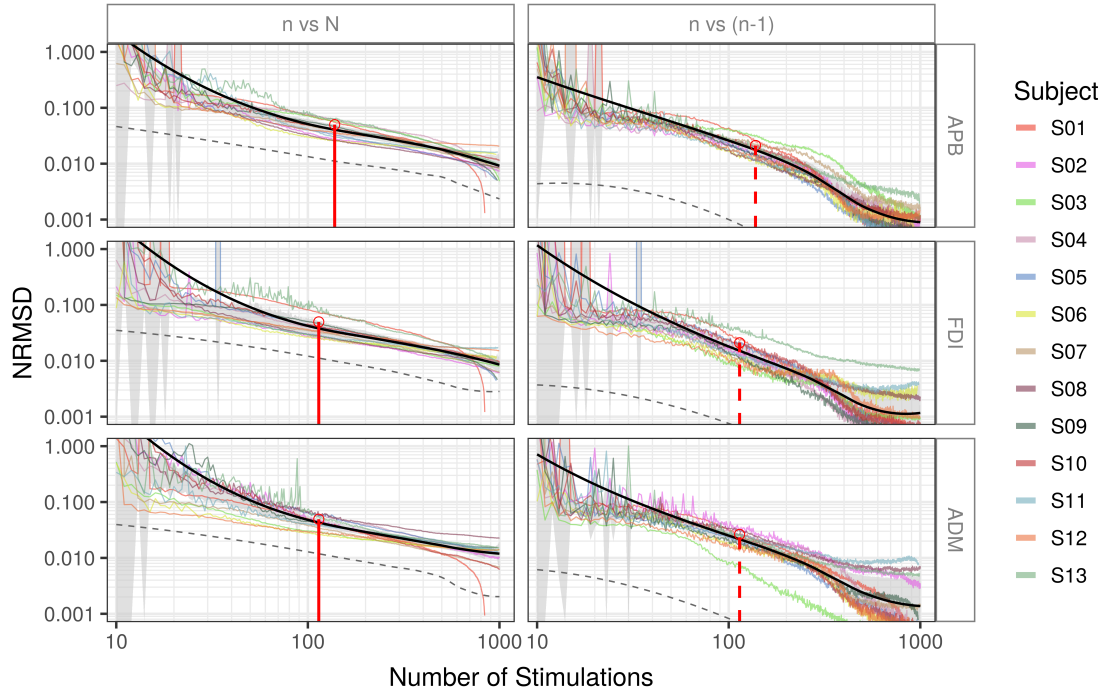
Figure 4.9: Localization maps converge after 120 quasi-random stimulations. The normalized root-mean-square deviation (NRMSD), a proxy of overall similarity, converges exponentially towards the solution from all ≈ 1000 stimulations. About 120 stimulations suffice to reach $<5\%$ error. $<5\% \ NRMSD_{n\,vs\,N}$ is achieved when yielding an $<3\% \ NRMSD_{n\,vs\,n-1}$. Left: NRMSD against the reference solution from all $N \approx 1000$ stimulations. Right: NRMSD against the previous $n-1$ stimulation. Colored lines: subject-wise average convergence (see text). Black line: grand average, smoothed for the sake of visualization. Gray area: confidence interval of the population mean based on non-parametric bootstrapping at $\alpha = 0.95$ level. Dashed gray line: best solution across samples. Red line: number of stimulations needed to reach 5% NRMSD against the reference solution N. Figure published initially in Numssen, Zier, et al. (2021).

4.6 Validation experiment

4.6.1 Data acquisition

After identifying the neuronal population (the '*hotspot*') underlying the observed MEP, i.e., yielding the highest R^2 score, I validated this finding in a second experimental session. Based on e-field simulations, I selected the coil position/orientation, which induced the strongest e-field at the hotspots. This optimization was done for
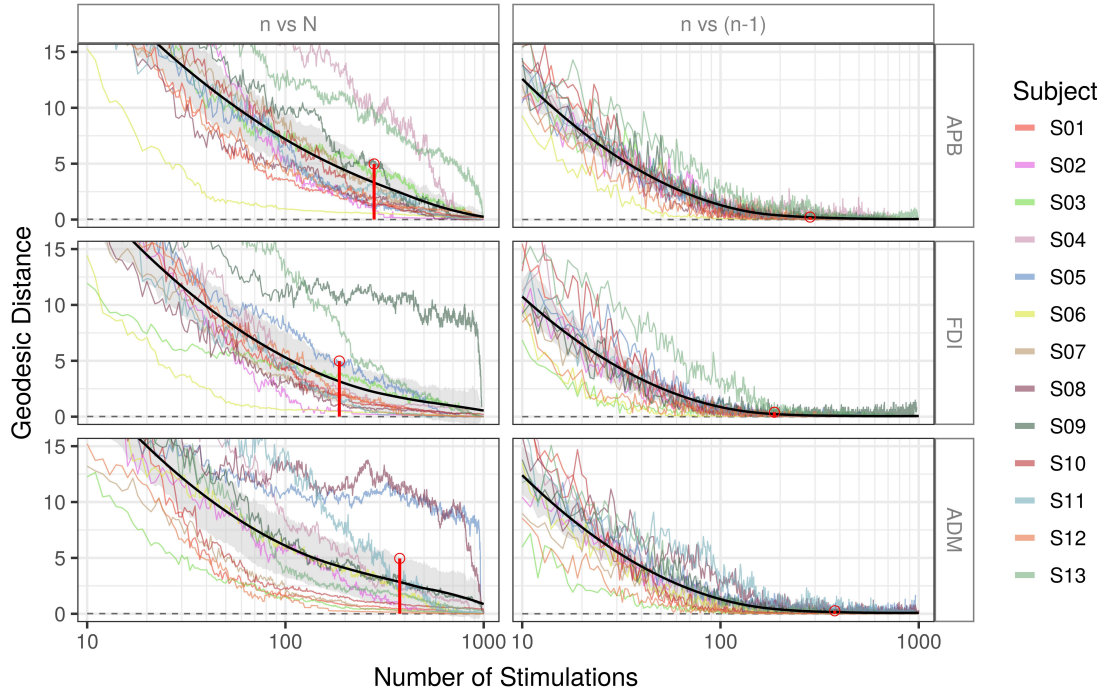
Figure 4.10: 150 random stimulations identify the correct cortical target. Geodesic distance (in mm) from the identified target to the *"true"* target, computed from n to N stimulation (reference solution). The minimum number of stimulations to yield <5 mm error differs across muscles. Left: reference solution is based on all $N \approx 1000$ stimulations. Right: reference is the solution from previous $n - 1$ stimulations. Colored lines: subject-wise average convergence (see text). Black line: grand average. Gray area: confidence interval around the population mean based on non-parametric bootstrapping at $\alpha = 0.95$ level. Gray dashed line: best solution across samples. The number of stimulations needed to reach 5 mm distance against the reference solution N is depicted left (solid red line). Red line: number of stimulations needed to reach 5 mm target distance against the reference solution N. Figure published initially in Numssen, Zier, et al. (2021).

each of the three muscle representations and for each subject individually. RMTs were acquired for these optimal coil positions/orientations and for adjacent ones to verify if stimulation of the proposed hotspots does indeed lead to the largest effect. Optimal coil positions/orientations were determined with an extensive search procedure, comparing e-fields magnitudes of 4852 coil configurations at the hotspot area (search radius = 20 mm, spatial resolution = 2.5 mm, search angle = 180°, angle resolution = 7.5°). The optimization routine is implemented in SimNIBS v3.1 (simnibs.github.io/simnibs) and has been described above (section 3.6).

Single bi-phasic pulses with $5\,\mathrm{s}$ ISI were applied to determine the true rMT. The rMTs for optimal coil configurations were compared to rMTs obtained for six adjacent coil configurations. Two coil configurations shared the same coil center with the optimal one but differed in their coil orientation (-45° and +45°). Four coil configurations shared the optimal coil orientation but were shifted $7.5\,\mathrm{mm}$ in the superior, posterior, inferior, or anterior direction.

4.6.2 Results

At the identified cortical digit hotspots, the adjacent coil positions yielded about $94\,\%$ of the stimulation strength induced by the optimal coil position and the rotated coil positions about $98\,\%$ (see Table 4.3 for details). These relative stimulation differences translate to absolute e-field changes of about $3\,\mathrm{V\,m^{-1}}$ for the shifted stimulation conditions and to differences of about $6\,\mathrm{V\,m^{-1}}$ for the rotated stimulation conditions, respectively. Nine of the 14 initial subjects participated in the validation study (Figure 4.11). In the majority of cases, the rMT for the optimal coil position was the lowest. Because data were not distributed normally (Shapiro-Wilk test: $W = 0.91299$, $p = 4.003 * 10^{-09}$), one Mann-Whitney U test was performed for each muscle. Resting motor thresholds at adjacent positions were significantly higher than rMTs from the optimal, pre-computed coil positions and orientations (APB: $W = 414$, $p = 3.459 * 10^{-04}$; FDI: $W = 455$, $p = 0.147 * 10^{-04}$; ADM: $W = 423$, $p = 1.899 * 10^{-04}$).

4.7 Critical evaluation

I presented an efficient and high-resolution approach to identify causal structure-function relationships with TMS. This approach was applied to map the individual somatotopy of several hand muscle representations in the primary motor cortex (M1). This mapping approach links the induced e-fields at the cortex to a modulated experimental outcome and exploits variance across induced e-fields from multiple stimulation sites.

E-field modeling and biophysically informed analyses allowed to identify strong relationships between e-field magnitude and MEP size at cortical muscle representations in the primary motor cortex (M1). In line with previous work (Weise & Numssen et al., 2020; Aberra et al., 2020), functional hotspots were found on the crowns and rims of the precentral gyrus between BA6 and BA4 for the magnitude and the tangential component of the e-field. For the normal component, similar locations were identified, although with significantly lower goodness-of-fit.
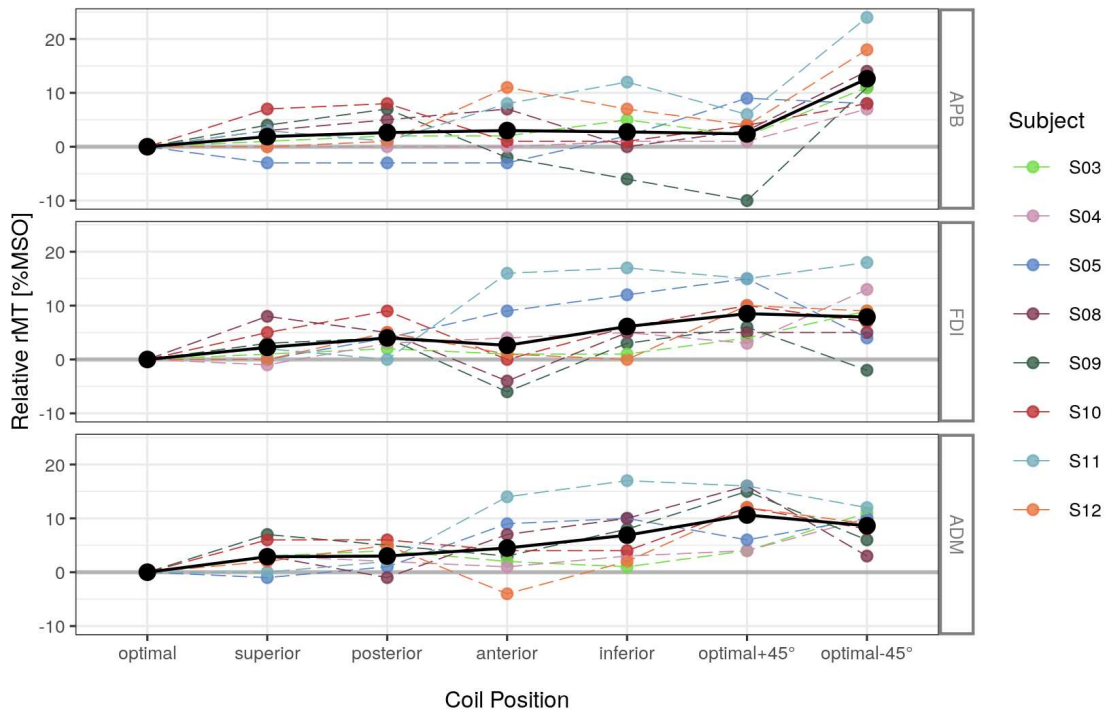
Figure 4.11: Optimized coil positions stimulate the correct cortical location. Resting motor thresholds (rMTs) were assessed for the identified, *optimal* coil positions and six adjacent ones: Four positions with the same optimal coil orientation (*superior*, *posterior*, *anterior*, *inferior*) and two coil orientations at the optimal coil center position (*optimal-45˚*, *optimal+45˚*). The optimal coil position yielded the lowest rMT value for most subjects and conditions, thus proving the correct identification of the cortical muscle representations. RMTs for each position/orientation are normalized to $rMT_{optimal}$ per subject and muscle. Color: subject id. Black line: average rMT. %MSO: Percentage of maximum stimulator output. APB: thumb muscle. FDI: index finger muscle. ADM: little finger muscle. Explicit rMT values are provided in Table 4.3. Figure published initially in Numssen, Zier, et al. (2021).

Table 4.3: Resting motor thresholds (rMTs) determined in the validation study.

Subject	Target	Coil condition						
		opt	opt-45°	opt+45°	pos	ant	inf	sup
	FDI	**42**	47	46	44	41	43	43
S03	ADM	**40**	53	46	44	44	43	43
	APB	**42**	53	**42**	44	44	45	43
	FDI	36	49	39	39	40	41	**35**
S04	ADM	**36**	46	40	38	37	39	39
	APB	**36**	43	37	**36**	**36**	37	**36**
	FDI	**48**	52	64	52	57	61	**48**
S05	ADM	48	59	54	49	58	58	**47**
	APB	49	56	57	46	**45**	50	46
	FDI	**52**	64	60	57	55	60	60
S08	ADM	59	**58**	68	**58**	62	62	62
	APB	**55**	66	62	60	59	59	58
	FDI	**47**	53	54	51	49	51	50
S09	ADM	55	54	62	60	**51**	55	62
	APB	48	58	**45**	55	**45**	49	52
	FDI	**42**	50	50	51	43	46	47
S10	ADM	**43**	48	54	49	44	46	49
	APB	**40**	50	47	48	43	44	47
	FDI	**72**	90	87	**72**	88	89	74
S11	ADM	**72**	84	88	74	86	89	**72**
	APB	**72**	96	78	73	80	84	75
	FDI	**46**	56	60	51	48	50	**46**
S12	ADM	47	59	58	52	**46**	48	49
	APB	**50**	64	51	51	57	54	**50**
	FDI	**35**	46	40	40	36	37	44
S14	ADM	**43**	50	44	44	45	44	48
	APB	**41**	50	**41**	43	42	42	46

Notes: opt: optimal coil position including ±45° orientations; *pos, ant, inf,* and *sup*: *posterior, anterior, inferior,* and *superior* coil position. Each shifted by 7.5 mm with respect to the optimal coil position. Minimum rMTs highlighted in bold.

By assessing the convergence behavior of the proposed mapping approach, I was able to estimate a lower bound for the number of quasi-random stimulations needed: About 150 pulses from quasi-random coil positions and orientations suffice to obtain robust cortical maps. This yields a mapping duration of less than 15 minutes. In contrast to

an overall cortical probability map, pinpointing single muscle representations requires between 190 (FDI) and 340 (ADM) pulses on average, with significant inter-subject variability. Knowledge about these convergence properties allows quantifying the overall mapping quality of any future muscle mapping. Specifically, the normalized root-mean-square deviation between all realized stimulations versus all but one stimulation ($N \approx 1000$) should be as low as 2% to guarantee valid mapping results.

This mapping approach was designed to increase the variance between e-field distributions by allowing quasi-random coil positions and orientations. The integration of information from many, quasi-random coil configurations solves the problem of a missing criterion to define coil configurations a priori (Weise & Numssen et al., 2020), increases the information gain per pulse, and thus substantially reduces the minimum number of stimulations for a robust localization. Allowing random coil positions and orientations instead of acquiring entire input-output curves for predefined coil positions/orientations establishes a highly efficient and robust experimental protocol. Its implementation in a standard TMS laboratory is straightforward because of the independence from any predetermined coil positions/orientations. Thus, this approach is better suited for practical and clinical use than previously proposed mapping approaches. To further ease the implementation in real-world scenarios, I provide an extensive set of analyses scripts and peer-reviewed implementation informations in the following chapter. Functional localizations based on e-field-behavior relationships are, in principle, possible in any brain region that produces a quantifiable outcome measure, thus excluding severely impaired regions, for example, after stroke. I present an exemplary application to locate attentional orientation processes in the discussion.
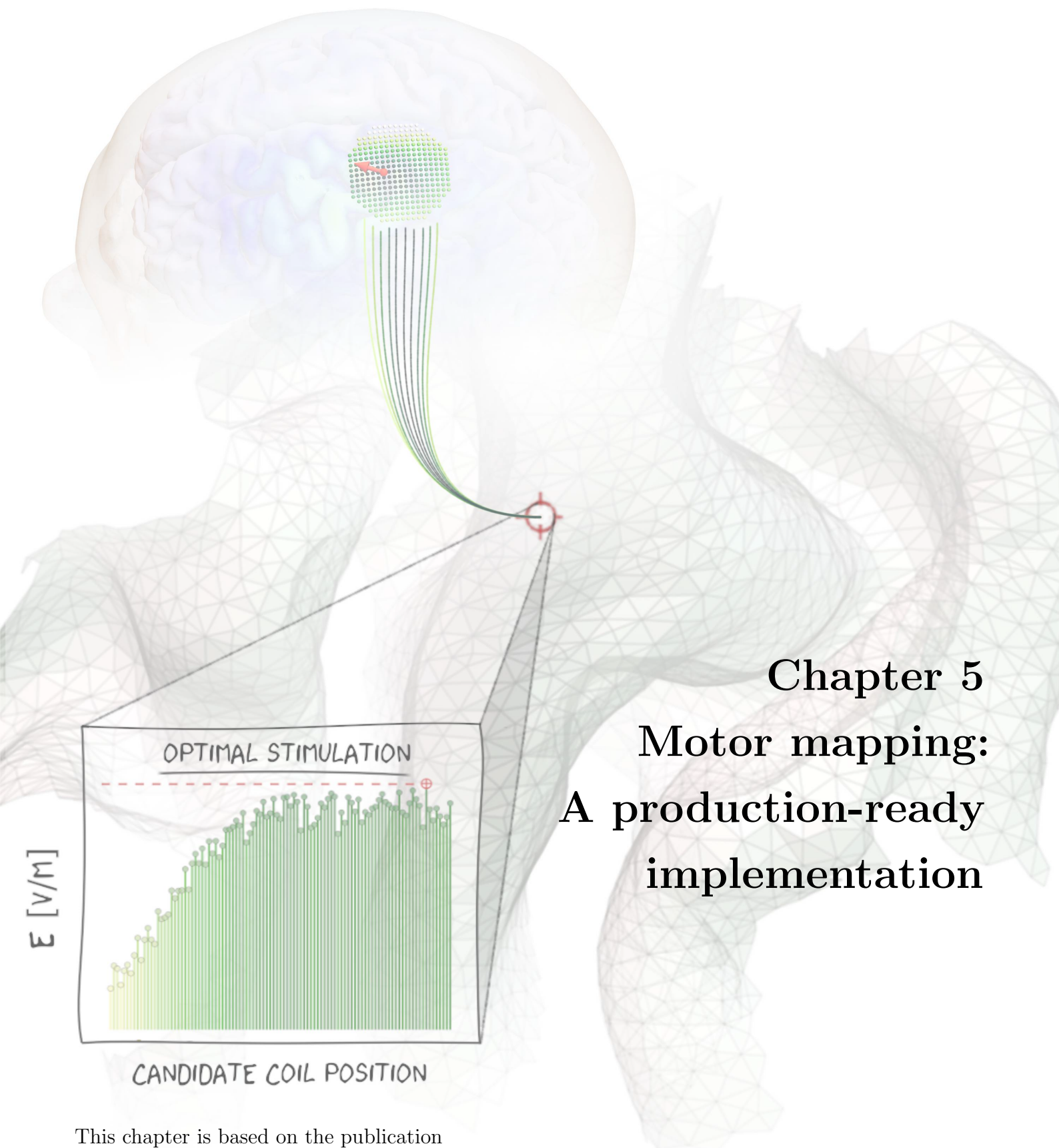
Chapter 5
Motor mapping:
A production-ready
implementation

5.1 Overview

After presenting the rationale and the methodological implementation above, I present detailed information on how to apply this cortical mapping approach in a realistic scenario. To further facilitate the application of this procedure, I provide a comprehensive set of scripts to perform the mapping in an online repository (gitlab.gwdg.de/tms-localization/papers/tmsloc_proto) and a sample data set for a single subject (doi.org/10.17605/osf.io/myrqn; Numssen et al., 2022).

At first, details on how to construct the individual head mesh to compute the TMS-induced e-fields are presented (Stage 1, step 1 – step 20). Second, a manual rMT estimation is performed, followed by TMS pulses at quasi-random coil positions and orientations (Stage 2, step 21 – step 41). Third, the experimental data is post-processed, all e-fields are computed for the realized coil positions and orientations, and the elicited MEPs are extracted (Stage 3, step 42 – step 48). The steps above yield the input data to pinpoint the cortical muscle representations via non-linear regression of the cortical e-field onto the MEP amplitudes (Stage 4, step 49 – step 53). As a final, optional step, a cortical e-field threshold can be calculated to allow precise supra-threshold neuronal stimulation (Stage 5, step 54 – step 56) at any cortical target.

5.2 Materials and methods

5.2.1 Experimental design

An overview of the experimental design and the general workflow is shown in Figure 5.1. The procedure starts with a preparation phase, including legal obligations, acquisition of MRI scans, construction of the individual head model, and definition of a cortical region of interest (ROI). T1 images are mandatory for the construction of the head models, but segmentation accuracy can be considerably increased with additional T2 images (Puonti et al., 2020). Additionally, diffusion weighted images (DWIs) can be used to assign anisotropic conductivity tensors to gray matter (GM) and white matter (WM). This leads to a more realistic modeling approach yielding up to 7 % change of the e-field magnitude on average and up to 40 % locally for

white matter regions. The effect of additional DWI scans is less pronounced for gray matter regions (Opitz et al., 2011). After the MRI acquisition session, the volunteer is invited to the first TMS session. Preparations include placement of the EMG electrodes and configuration of the EMG and the neuronavigation recordings. After defining the stimulation area, data is recorded for 300 quasi-random pulses from coil positions/orientations. The acquired data is post-processed by calculating peak-to-peak MEP amplitudes from the EMG recordings. The induced e-fields of the realized coil positions and orientations are calculated. Afterward, the e-fields are fitted to the MEP amplitudes with sigmoidal neural response curves to yield element-wise goodness-of-fit statistics (R^2 score) in the cortical ROI. R^2 hotspots are interpreted as the cortical MEP origin. Optionally, the coil position and orientation optimally stimulating this location can be calculated for a follow-up TMS session to determine the precise resting motor threshold (rMT) and the cortical e-field threshold.

An up-to-date computational infrastructure and a laboratory equipped with a standard TMS neuronavigation system and EMG recording hardware and software are required. This protocol offers a ready-to-use solution to map finger muscle representations in the primary motor cortex with the specified hardware and software. Applications to other laboratory systems and different modalities require protocol adjustments and are discussed below.

DEFINING THE STIMULATION TARGET AREA. The mapping approach exploits the variance of induced e-fields and the resulting MEPs. Crucially, the realized stimulation positions/orientations and the MEPs have to cover the whole range of the cortical I/O curve, i.e., low e-field strength yielding no or small MEPs up to high e-field strength yielding MEPs from the upper saturation plateau (around 4 mV). The TMS coil is positioned at multiple positions and orientations around M1 to cover the whole cortical I/O curve with constant stimulator intensity. A sampling area of about 5 cm * 5 cm with a stimulator intensity of 150 % rMT yields sufficient data (steps 34–37).
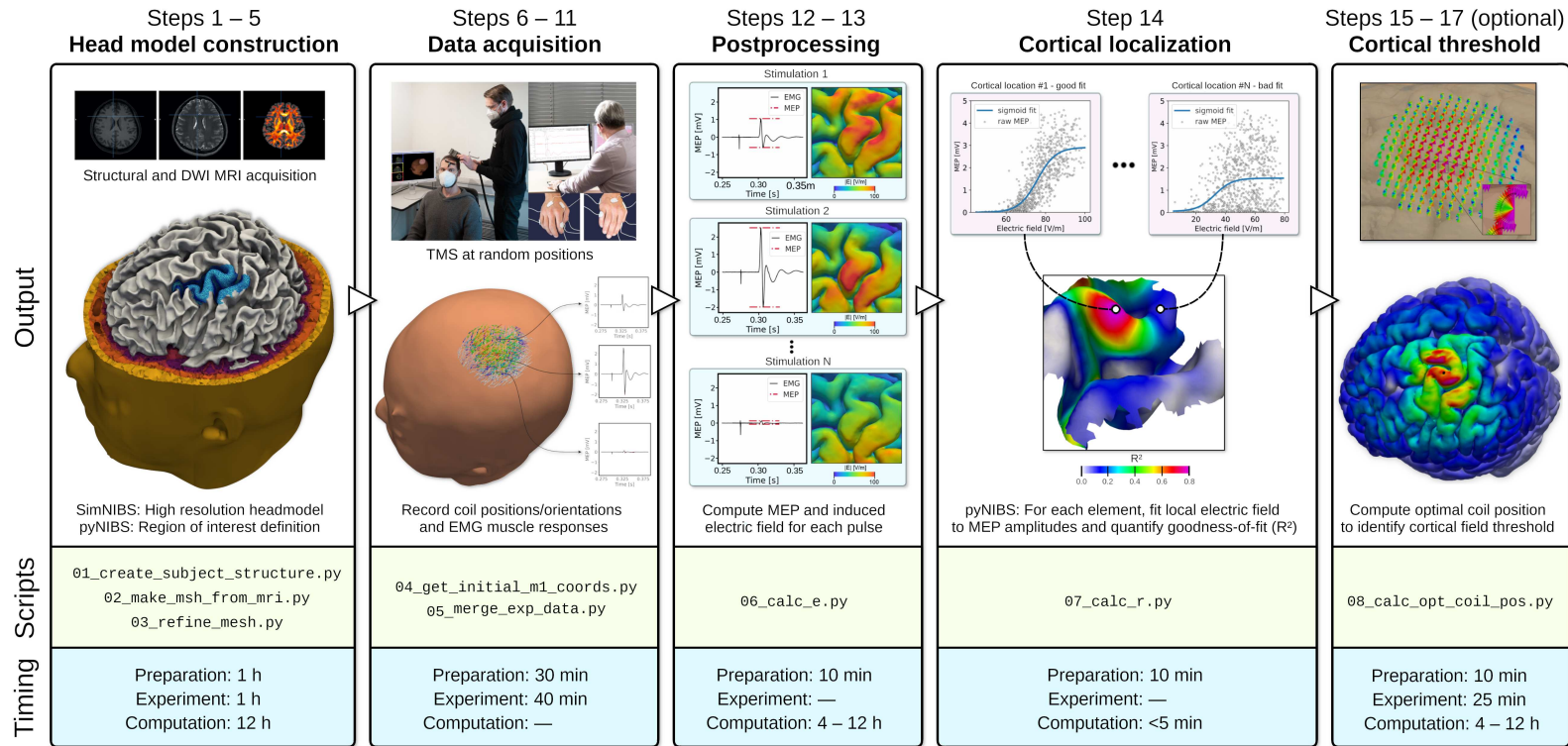
Figure 5.1: The cortical localization comprise five major stages of data acquisition and processing.
The individual headmodel construction is the basis for all subsequent e-field and R^2 analyses. During the data acquisition TMS pulses are applied at random positions around the cortical target, in this case the primary motor cortex (M1). MEPs from multiple muscles can be recorded simultaneously. The cortical muscle representations are identified by the goodness-of-fit between local e-field exposure and MEP amplitude. Optionally, a cortical e-field threshold can be computed. Figure published initially in Weise & Numssen et al. (2022).

TUNING THE FIT PROCEDURE. After data acquisition and postprocessing, the relationship between the induced e-field and the resulting MEP is quantified for each cortical location in a region of interest. The relationship is assessed by fitting one of several pre-defined function types to the data, which can yield significant computational costs depending on the size of the region of interest and data points. The set of pre-defined functions can be extended and currently spans from simple linear regression to multiple sigmoidal function types. Whereas linear functions allow a fast fitting procedure, these are also highly susceptible to suboptimal data acquisition, i.e., not covering the complete cortical I/O curve. For mappings of muscles other than the ones presented here (ADM, FDI, or APB) or for use in clinical populations, different function types might have to be implemented, or the initial fit parameters might have to be adjusted.

ADAPTATIONS TO OTHER LABORATORY SETUPS. The underlying rationale of this mapping approach does not per se depend on specific laboratory hard- and software. Any reliable TMS neuronavigation that can export coil positions for single TMS pulses may, in principle, be used. The presented protocol is written for a TMS Navigator (Localite GmbH, Bonn, Germany) neuronavigation system with a CED Signal EMG recording environment (Cambridge Electronic Design Limited, Cambridge, England). Other systems require adaptations of the analysis scripts. The provided scripts allow data import from Brainsight (Rogue Research, Québec, Canada) and Visor (ANT Neuro, Hengelo, Netherlands) neuronavigation systems, requiring only small adjustments of the experimental procedure, such as data export. Similarly, other EMG recording systems can be utilized to record physiological responses as long as the user provides the necessary data import functions. The script `05_merge_exp_data.py` interfaces the post-processing routines to proprietary data formats and can be adapted to individual needs. Due to the intense utilization of the SimNIBSsoftware, using a different meshing tool or FEM solver would require major changes in the analysis pipeline.

ADAPTATIONS TO OTHER OUTPUT QUANTITIES. This protocol was developed and tested with EMG responses from three finger muscles (ADM, FDI, and APB). When mapping other body muscles, e.g., leg or lip muscles, a correct stimulation intensity must be chosen to elicit sufficiently large MEPs from the upper saturation plateau.

In addition, a different number of stimulations might be necessary, depending on the noise floor of the EMG and the intrinsic variance of the MEPs.

5.2.2 Expertise needed to implement the protocol

Two TMS-trained experimenters can perform the experimental part of the protocol. Training must include awareness of TMS-related safety aspects (Rossi et al., 2021).

5.2.3 Limitations

This protocol was developed in the motor system of healthy volunteers. Motor representations may differ in lesioned brains, e.g., in tumor or stroke patients. In tumor patients, the segmentation algorithms for creating the head model must be adapted accordingly due to non-standard tissues and tissue distribution. In both groups, lesions need to be considered and potentially be masked out. High-quality MRI scans with minimal head movement are obligatory to guarantee accurate e-field simulations. MRI scanners with a field strength of at least 1.5 T (3 T preferable) suffice to achieve an adequate resolution (typically 1 mm^3) and signal-to-noise ratio. The general mapping procedure can be adapted to other functional domains outside the motor cortex and may be transferred to clinical applications only if the criteria discussed above are met. The number of necessary stimulations and, therefore, the mapping time increases with higher noise levels in the behavioral response. The localization accuracy is negatively affected by errors of the neuronavigation system, such as poor coil calibrations and volunteer registrations.

5.2.4 Materials

Volunteers

- Human volunteers with no contraindications for MRI and TMS may be recruited and must be screened by trained medical personnel following established guidelines (Rossi et al., 2021; Bikson et al., 2020) and documented accordingly. Only healthy, right-handed volunteers should be included (Kleim et al., 2007; Rossi et al., 2021). For clinical populations, a physician has to decide whether TMS is applicable. The experiments in Weise & Numssen et al. (2020) and Numssen, Zier, et al. (2021) were approved by the local Ethics committee

of the Medical Faculty of the University of Leipzig.

The principal investigator has to follow all applicable regulations, possibly including approval by a local Institutional Review Board or similar, obligations by national data protection regulations, insurance-related requirements, and others.

Informed written consent must be obtained from all volunteers prior to the experiments.

- All analyses are performed at the subject level.

Hardware

- 1.5 T or 3 T (preferred) MRI scanner
- TMS Stimulator (used here: X100, MagVenture GmbH, Willich, Germany)
- Stereotaxic neuronavigation system (used here: TMS Navigator, Localite GmbH, Bonn, Germany)
- Figure-of-eight TMS coil (used here: C-B60 and MCF-B65, MagVenture GmbH, Willich, Germany)

  This protocol was developed using a MagVenture X100 stimulator, bi-phasic pulse shape, and a MagVenture MCF-B65 coil.

  Other coil sizes, coil shapes, or pulse shapes will influence TMS measures (Pascual-Leone et al., 2002; Sommer et al., 2006; Kammer et al., 2001) and likely lead to different numbers of stimulations needed due to higher or lower e-field variance.
- Foam ear plugs
- Tape
- Self-adhesive single-use surface belly-tendon EMG electrodes (e.g., Neuroline 710, Ambu GmbH, Bad Nauheim, Germany)
- EMG amplifier (e.g., D-360, Digitimer Ltd., Welwyn Garden City, UK)
- Analog to digital converter (e.g., Power1401 MK-II, CED Ltd., Cambridge, UK)
- EMG recording software (e.g., Signal, Cambridge Electronic Design Ltd, version 4.11, Cambridge, UK)
- Workstation ($\geq$ 4 CPU cores, 16GB RAM, 500GB disc space per subject

Software

- Operating system: 64 bit Linux (tested on Ubuntu $\geq$ 16.04), MacOS $\geq$ 10.14, or 64 bit Windows $\geq$ 7. Computations of (optional) diffusion tensors during the head model construction for anisotropic e-field calculations currently (SimNIBS 3.x) require FSL, which only runs on Linux, MacOS, or Windows Subsystem for Linux (WSL).
- Python $\geq$ 3.7 environment, www.python.org
- SimNIBS 3.2.6 for head model construction and e-field FEM, www.simnibs.org
- pyNIBS, for pre- and post-processing, gitlab.gwdg.de/tms-localization/pynibs
- Matlab $\geq$ 7.4 for mesh construction with SimNIBS, www.mathworks.com
- Optional: IMporter tool to import InstrumentMarker files into Localite neuronavigation system, gitlab.gwdg.de/tms-localization/importer
- Optional: FSL $\geq$ 5.0.5 to construct diffusion tensors for anisotropic e-field calculations, fsl.fmrib.ox.ac.uk
- Optional: FreeSurfer $\geq$ 5.3.0 to define regions of interest from the FsAverage template, surfer.nmr.mgh.harvard.edu
- Analyses scripts and installation instructions, gitlab.gwdg.de/tms-localization/papers/tmsloc_proto
- Example data set, www.doi.org/10.17605/osf.io/myrqn, Numssen et al. (2022)

See the online repository gitlab.gwdg.de/tms-localization/papers/tmsloc_proto for detailed installation instructions.

5.3 Procedure

I provide all scripts needed to perform this protocol gitlab.gwdg.de/tms-localization/papers/tmsloc_proto and an exemplary data set for a single subject from a previous study (chapter 4; Numssen et al., 2022). Information on installing the necessary software, i.e., a Python environment, the head modeling and e-field simulation software SimNIBS, and the pyNIBS python package for pre- and post-processing is also provided there (`installation.md`). The provided scripts accompany this protocol and are documented extensively. All paths and folders in this chapter refer to the repository root folder.

5.3.1 Stage 1 – Head model construction

Volunteer clearance

STEP 1. Obtain written informed consent from the volunteer for all subsequent procedures. Follow safety guidelines, applicable national laws, and possible insurance requirements (see subsubsection 5.2.4.1) while performing the medical screening.

MRI acquisition

The example data set (10.17605/osf.io/myrqn, Numssen et al., 2022) contains high-resolution T1-weighted and T2-weighted images, a DWI scan, and a complete list of the MRI sequence parameters.

STEP 2. Acquire a T1-weighted image (Figure 5.2a) as precise head models are constructed from high-resolution (at most 1 mm³ voxel size) structural MRI scans. A 3 T MRI scanner with a 32-channel head coil yields sufficient image quality.

STEP 3. Acquire a T2-weighted image (Figure 5.2b) with the same voxel size to improve skull segmentation (Puonti et al., 2020; Nielsen et al., 2018). This is strongly recommended to improve the accuracy of the head tissue segmentation.

STEP 4. To increase the accuracy of the e-field calculations, use DWI data to provide conductivity anisotropy information to complement the T1-weighted and T2-weighted images Figure 5.2c.

Creating the subject-object file

Data organization of the individual volunteers is done with the pyNIBS package by using subject-objects. These are defined by a human-readable file (e.g., `create_subject_0.py`). The example data set (Numssen et al., 2022) provides an example of a fully configured subject-object file. In the following, the general procedure to create a new subject is described.

(a) (b) (c)
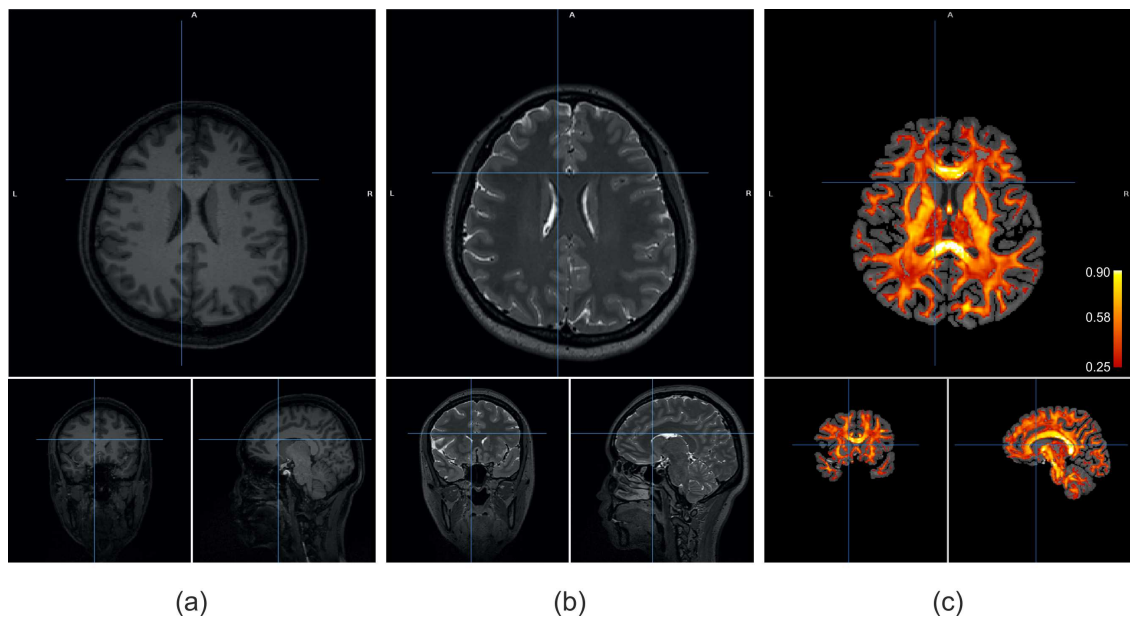
Figure 5.2: Example MRI data for `subject_0` used for head model construction and e-field modeling. a) High-resolution T1-weighted MR image. b) High-resolution T2-weighted MR-image. c) Fractional anisotropy map from a DWI scan. Figure published initially in Weise & Numssen et al. (2022).
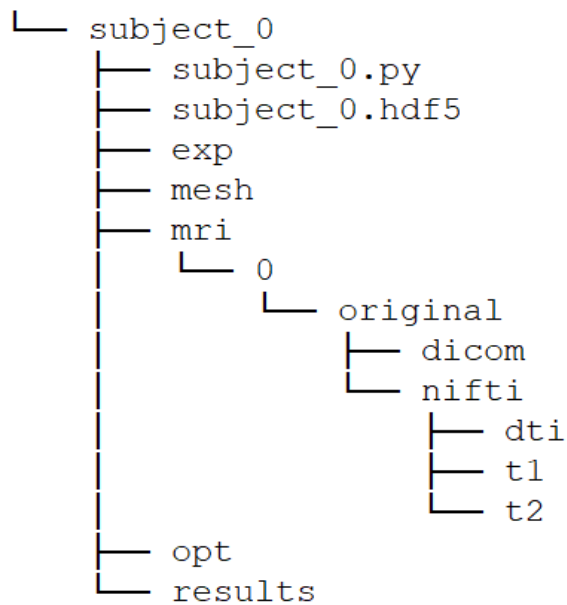
Figure 5.3: Initial folder structure to store MR images, head models, and experimental data for example subject. Figure published initially in Weise & Numssen et al. (2022).

STEP 5. Execute `01_create_new_subject.py` to create a new subject-object
template file and the folder structure as shown in Figure 5.3.

```
> python scripts/01_create_subject_structure.py -f /path/to/subject_0
```

STEP 6. Convert MRI scans into the NIfTI `.nii` format (Li et al., 2016) with
dcm2niix and copy these to the subfolders of `subject_0/mri/0/original/`
`nifti/`.

STEP 7. Edit `create_subject_0.py` and add the NIfTI filenames and image
properties in the `mri` section (Listing 5.1).

STEP 8. Enter the `dti_readout_time` as stated in the `.yaml` file from `dcm2niix`.

```
33  # MRI information
34  mris = dict()
35
36  # we could have several MRI sets, but for now we'll only use one.
37  mris[0] = dict()
38  mri_dir = 'mri/0/original/nifti/'
39  mris[0]['fn_mri_T1'] = f'{sub_dir}/{mri_dir}t1/T1.nii'
40  mris[0]['fn_mri_T2'] = f'{sub_dir}/{mri_dir}t2/T2.nii'
41  mris[0]['fn_mri_DTI'] = f'{sub_dir}/{mri_dir}dti/DTI.nii'
42  mris[0]['fn_mri_DTI_rev'] = f'{sub_dir}/{mri_dir}dti/DTI_rev.nii'
43  mris[0]['fn_mri_DTI_bvec'] = f'{sub_dir}/{mri_dir}dti/DTI.bvec'
44  mris[0]['fn_mri_DTI_bval'] = f'{sub_dir}/{mri_dir}dti/DTI.bval'
45  mris[0]['dti_readout_time'] = '0.0476258'
46  mris[0]['dti_phase_direction'] = '-y'
```

Listing 5.1: MRI section of `create_subject_0.py`.

STEP 9. Enter the mesh information in the mesh section as shown in Listing 5.2.
Mesh resolution can be controlled with the `vertex_density` parameter to set
the vertex density of the surface meshes in nodes per mm^2. For 0.5, 1.0, and 2.0
nodes per mm^2, the resulting head meshes will contain around 4, 9, and 18 million
tetrahedra, respectively. A density of 1 node per mm^2 is recommended.

```
48   # mesh specifications
49   meshes = dict()
50
51   # Create 'mesh0' with default arguments
52   meshes['mesh0'] = dict()
53   meshes['mesh0']['info'] = 'headreco v1.0 (simnibs 3.2.5)'
54   meshes['mesh0']['approach'] = 'headreco'
55   meshes['mesh0']['vertex_density'] = 1.0
56   meshes['mesh0']['mri_idx'] = 0
```

Listing 5.2: Mesh definition in `create_subject_0.py`.

Defining the region of interest

To speed up the data analyses, a region of interest (ROI) is created for an a-priori-defined brain area. The ROI is typically defined halfway between the gray and white matter surfaces, the *midlayer* , because e-field estimates (step 13) are more robust here compared to tissue boundaries. These differences in accuracy stem from discontinuities in the electric conductivity at tissue transitions and, consequently, in the e-field between different tissue compartments. A ROI can be defined based on the subjects' masks from MNI or FreeSurfer (surfer.nmr.mgh.harvard.edu; Dale et al., 1999; Fischl et al., 1999) FsAverage templates. Here, an FsAverage ROI template file is used, covering the left somatosensory cortex (BA1, BA1, BA3), the left primary motor cortex (M1/BA4), and the dorsal premotor cortex (PMd/BA6). This file is provided with other examples in the example data set (`roi/lefthandknob` `_M1S1PMd.overlay`). Use `roi/righthandknob_M1S1PMd.overlay` for the right M1 region, e.g., for left-handed volunteers.

STEP 10. Add the ROI information to the `create_subject_0.py` script (Listing 5.3), including the filenames of GM, WM, midlayer surfaces, and of the individual ROI mask.

STEP 11. Enter the path to the template ROI `.overlay` file in `fn_mask_avg`. The template ROI is later (step 5) transformed to the individual subject space, and a subject-specific `.mgh` mask file is created in `fn_mask`. This transformation can be skipped for the example subject by copying the provided file `mask_lefthandknob` `_M1S1PMd.mgh` to the `midlayer_m1s1pmd` folder in case FreeSurfer is not installed. See the TMSloc_proto repository for information on how to construct study-specific

ROIs, for example, based on group fMRI results.

```
70  # region of interest specification
71  rois = dict()
72
73  # create a roi 'midlayer_m1s1pmd' for 'mesh0'
74  rois['mesh0'] = {'midlayer_m1s1pmd': dict()}  # each ROI is mesh
    ↪   specific.
75
76  # by default, the ROI is resampled to midlayer GM
77  rois['mesh0']['midlayer_m1s1pmd']['type'] = 'surface'
78  rois['mesh0']['midlayer_m1s1pmd']['info'] = 'freesurfer PMd, M1 and
    ↪   somatosensory cortex'
79  rois['mesh0']['midlayer_m1s1pmd']['hemisphere'] = 'lh'
80
81  # provide filename for midlayer geometry
82  rois['mesh0']['midlayer_m1s1pmd']['midlayer_surf_fname'] =
    ↪   f'fs_{subject_id}/surf/lh.central'
83
84  # ROI .mgh definition in subject space
85  rois['mesh0']['midlayer_m1s1pmd']['fn_mask'] =
    ↪   f'roi/midlayer_m1s1pmd/mask_lefthandknob_M1S1PMd.mgh'
86
87  # ROI in fsaverage space (for bookkeeping reasons)
88  rois['mesh0']['midlayer_m1s1pmd']['fn_mask_avg'] =
    ↪   os.path.join(os.path.split(sub_dir)[0],'ROI',
    ↪   'lefthandknob_M1S1PMd.overlay')
```

Listing 5.3: ROI section of `create_subject_0.py`.

STEP 12. Finally, execute `create_subject_0.py` to create the `subject_0`
`.hdf5` subject-object file.

```
> python subject_0.py
```

Execute this script again after any changes to update the subject-object file. The
example data set contains a fully configured subject-object file for comparison.

Constructing the head model

The quality of the head model strongly affects the accuracy of the e-field calculations
and should be inspected visually for correctness and plausibility.

STEP 13. Construct the head model and the conductivity tensors from the acquired
MR images by executing the following script. This utilizes the headreco pipeline
of SimNIBS to segment the MRI scans into different tissue types and creates a
volumetric head mesh. Diffusion tensors are reconstructed in GM and WM if a DWI
scan is provided.

```
> python scripts/02_make_msh_from_mri.py -s subject_0.hdf5 -m mesh0


Parameters:
    -s : Path to subject-object file
    -m : Mesh ID
```

STEP 14. The mesh will be saved in the folder subject_0/mesh/mesh0. Visually
inspect the quality of the meshing procedure. This shows the reconstructed surfaces
overlaid on the raw MRI data. Pay special attention to a good alignment of tissue
boundaries and surfaces, as these critically impact the e-field computation.

```
> headreco check subject_0
```

STEP 15. Inspect the normalization accuracy to the MNI template via the anatomical
overlay shown.

STEP 16. Load the .xdmf file of the final head mesh with the visualization tool
ParaView (Geveci, 2005; Ayachit, 2015) to inspect the quality of the mesh.

STEP 17. Check the geometric integrity of the head model via Gmsh (Geuzaine &
Remacle, 2009). No invalid elements (negative or zero volume/surface area) must
exist in the mesh.

```
> gmsh check subject_0.msh
```

STEP 18. The use of diffusion tensors is optional and can increase the accuracy of
the e-field calculations (Opitz et al., 2011). Visualize the reconstruction of diffusion
tensors from the DWI data with:

```
> dwi2cond -c subject_0
```

STEP 19. Superimpose the fractional anisotropy (FA) image before and after
preprocessing on the subject's anatomical scan with fslview or fsleyes to inspect the
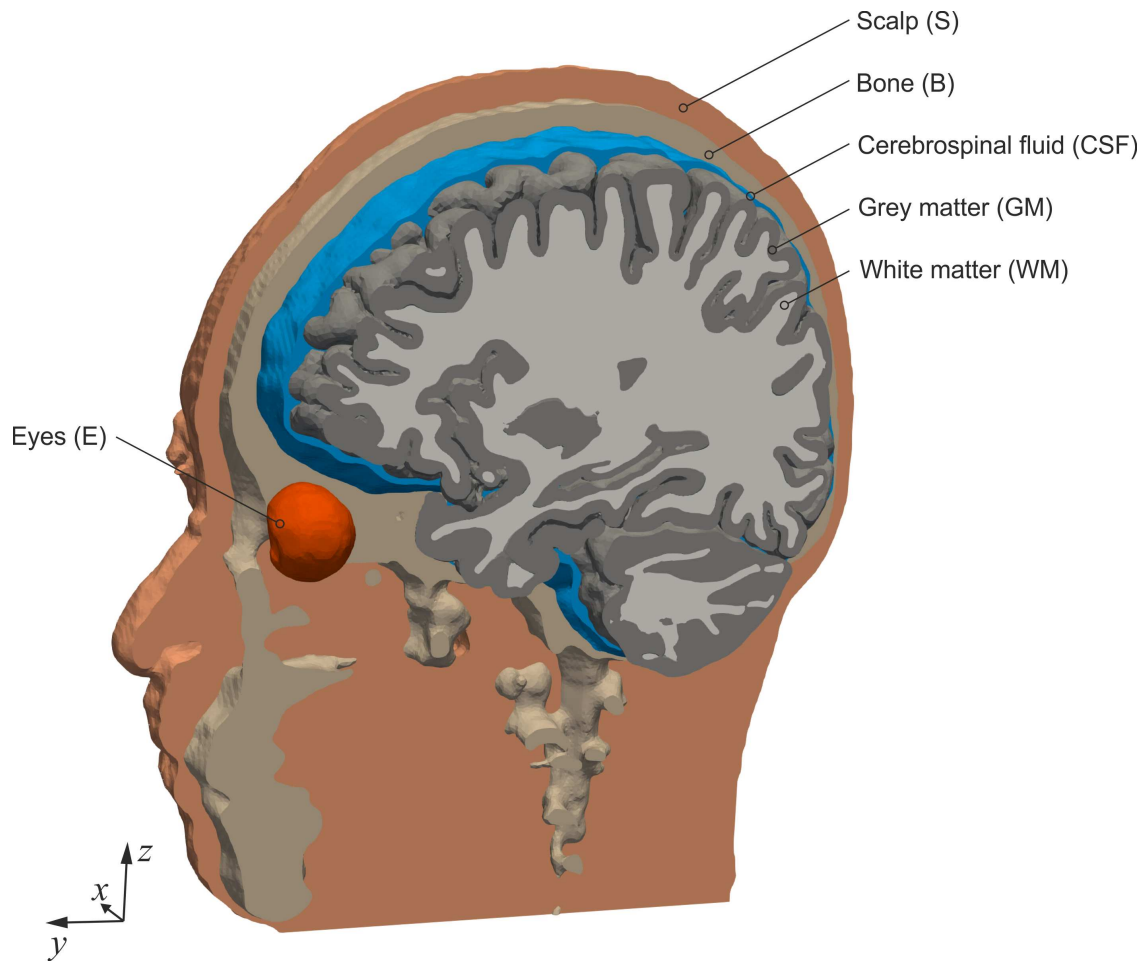
Figure 5.4: Head model from the example data set `subject_0` constructed with the headreco pipeline. Figure published initially in Weise & Numssen et al. (2022).

co-registration visually. The final mesh from the example data set with its six tissue types is visualized in Figure 5.4. Here, a vertex density of 1.0/mm yielded 10 832 185 tetrahedra and 1 620 479 nodes.

STEP 20. After constructing the head model, the mesh should be refined in relevant regions to increase the accuracy of the e-field estimation in these areas. Edit the `create_subject_0.py` script, add a new refined mesh (Listing 5.4) `mesh0\_refinedM1`, and set the `refine_domains` parameter to increase mesh density in CSF, GM, and GM within the specified sphere. Here a point on the skin surface of the SimNIBS-processed T1 image is chosen (`subject_0/mesh/mesh0 _refinedM1/subject_0_T1_conform.nii.gz`) above the primary motor cortex

as the center of the refined area. Add the ROI to the refined mesh as well (Listing 5.5).
In addition to refining the mesh in the region of interest, the skin surface is smoothed
by setting `smooth_domains` to `'skin'`. A smooth skin surface is required when
determining the optimal coil position in step 15 because the induced e-field in the
cortex is highly sensitive to changes in the coil distance.

```
58   # Create a second mesh, 'mesh0_refinedM1' ...
59   meshes['mesh0_refinedM1'] = dict()
60   meshes['mesh0_refinedM1']['info'] = 'headreco v1.0 (simnibs 3.2.5)'
61   meshes['mesh0_refinedM1']['approach'] = 'headreco'
62
63   # ... and set refinement specific parameters
64   meshes['mesh0_refinedM1']['center'] = [-31.17, -45.68, 73.47]
65   meshes['mesh0_refinedM1']['radius'] = 35  # radius of refinement
66   meshes['mesh0_refinedM1']['element_size'] = 0.4
67   meshes['mesh0_refinedM1']['refine_domains'] = ['wm', 'gm', 'csf']
68   meshes['mesh0_refinedM1']['smooth_domains'] = ['skin']
```

Listing 5.4: Refined mesh section in `create_subject_0.py`.

```
90  # create a roi 'midlayer_m1s1pmd' for 'mesh0_refinedM1'
91  rois['mesh0_refinedM1'] = {'midlayer_m1s1pmd': dict()}
92  rois['mesh0_refinedM1']['midlayer_m1s1pmd']['type'] = 'surface'
93  rois['mesh0_refinedM1']['midlayer_m1s1pmd']['info'] = 'freesurfer PMd,
    ↪  M1 and somatosensory cortex'
94  rois['mesh0_refinedM1']['midlayer_m1s1pmd']['hemisphere'] = 'lh'
95  rois['mesh0_refinedM1']['midlayer_m1s1pmd']['midlayer_surf_fname'] =
    ↪  f'fs_{subject_id}/surf/lh.central'
96  rois['mesh0_refinedM1']['midlayer_m1s1pmd']['fn_mask'] =
    ↪  f'roi/midlayer_m1s1pmd/mask_lefthandknob_M1S1PMd.mgh'
97  rois['mesh0_refinedM1']['midlayer_m1s1pmd']['fn_mask_avg'] =
    ↪  os.path.join(os.path.split(sub_dir)[0], 'roi',
    ↪  'lefthandknob_M1S1PMd.overlay')
```

Listing 5.5: ROI information for refined mesh in `create_subject_0.py`.

Update the subject-object file by executing `create_subject_0.py` and run the following script to create the refined mesh:

```
> python scripts/03_refine_mesh.py -s subject_0.hdf5 -m mesh0 -o
    mesh0_refinedM1


Parameters:
    -s : Path to subject-object file
    -m : Mesh ID (original)
    -o : Mesh ID (refined)
```

The refined mesh will be created in the folder `subject_0/mesh/mesh0_refinedM1`. See Figure 5.5 for a comparison of both head models. Bone and skin regions are not refined because their influence on the TMS-induced e-fields is weak (Saturnino, Madsen, & Thielscher, 2019). All following analyses are performed with the refined mesh.

TROUBLESHOOTING.

PROBLEM: Unreasonable mesh geometries.

REASON: E. g., wrong segmentation, cortical matter outside of the head, doubled or shifted brain segments might occur due to bad MRI quality or incorrect co-registration.
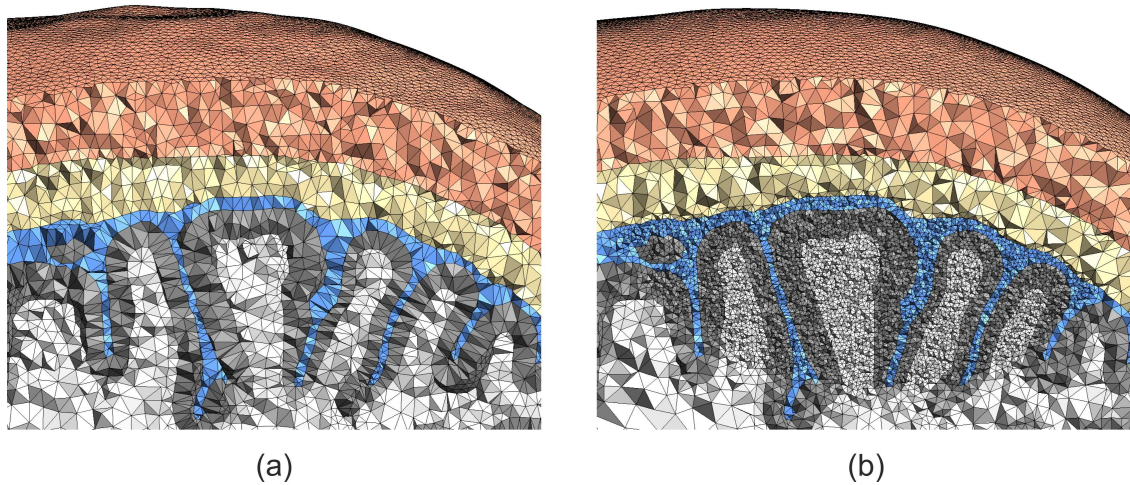
Figure 5.5: Original (a) and refined head mesh with smoothed skin surface (b) from the example data set. Figure published initially in Weise & Numssen et al. (2022).

SOLUTION: Check the quality of the MR images for low signal-to-noise or low intensity as well as a strong signal inhomogeneity. Manually set origins of the MRI coordinate systems for all images to a similar location, e.g., the center of the anterior commissure. If the segmentation was successful, but the mesh construction failed, restart the script with a slightly different vertex density.

PROBLEM: Invalid elements exist in the mesh.

REASON: Skin smoothing and meshing steps occasionally introduce invalid element definitions.

SOLUTION: Use the pynibs function `fix_mesh()` to eliminate invalid mesh elements.

5.3.2 Stage 2 – Data acquisition

TMS laboratory preparation

STEP 21. Start the initial motor threshold hunting procedure by running the `04_get_initial_m1_coords.py` script to transform template coordinates into subject space. The initial motor threshold hunting procedure must be started with a reasonable cortical target, for example, the MNI FDI coordinates from my previous work (FDI: -34.19, -14.33, 66.83; Numssen, Zier, et al., 2021).

```
> python scripts/04_get_initial_m1_coords.py -s subject_0.hdf5 -m
    mesh0_refinedM1


Parameters:
    -s : Path to subject-object file
    -m : Mesh ID
```

STEP 22. Enter these subject-specific coordinates (see Table 5.1 for the initial target coordinates for subject_0) as the target coordinates in the neuronavigation system to start the initial motor threshold hunting procedure with (step 7).

STEP 23. Initialize the neuronavigation session according to the neuronavigation manual and use the individualized coordinates from Step 22 as the initial target.
A modified T1 image is generated during head model construction with a coordinate system corresponding to the mesh. Use this image, subject_0/mesh/ mesh0_refinedM1/subject_0_T1_conform.nii.gz, for the neuronavigation system to minimize post-processing steps. Initialize the neuronavigation session according to the neuronavigation manual and use the individualized coordinates from subsubsection 5.3.2.1 as the initial target.

STEP 24. Configure the stimulation and EMG setup to stimulate once approximately every 5 seconds with a short jitter of at least 200 ms (Awiszus, 2003) and to record the EMG data in a time window of at least 200 ms starting at the TMS pulse, with at least 52 kHz sampling rate.
Recording valid MEPs relies on correct filtering parameters. These include gain (10 000) and filtering (highpass 30 Hz, low-pass 1 kHz). Different hardware setups might require different values or other parameters and should be checked carefully for artifacts before. The inter-stimulus interval (ISI) must not be shorter than 5 s to avoid facilitation or depression of the MEP amplitude (Julkunen et al., 2012; Brasil-Neto et al., 1994). See the example data (Numssen et al., 2022) set for an

Table 5.1: Target coordinates in subject and MNI space of subject_0.

Target	*Subject_0* space	MNI space
left-M1	[-37 -43 +48]	[-37 -25 62]

exemplary configuration file for the Signal software.

TMS electrode placement and EMG recording parameters

STEP 25. Ask the volunteer to take a comfortable position in the lab seat. Apply EMG surface electrodes in a standard belly-tendon montage for the muscle or muscles for which the rMT is to be determined (Figure 5.6).

STEP 26. Use the first *dorsal interosseous* (FDI) muscle of the right hand for right-handed volunteers for rMT estimation. Data from multiple muscles might be recorded during a single experiment or from the left hand for left-handed volunteers. If recording EMG data from multiple muscles simultaneously, note which channel records data from which muscle.

STEP 27. Place the active electrode over the muscle belly, the reference over the proximal tendon, and the ground electrode at the back of the wrist of the same hand (see Kleim et al. (2007) for detailed instructions). Both pre-gelled self-adhesive and passive EEG electrodes, have been used in our laboratories, yielding similar results. Skin preparation, i.e., fat removal and skin peeling, is advised. In addition, fixate all electrodes with strips of tape, as this has proven useful in keeping skin-electrode contact stable.

STEP 28. Ask the volunteer to place their arm and hand on a table, cushion, or similar to allow relaxation of all muscles. Perform an electrode impedance check and visually inspect the signal for an adequate low noise level ($\sim 10\,\mu V$) and correct muscle activity recognition.

TROUBLESHOOTING.

PROBLEM: High noise level in EMG signal.

REASON: Tension in the volunteer's hand or poor skin contact or electrical interference.

SOLUTION: Assure that the volunteer's hand is relaxed. Check skin contact of the electrodes. Replace the electrodes with new ones. Check the amplifier settings for correct parameters. Remove any electronic devices with high radiation power, such as mobile phones, from the proximity of measurement electronics.

Neuronavigation preparations

Preparation of the neuronavigation software might differ between manufacturers, but should include the following steps: 1) co-register the TMS coil, 2) co-register the volunteer to the anatomical scan, 3) record data.

STEP 29. Closely follow the manufacturer's manual for the co-registration of the volunteers to the anatomical scan. A precise co-registration of volunteers to their anatomical MR image is indispensable for a valid and precise functional localization. In addition to landmarks (e.g., nasion, tragi, lateral corners of the volunteer's eyes), experimenters should sample the volunteer's head surface evenly, if possible, including the forehead, posterior areas (inion), lateral areas, and superior areas. Assure a stable fixation of the tracking device attached to the volunteer's head during the experimental process and consider potential obstructions by the coil and its handle or cable while placing it.

STEP 30. Co-registering and re-validating the TMS coil during the experiment is important to avoid errors. Place the coil-tracker in a way to anticipate into account
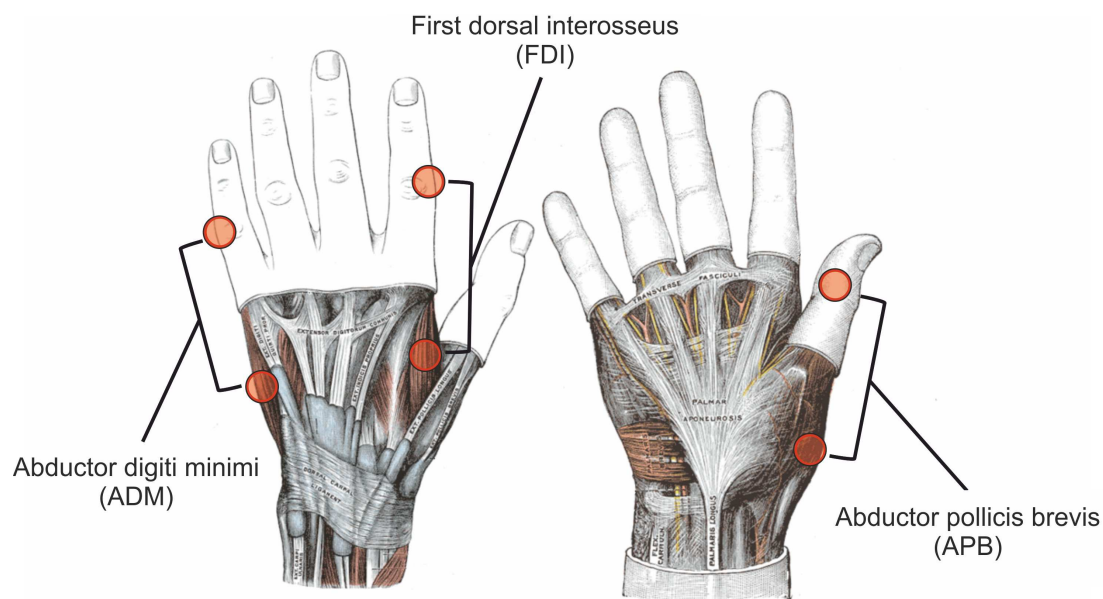
Figure 5.6: Electrode placement for EMG recordings using a bipolar belly-tendon montage. Modified plates #424 and #425, originally published in Gray (1918). Figure published initially in Weise & Numssen et al. (2022).

potential obstructions by the TMS coil and the experimenter. The coil has to be recognized from different angles, from 0° to 90°.

STEP 31. Record coil position/orientation, stimulation intensity, and MEP amplitudes for each pulse. Assure a working connection from the neuronavigation computer to the stimulator to record the realized stimulation intensity.

TROUBLESHOOTING.

PROBLEM: Neuronavigation does not record coil positions ('*TriggerMarker*').

REASON: Pulses might be dropped from the neuronavigation recording if the coil or head tracker is blocked from the camera.

SOLUTION: Occasionally, pulses might be dropped from the neuronavigation recording. This is automatically taken care of by the post-processing scripts. Check the hardware connections (stimulator → triggerbox → TMS Navigator PC) if no pules at all are recorded. If multiple EMG `.mat` files are saved instead of one, these can be entered as a list for the `exp['m1']['fn_data']` parameter (see below).

PROBLEM: Neuronavigation does not record stimulation intensities.

REASON: Faulty hardware connection or software error.

SOLUTION: Stimulation intensities are transmitted via the serial cable (Stimulator control port → TMS Navigator PC). Check hardware connection and settings on the stimulator. Restart Neuronavigation (subject registration can be restored).

Initial motor hotspot estimation

STEP 32. Estimate the resting motor threshold (rMT) and the corresponding hotspot with a standard threshold hunting procedure (see IFCN guidelines (Rossini et al., 2015) for an overview), starting at the individualized coordinates from step 6. Here, a rough rMT estimation is sufficient (see below).

STEP 33. Save the hotspot position by adding an InstrumentMarker for the identified coil position (step 32) in the Localite neuronavigation software using the InstrumentMarker control panel. This InstrumentMarker will be used below as visual guidance to sample a reasonable area.

Determining the stimulation intensity for the mapping procedure

The following procedure ensures a complete sampling of the cortical I/O curve, i.e., the relation between the local cortical e-field and the MEP amplitude, of the to-be-located neural population with all its features (step 11). In the realm of motor cortex stimulation, I expect a sigmoidal relationship, which can be parameterized via a lower plateau, turning point, and saturation point.

STEP 34. Start stimulating over the previously determined hotspot with rMT intensity and increase the intensity until MEP amplitudes reach the upper plateau of the sigmoidal I/O curve. As a guideline, the upper plateau of the sigmoidal I/O should be around 150 % of the rMT. The realized amplitudes differ between individuals and EMG setup but should be around 2 mv to 4 mV for FDI (lower for smaller muscles like ADM).

STEP 35. Move the coil about 3 cm into the inferior, posterior, superior, and anterior directions and rotate the coil about $\pm 30°$ while observing the resulting MEPs.

STEP 36. The MEPs should decrease to low amplitudes or to zero when tilting the coil 30° and moving it far away from the initial hotspot. Increase the stimulator intensity if the MEPs vanish already before reaching the maximum coil deviations. If MEPs at the outer border of the search area are too high, decrease the stimulator intensity until they are in the expected range. Stop increasing the intensity if the stimulation becomes uncomfortable for the volunteer.

STEP 37. If EMG data from multiple muscles are recorded, select an intensity yielding an appropriate MEP response for all muscles. Keep these stimulator intensities for later use. The random placement and orientation of the TMS coil over the target region entails a random sampling of the I/O curve and thus limits the hysteresis effect (Möller et al., 2009; Schmidt et al., 2009). If the stimulation intensity is too low, the upper saturation of the MEP amplitude is not sampled. This undersampling negatively affects the localization due to undersampling of the cortical I/O curves. In this case, more stimulations are required to yield stable results.

Applying TMS with quasi-random coil positions and orientations

During the following steps, MEPs will be recorded for quasi-random coil positions and orientations to sample data from a wide range of parameter combinations.

POSITION OF VOLUNTEER. During TMS mapping, the volunteer sits comfortably with the right arm resting at half abdominal height on a pillow. The volunteer must wear earplugs and completely relax arm and hand muscles. The wrist is in a neutral position, and the fingers are in a resting position with slight flexion. Use the EMG signal to confirm complete relaxation. Remind the volunteer to avoid arm, hand, and finger muscle contractions throughout the TMS procedure. Small movements and adjustments are only allowed between stimulations.

POSITION OF EXPERIMENTERS. The experimenter controlling the TMS coil (Figure 5.7 a) stands sideways behind the volunteer, such that both, the neuronavigation and the EMG signal, can be monitored. The second experimenter (Figure 5.7b) starts, pauses, and stops the experiment and controls data recording.

STEP 38. Coil positions (referring to the center of the coil) are chosen within an area of approximately $3\,\mathrm{cm}$ radius around the manually estimated M1 hotspot (Figure 5.8). Start recording the coil position/orientation and the EMG signal. Ensure that the coil gently touches the scalp of the volunteer. In later modeling steps, direct contact between the plastic housing of the coil and the skin surface is assumed (see step 14).

STEP 39. Set the stimulator to the intensity determined in step 10 and apply stimulations with an ISI of $5\,\mathrm{s} \pm 200\,\mathrm{ms}$ jitter. Choose an ISI that does not cause progressive carry-over effects (i.e., at least $5\,\mathrm{s}$ for single pulse motor cortex studies; Julkunen et al., 2012; Brasil-Neto et al., 1994).

STEP 40. Between stimulations, move the coil arbitrarily within the area and vary the coil angle in the interval $\pm90°$ around the PA-45 orientation towards the *fissura longitudinalis* (Brasil-Neto et al., 1992; Mills et al., 1992).

STEP 41. Apply at least 300 stimulations to ensure successful localization of the cortical muscle representation. Short breaks during the measurement process are possible, and in this case, the EMG recording software should be paused (and not stopped) to prevent creation of multiple EMG data files. After completing the stimulation protocol, export the EMG data for all channels and all frames to a `.mat`
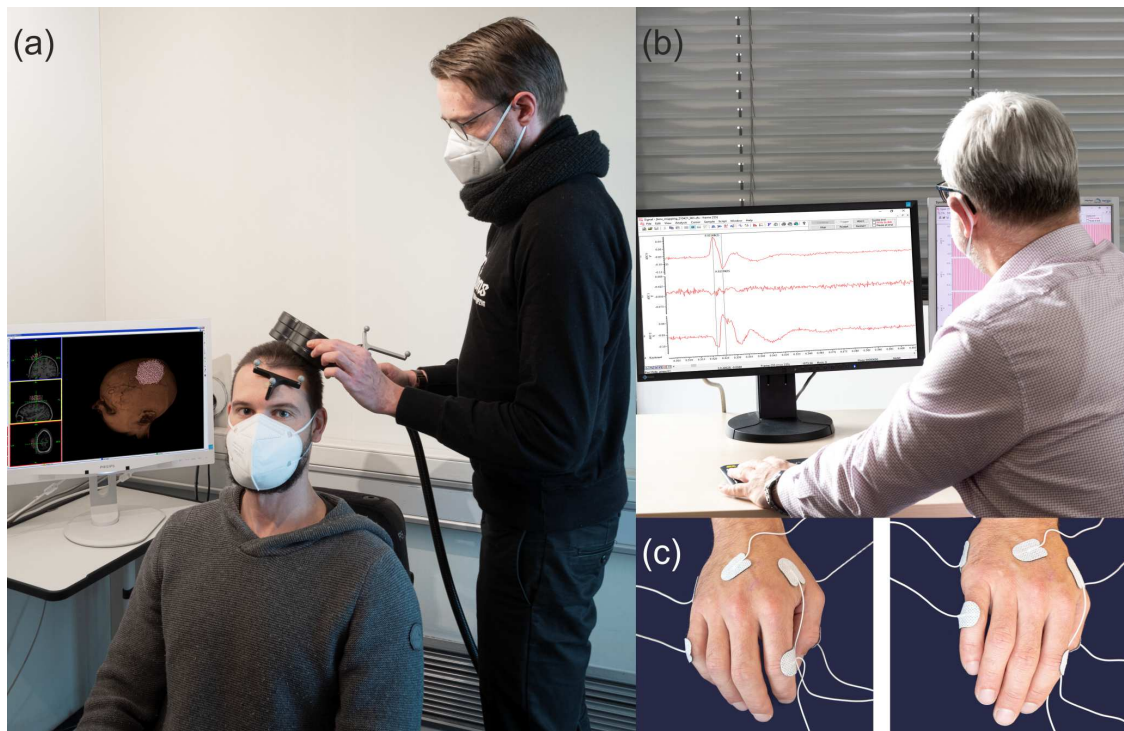
Figure 5.7: Position of volunteer and experimenters. (a) One experimenter positions the TMS coil over the volunteer's motor cortex and (b) a second experimenter controls the stimulator and monitors the motor evoked potentials (MEPs). (c) The belly tendon montage to measure MEPs from the little, index, and thumb finger muscles (ADM, FDI, APB). Figure published initially in Weise & Numssen et al. (2022).

file via the 'Export as' Signal function.

TROUBLESHOOTING.

PROBLEM: The Participant experiences discomfort from the stimulation.

SOLUTION: If the volunteer reports discomfort during the protocol, decrease the stimulation intensity. More pulses will be needed if the intensity is too low (see above). Intensity changes are recorded by the TMS Navigator and will be considered automatically during the post-processing.

PROBLEM: MEP recording software was stopped (instead of paused) during the experiment.

Reason: User error.

Solution: If multiple EMG `.mat` files are saved instead of one, these can be entered as a list for the `exp['m1']['fn_data']` parameter.
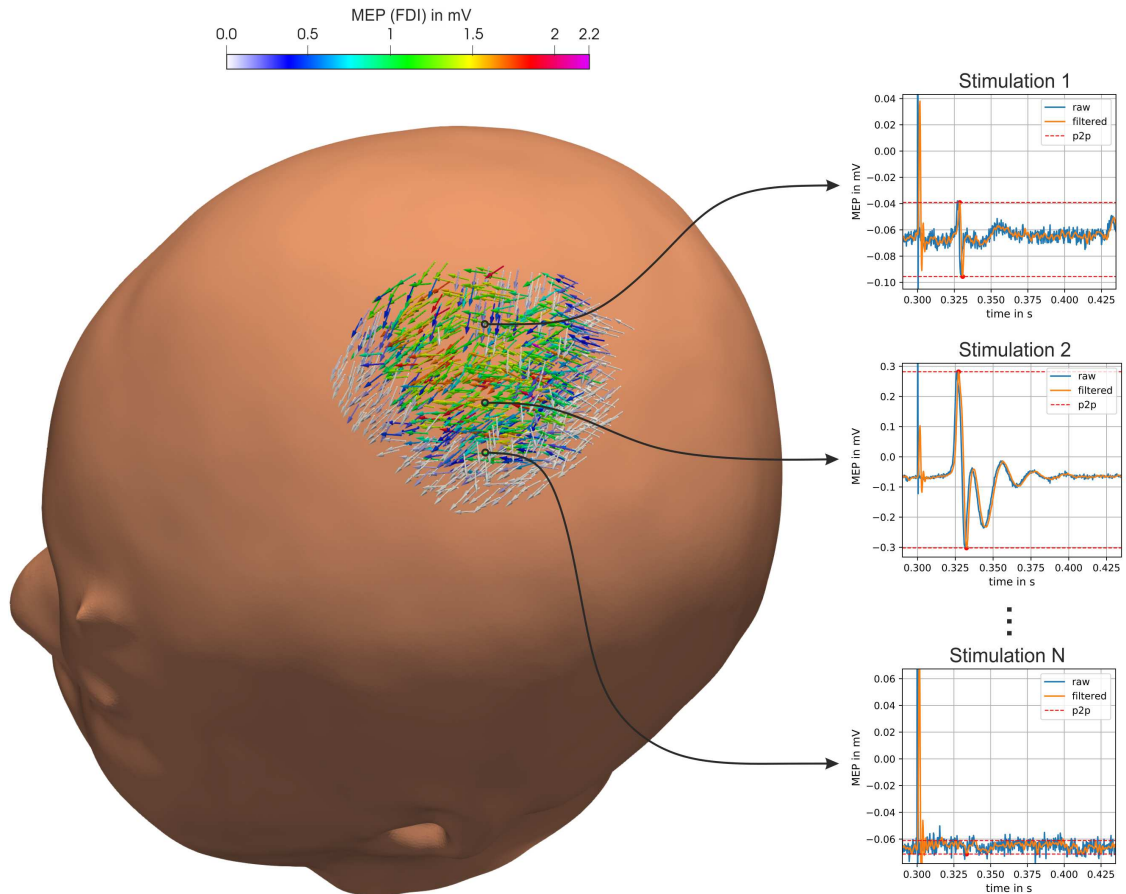
Figure 5.8: Realized quasi-random TMS pulses over the motor cortex.
MEPs are recorded for every TMS pulse at a quasi-random position and orientation. Right: MEPs for three exemplary pulses. Color: amplitude for FDI MEPs. Figure published initially in Weise & Numssen et al. (2022).

5.3.3 Stage 3 – Post-processing

Post-processing of experimental data

Step 42. Copy the EMG `.mat` file to the subject data folder `subject_0/exp/m1/mep`.

STEP 43. Copy the latest trigger marker `TriggerMarker\%DATETIME\%`
`.xml` file from the neuronavigation folder `Sessions/Session_\%DATE\%/`
`TMSTrigger` and the neuronavigation T1 image from `BinData/NIFTI` to the
subject data folder `subject_0/exp/m1/tms_navigator`.

STEP 44. Add paths and filenames of the triggermarker file (`fn_tms_nav`), the T1
image (`fn_mri_nii`), and the EMG data (`fn_data`) to the `create_subject_0`
`.py` script (Listing 5.6).

STEP 45. Enter the muscle names in the correct EMG channel order in `channels`.
If necessary, adjust the `tms_pulse_time` parameter to indicate the TMS pulse
onset in seconds. Save and execute the `create_subject_0.py` script to update
the subject-object file.

```
99  # experiment information
100 experiments = dict()
101
102 # create 'm1' experiment with some basic information
103 experiments['m1'] = dict()
104 experiments['m1']['info'] = ['TMS-MEP M1 Regression study (random
    ↪  sampling), ISI=5']
105 experiments['m1']['date'] = ['09/11/2020']
106 experiments['m1']['nnav_system'] = 'Localite'
107 experiments['m1']['experimenter'] = 'Ole Numssen, Konstantin Weise'
108
109 # neuronavigation data
110 experiments['m1']['fn_tms_nav'] = [[sub_dir +
    ↪  '/exp/m1/tms_navigator/TriggerMarkers.xml', '']]
111 # stimulation intensity in additional .csv file:
112 experiments['m1']['fn_intensity'] = None
113 experiments['m1']['fn_coil'] =
    ↪  [[os.path.join(os.path.split(sub_dir)[0], 'coils',
    ↪  'MagVenture_MCF_B65_REF_highres.ccd.nii.gz')]]
114
115 # EMG/MEP data
116 experiments['m1']['fn_data'] = [[f'{sub_dir}/exp/m1/mep/mep.cfs']]
117 # EEG channel names (order is important!):
118 experiments['m1']['channels'] = ['FDI', 'ADM', 'APB']
119 # TMS pulse onset in [s]
120 experiments['m1']['tms_pulse_time'] = 0.3
121
122 # T1 image the co-registration was performed with
```

```
123  experiments['m1']['fn_mri_nii'] =
     ↪  [[f'{sub_dir}/exp/m1/tms_navigator/subject_0_T1fs_conform.nii']]

124

125  # output filename with the merged experimental data
126  experiments['m1']['fn_exp_hdf5'] =
     ↪  [f'{sub_dir}/exp/m1/experiment.hdf5']
```

Listing 5.6: Experiment information in create_subject_0.py.

STEP 46. Merge and postprocess TMS navigator and EMG data:

```
> python scripts/05_merge_exp_data.py -s subject_0.hdf5 -m mesh0_refinedM1 -e m1 -


Parameters:
    -s : Path to subject-object file
    -m : Mesh ID
    -e : Experiment ID
    -d : Apply coil/skin distance correction
    -r : Remove outlier
    -p : Save MEP plots
```

This matches the EMG data to the recorded coil positions of the neuronavigation system and saves the results in a file specified in exp['m1']['fn_exp_hdf5']. EMG data is filtered using a 6th-order Butterworth low-pass filter with a cutoff frequency of 500 Hz. Subsequently, peak-to-peak amplitudes are extracted by a min-max search from 18 ms to 35 ms after the TMS pulse (Figure 5.9 Sommer et al., 2006).

STEP 47. Coordinates recorded in the TriggerMarker\%DATETIME\%.xml file are converted to the SimNIBS coordinate system to compute the e-field distributions of the realized coil positions and orientations. For other neuronavigation systems, different coordinate system transformations will be necessary. Coil positions are projected onto the skin surface to compensate for slight deviations (0.5 mm to 2 mm) stemming from the tracking system and the head surface reconstruction of the neuronavigation software. Coil positions with a distance greater than 2 mm from the head surface are excluded from the analysis.
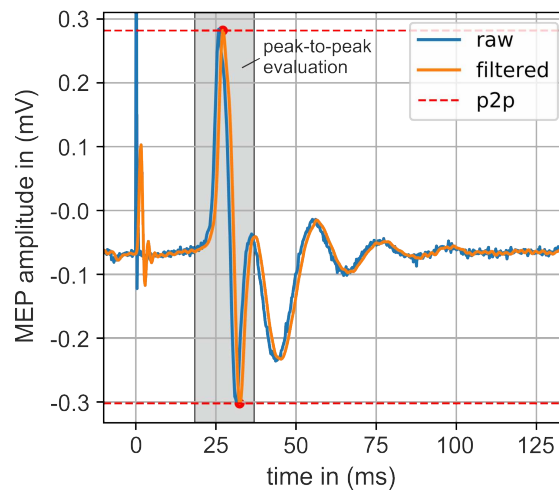
Figure 5.9: Postprocessed EMG data and extracted peak-to-peak amplitudes of motor evoked potentials. Figure published initially in Weise & Numssen et al. (2022).

E-field calculations

STEP 48. Calculate the e-field distributions for the recorded coil positions with the script below. A configuration file (`subject_0/results/electric_field/FEM_config.mat`) is created, including parameters to initialize the SimNIBS FEM solver. The transformed coil positions from `subject_0/exp/m1/matsimnibs.hdf5` are imported, and e-fields are computed. Fields in the midlayer ROI (subsubsection 5.3.1.2) are calculated, scaled with the applied stimulator intensity, and stored (`subject_0/results/electric_field/e_scaled.hdf5`). The standard FEM solver requires about 10 GB to 12 GB of RAM for each parallel computation (8 GB without mesh refinement). Depending on the available computational resources, the process can be accelerated using the solver option `'PARDISO'`, which requires about 40 GB for each core for the given mesh size.

```
> python scripts/06_calc_e.py -s subject_0.hdf5 -m mesh0_refinedM1 -e
    m1 -r midlayer_m1s1pmd -n 4 -a vn -p

Parameters:
    -s : Path to subject-object file
    -m : Mesh ID
    -e : Experiment ID
    -r : ROI ID
    -n : Number of parallel computations
    -a : Anisotropic conductivity (volume normalized): "vn", isotropic
        conductivity: "scalar"
    -p : Flag to use pardiso solver
```

Troubleshooting.

Problem : SimNIBS does not return the final output after successful e-field simulations.

Reason : A long computation time and/or high RAM usage can trigger multiprocessing issues that prevent SimNIBS from successfully returning.

Solution : Cancel and re-run `06_calc_e.py` script with the same arguments.

5.3.4 Stage 4 – Cortical localization

Localizing the cortical muscle representation

After calculating the e-field distributions and the MEP amplitudes for all stimulations, the data is fitted to cortical I/O curves with linear, sigmoidal, or log-transformed sigmoidal functions for all examined muscles.

Linear regression has the lowest computational cost but reduced resolution and biological plausibility (see chapter 4 for a comparison between different curve-fitting approaches). Sigmoidal or log-transformed sigmoidal functions are recommended.

Step 49. In every element in the ROI, the goodness-of-fit is calculated using R^2 scores, with a higher score representing a better fit between data and the assumed activation function. Results are saved in `subject_0/results/.../r2_roi_data.hdf5`, together with a file containing the geometry information of the

ROI and an `.xdmf` markup file to visualize the results, for example, with ParaView. The curve-fitting and goodness-of-fit quantification is implemented in the following script.

```
> python scripts/07_calc_r2.py -s subject_0.hdf5 -m mesh0_refinedM1 -e
    m1 -r midlayer_m1s1pmd -n 10 -f sigmoid4_log -i 10 -v

Parameters:
    -s : Path to subject-object file
    -m : Mesh ID
    -e : Experiment ID
    -r : ROI ID
    -n : Number of parallel computations
    -f : Fit function ("linear", "sigmoid4", "sigmoid4_log")
    -i : Number of refit iterations
    -v : verbose, show output messages
```

STEP 50. Identify the cortical origin of the MEPs based on the goodness-of-fit results in the results `.hdf5` file. Assess the overall quality of the result. After the R^2 computation for all stimulations (e.g., $N = 150$ pulses), this solution is compared to the R^2 map for $n - 1$ pulses (e.g., $150 - 1 = 149$ pulses) via two metrics: The normalized root-mean-square deviation (NRMSD) assesses the similarity of the whole cortical R^2 map, whereas the geodesic distance measures the distance along the cortical surface between the identified peak R^2 locations. NRMSD above 5 % and peak R^2 distances above 3 mm imply data collected data did not cover enough of the variance (cf. chapter 4).

TROUBLESHOOTING.

PROBLEM : Localization results do not converge.

REASON : The collected dataset does not cover enough variance to precisely map the cortical representation.

SOLUTION : This could be the case for mappings outside of the primary motor cortex or because only the coil position and not its orientation was varied. Repeat the experiment (step 11) and combine the data from both experiments (step 13). Finally, rerun step 14 to calculate the R^2 map.
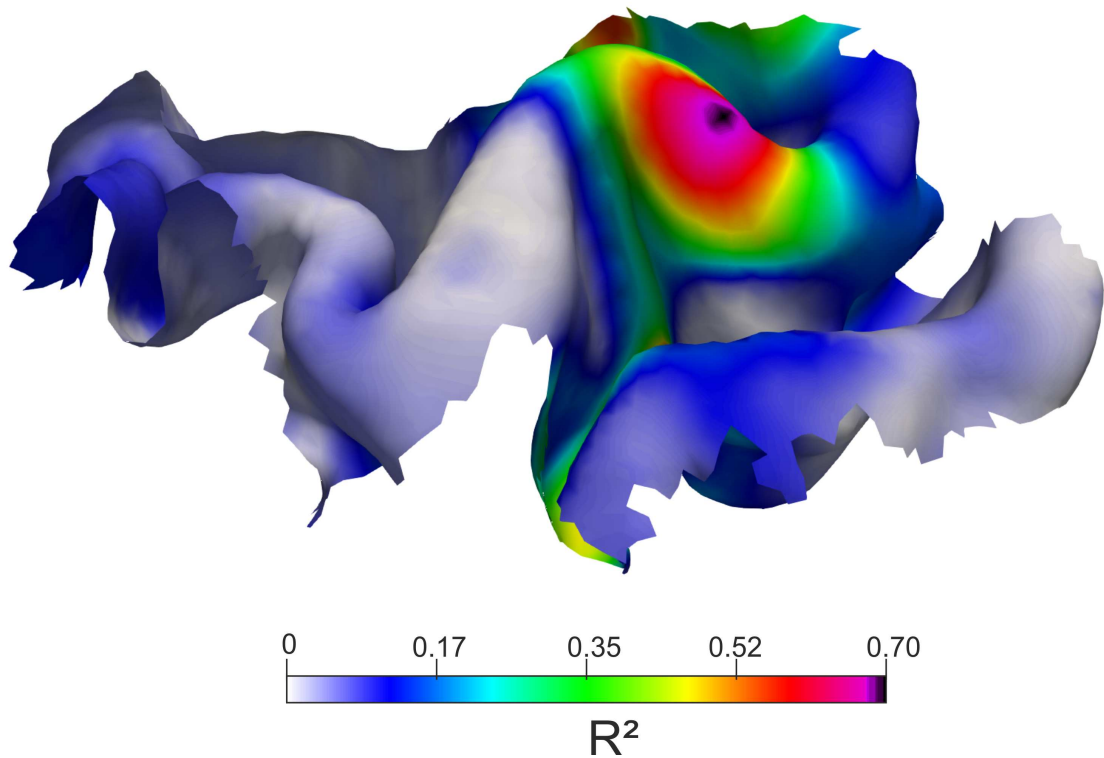
Figure 5.10: The goodness-of-fit distribution identifies the cortical MEP origin. The relationship between the induced e-field distributions and the MEPs from quasi-random coil positions were fitted to log-sigmoidal functions. At each location, the goodness-of-fit is quantified by the R^2 score between fit and data. Figure published initially in Weise & Numssen et al. (2022).

The optimal coil position for motor threshold determination

After identifying the cortical target, a coil position/orientation can be computed to stimulate this area optimally.

STEP 51. Run the script `08_calc_opt_coil_pos.py` to choose the cortical location with maximum goodness-of-fit value as the cortical target for the coil optimization from the results file of step 14 (`subject_0/results/.../FDI/.../r2_roi_data.hdf5`).

STEP 52. E-fields are computed for several candidate coil positions and orientations for this cortical target (Figure 5.11a). A Localite *instrument marker* to be used in the subsequent MT determination experiment is exported for the coil position/orientation that maximizes the e-field magnitude at the cortical target. A different TMS coil

type from the one used in the first TMS experiment can be used here as long as the correct coil model is specified during the optimal position/orientation calculation. E-field results for the optimum coil position/orientation (Figure 5.11b) are stored in the .hdf5/.xdmf file tuple subject_0/opt/.../opt_coil_pos.hdf5, the instrument marker as subject_0/opt/.../opt_coil_pos.xml.

```
> python scripts/08_calc_opt_coil_pos.py -s subject_0.hdf5 -m
    mesh0_refinedM1 -e m1 -n 4 -a vn -p -t subject0/results/.../FDI
    /.../r2_roi_data.hdf5 -c example_data/coils/
    MagVenture_MCF_B65_REF_highres.ccd.nii.gz

Parameters:
    -s : Path to subject-object file
    -m : Mesh ID
    -e : Experiment ID
    -n : Number of parallel computations
    -a : Anisotropic conductivity: "vn", isotropic conductivity: "
        scalar"
    -p : Flag to use pardiso solver
    -t : Cortical target (x y z coordinate or r2 result file)
    -q : \Acrshort{ef} quantity to optimize ("E_mag" (default), "E_norm
        ", "E_tan")
    -c : Coil .nii.gz file
```

STEP 53. In addition, the individual cortical e-field threshold in V/m and a motor threshold estimation in %MSO can be computed from the available data after identifying the optimum coil position (09_estimate_rmt_from_data.py). This step combines the localization of the cortical origins of the MEPs (step 14), the exact rMT activating these neuronal populations (step 17), and the e-field distribution of the optimal stimulation position/orientation (step 15).

```
> python scripts/09_estimate_rmt_from_data.py --fn_gof=/path/to/
    subject0/results/\dots/FDI/\dots/r2_roi_data.hdf5 --fn_e=/path/to/
    subject_0/results/exp_m1/electric_field/mesh_mesh0_refinedM1/
    roi_midlayer_m1s1pmd/e_scaled.hdf5 --fn_exp=/path/to/subject_0/exp/
    m1/experiment.hdf5 --fn_e_opt=/path/to/subject_0/opt/exp_m1/target_
    [-26.56 -38.13 +57.77]/mesh_mesh0_refinedM1/E_mag/e_opt/e.hdf5 --
```

```
    muscle=FDI --fun_type=sigmoid4_log --MSO_factor=1.43 --rmt_thres=50
     --n_cpu=1


Parameters:
    --fn_gof : Path to goodness-of-fit results .hdf5 file (ROI)
    --fn_e : Path to e_scaled.hdf5 file (ROI)
    --fn_exp : Path to experiment.hdf5 file
    --fn_e_opt : Path to optimal \acs{ef} .hdf5
    --muscle : Muscle name
    --fun_type : Function to fit data. One of ("sigmoid", "sigmoid4_log
       ", "linear")
    --MSO_factor : Vendor specific factor to transform $A/\mus$ to \%
       MSO
    --rmt_thres : rMT threshold in $\mu$ V
    --n_cpu : Number of CPUs to use
```

The e-field intensity in the hotspot (in V/m) for a stimulator intensity of 1 A/µs is saved in the file opt/.../opt_coil_pos_m1.hdf5. Multiplication with the vendor- and coil-specific current/intensity factor and the rMT yields the e-field strength needed to stimulate the neural population effectively. For a MagVenture X100 stimulator and a MagVenture MCF-B65 coil, the factor is 1.43 A/µs/%MSO. Instead of assessing the real rMT precisely with a final experimental session (step 17) this computed rMT approximation can be used if ±3 %MSO accuracy suffices.

5.3.5 Stage 5 – Determining the individual e-field threshold

Session preparation

STEP 54. Create a copy of the first TMS session with the TMS Navigator software. Repeat Step 7 – Step 9 to prepare the volunteer. Use the TMS coil considered during calculating the optimal coil position for the rMT determination (subsubsection 5.3.4.2). Duration: 20 min

Determining the exact resting motor threshold

STEP 55. Load the InstrumentMarker file opt/.../opt_coil_pos_m1.xml containing the optimal coil position and orientation with the IMporter tool.
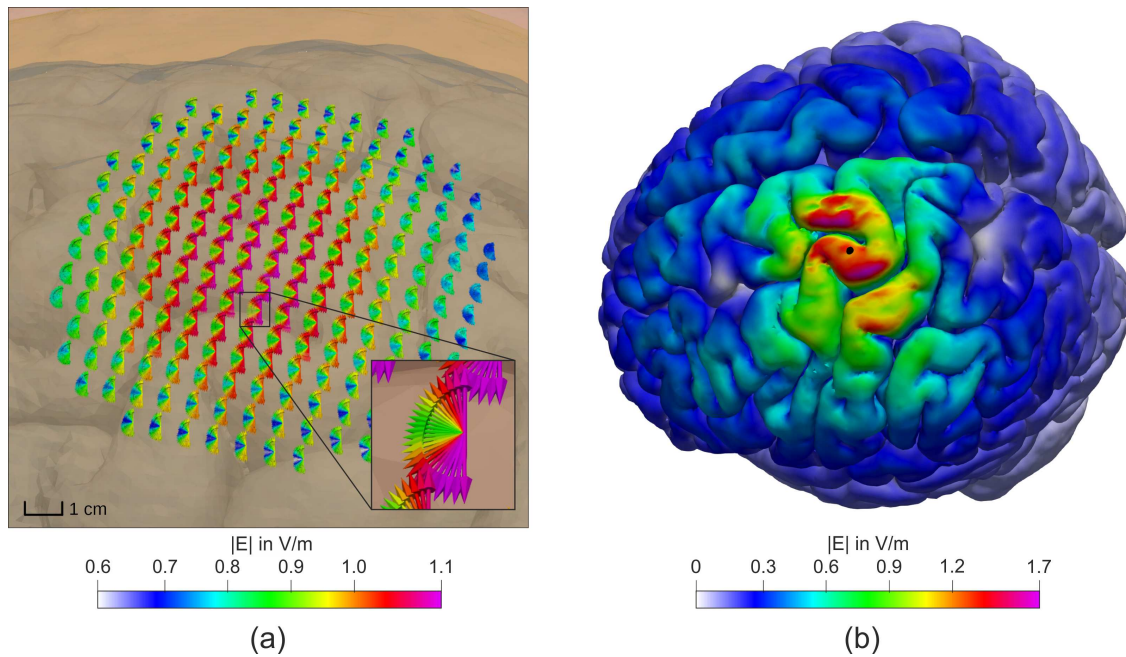
Figure 5.11: The optimal coil position for rMT determination is identified.
(a) 4825 candidate coil positions and orientations. Color: e-field magnitude in the cortical target (here: FDI); (b) E-field magnitude on the GM surface from the optimal coil position. The black spot is the cortical target (R^2 hotspot from Figure 5.10) determined by the previous localization. Areas more superficial than the cortical target receive a stronger e-field exposure. Figure published initially in Weise & Numssen et al. (2022).

STEP 56. Determine the rMT (Rossini et al., 2015) for the muscle of interest (e.g., FDI) with this coil position/orientation. The rMT should be lowest for the optimized coil position/orientation compared to locations around the optimum.

5.4 Timing

See Table 5.2 for the estimated durations of each step.

5.5 Anticipated results

A successful localization and fitting procedure yields high R^2 values (Figure 5.10: $R^2_{\max}$) and a smooth distribution of fits across the region of interest. When mapping

Table 5.2: Estimated durations of all steps to complete the protocol.

Step	Description	Time
	Stage 1: Head model construction: ~14 h	
1	Volunteer clearance	30 min
2–4	MRI acquisition	1 h
5–9	Creating the subject-object	15 min
10–12	Defining the region of interest	10 min
13–20	Constructing the head model	~12 h
	Stage 2: Data acquisition: ~1 h	
21–24	TMS laboratory preparation	10 min
25–28	Electrode placement and EMG recording parameters	10 min
29–31	Neuronavigation preparation	10 min
32–33	Initial motor hotspot estimation	15 min
34–37	Determination stimulation intensity for localization	10 min
38–41	Applying TMS with quasi-random coil positions	20 min
	Stage 3: Post-processing: ~12 h to 24 h	
42–47	Post-processing of experimental data	10 min
48	E-field calculations	4 h to 12 h
	Stage 4: Cortical localization 6 to 24 h	
49–50	Localizing the cortical muscle representation	3 min
51–53	The optimal coil position for motor threshold determination	6 h to 24 h
	Stage 5: Determining the individual e-field threshold: 30 min	
54	Session preparation	25 min
55–56	Determining the exact resting motor threshold	5 min

multiple muscles concurrently, each muscle yields a single R^2 map with distinct peaks. The cortical localization is reflected by a goodness-of-fit distribution that peaks in a unique focal hotspot in the motor hand area of the precentral gyrus, as shown in Figure 5.10. However, if the number of stimulation sites is too low, second hotspots may emerge in the somatosensory or premotor cortex, as observed in previous studies (Bungert et al., 2016; Weise & Numssen et al., 2020). These spurious hotspots result from array ambiguities, for instance, spurious overlaps of the realized e-fields or an insufficient sampling of the cortical I/O curve.

In healthy volunteers, the resting motor threshold for FDI usually equals approximately 35 %MSO to 45 %MSO. However, this depends strongly on the individual brain anatomy and potentially on other factors. MEP amplitudes are generally in the range of 0.84 mV ± 0.63 mV at 120 %, 1.82 mV ±1.29 mV at 135 %, and 2.29 mV ± 1.67 mV at 150 % of the rMT (Pellegrini et al., 2018).

5.6 Summary

The approach described herein pinpoints the cortical origin of MEPs (Figure 5.9) for single or multiple muscles concurrently via TMS by assessing the functional relation between the induced e-field and the elicited MEP.

The data acquisition includes TMS pulses around the primary motor cortex with random coil positions and orientations (Figure 5.8). This procedure yields MEPs with high (Figure 5.8), middle MEP), low (Figure 5.8, top MEP), and no MEPs (Figure 5.8, bottom MEP) due to the different strengths of cortical stimulation at the muscle representation. For each element in a region of interest, the relationship between cortical e-field exposure and MEP is quantified via the R^2 score (Figure 5.10). The peak R^2 location is assumed to be the origin of the cortical muscle representation (Figure 5.10, black spot on gyral crown).

Rigorous testing of the convergence properties of the approach revealed a lower bound of 200 to 300 quasi-random stimulation sites (Figure 5.8) to robustly determine the first *dorsal interosseous* (FDI) representation. Notably, the mapping approach is based on quasi-random coil positions and an automatized, objective analysis scheme and, thus, is user-independent. In addition, a precise cortical localization renders TMS dosing based on an individual cortical activation threshold (step 53), possible. A cortical e-field-based dosing metric, in contrast to a commonly used MT-based metric (in %MSO, cf. subsubsection 2.3.1.1), would provide a biophysiogically plausible dosing strategy.

Chapter 6
Discussion and outlook

6.1 Discussion

6.1.1 Overview

Above, I have reasoned for a novel TMS mapping approach that leverages information from the full relationship between induced e-fields from TMS and the modulated behavior (section 1.1). As such, this approach resides on a fundamentally different understanding and analysis of TMS (section 1.1, compared to how it is currently employed. In contrast to a *binary* understanding of TMS – for example, *active* versus *sham* TMS– I propose the appreciation of TMS as a continuous factor, both within and across subjects: Within subjects, TMS exposes different cortical regions to different local e-field parts. Across subjects, TMS yields different stimulation exposures with current dosing approaches, which are based on the motor threshold (MT), both, at the cortical target and off-target locations. Together, these sources of unexplained variance reduce TMS effect sizes and impede a straightforward and clear-cut interpretation of TMS studies.

I have presented two implementations of novel single-subject TMS cortical mapping approaches to overcome this shortcoming. I applied both in a set of volunteers to pinpoint cortical representations of finger muscles in the primary motor cortex (M1): i) A first approximation (chapter 3), which derived its cortical mapping metric from previous knowledge of physiological input-output relationships (I/O curves) of induced e-fields and evoked muscle responses (MEPs). The precision of this mapping approach was underpinned by an experimental validation study in which the correct cortical localization of muscle representations was proven. ii) Building on this, I significantly improved the efficiency of the mapping approach without hampering its precision. The resulting methodological solution and the experimental paradigm are presented in chapter 4. Again, the precision of the method was proven with extensive experimental validation. Notably, this second implementation leverages

---

Chapter image: 3D-scan of an 1850's phrenology bust from Anatomical Museum (2018). TMS coil model: MagVenture MCF-B65. Grey matter brain surface with induced electric field strength ($|E|$) computed with SimNIBS.

the variance between induced e-fields from TMS pulses from quasi-random positions and orientations – ultimately leading to a significantly reduced number of necessary stimulations and a simple and fast experimental realization.

6.1.2 Insights into neural activation by TMS

My main finding regarding the interaction between TMS and neural structures is that relatively focal neural structures in the gyral crowns, extending to the upper parts of the sulcal wall of the motor hand area, are the origins of the motor evoked potentials (MEPs). Both presented cortical mapping implementations identified the e-field's magnitude ($|E|$) and the e-field's tangential component $E_\parallel$ to drive the MEPs, in contrast to the e-field's normal component $E_\perp$. Importantly, this parallels recent modeling work of detailed single neurons from Aberra et al. (2020) and substantiates their results through the integration of experimental data.

The identified geodesic distances between finger muscle representations are consistent with recent high-resolution functional MRI studies (Yu et al., 2008). Moreover, the somatotopic organization of finger muscle representations in M1 is in accordance with previous work, i.e., APB located infero-lateral to ADM (Wilson et al., 1993; Martuzzi et al., 2014) and ADM located superior to FDI (Dubbioso et al., 2021; Raffin et al., 2015; Raffin & Siebner, 2019; Dubbioso et al., 2017). The observed substantial variability between subjects is also consistent with previous studies (Goldsworthy et al., 2016). Based on these collected results, I reason that TMS either evokes muscle activity through direct cortico-motoneuronal pyramidal neurons from the (caudal PMd; PMdc; Dum & Strick, 2004) or indirectly via cortico-cortical premotor-motor (PMdc-to-BA4a/BA4p) projections (Ninomiya et al., 2019; Siebner et al., 2022).

6.1.3 Comparison with other mapping methods

Currently, grid-based CoG approaches represent the gold standard (see subsection 2.3.3 and Sondergaard et al., 2021) for non-invasive human motor cortex mappings. These mapping approaches are characterized by considerable variation, both in experimental realization and in the obtained results (Sondergaard et al., 2021), and often significantly exceed the number of 150 pulses, which are required for the here presented approach (chapter 4; Numssen, Zier, et al., 2021). Significant

differences in the experimental realization, including fundamental parameters like grid size and resolution, introduce significant variance across CoG-derived mapping results. Notably, grid-based approaches aim to locate MEP origins on the cortex as a function of coil position on the head surface rather than utilizing the underlying functional relationship between the induced e-field in the cortex and the evoked response. These approaches thus neglect the largest part of the response curve, oversimplify the underlying causal relationship, and impede accurate conclusions about the actual site of cortical stimulation.

Only recently, TMS localization has been considerably improved by specifically including the e-fields to explain the TMS-induced effect (Opitz et al., 2014; Mandija et al., 2016; Magsood & Hadimani, 2021). Here, multiple e-fields are considered additive or multiplicative (Aonuma et al., 2018; Opitz et al., 2013), yielding a bias towards identifying superficial cortical regions due to the spatial gradient of the e-field. Several statistical approaches were introduced to overcome this bias, which quantified the effects of e-fields from either multiple coil orientations (Bungert et al., 2016) or positions (Laakso et al., 2018) on the rMT.

These first implementations relied on the TMS-induced cortical e-fields to locate a functional representation, demonstrating the principal practicability of such an approach. However, only stimulation responses from either different positions or orientations could be analytically combined. Additionally, the analyses did only compare data from only a few coil configurations (Laakso et al. (2018): 5 positions, Bungert et al. (2016): 9 angles) to quantify a single point on the I/O curve, i.e., the MT.

In contrast, the here proposed method exploits information from many different coil positions and orientations to increase e-field variability across stimulation conditions. This integration of many stimulation sites leads to high localization reliability, a low number of stimulations, and a simple experimental setup.

6.1.4 Applications of the method

The ability to precisely map individual motor cortices fast and reliably adds value, both for neuroscientific and clinical environments alike. Currently, motor mappings in patients with brain tumors (Rösler et al., 2014; Shamov et al., 2010) or

epilepsy (Pelletier et al., 2007) are performed intraoperatively with strenuous direct cortical stimulation (see subsection 2.3.4). With its precise results, the presented mapping approach can support operational planning with precise, pre-operative cortical results. Its straightforward experimental implementation building on quasi-random stimulation sites further allows assessing the stability of the cortical organization versus motor plasticity (Nazarova et al., 2021), due to its robustness (cf. section 4.5). The precise identification of cortical muscle representations not only provides valuable insights into the functional organization of the human cortex but can also contribute to a physiologically founded TMS dosing metric: A subject-specific cortical e-field threshold may significantly advance personalized stimulation approaches (Zmeykina et al., 2020). This e-field-based TMS dosing approach is addressed in the outlook section below.

In addition, this novel mapping approach, linking induced e-fields to an outcome variable, does not — in principle — rely on a direct evocation of measurable outcomes like MEPs. Instead, modulating an experimental outcome variable, such as response speed or accuracy of a behavioral response (Rushworth et al., 2001), would suffice as long as a trial-by-trial assessment is possible. Furthermore, outcome variables based on other modalities, for example, EEG, could provide more direct cortical readouts (Rosanova et al., 2009). Finally, the mapping approach might be adapted to map higher functional domains as long as i) stimulation of a focal brain region results in a reliable change of a measurable outcome variable and ii) a functional relationship exists between the induced e-field and the measurable outcome variable. These advances would, thus, allow cortical localization of single nodes of more complex functions, such as attention or language processing. However, due to a lower signal-to-noise ratio in higher functional domains, more sensitive fitting approaches may have to be used. A higher number of trials might be necessary to yield robust results (Chung et al., 2016).

6.2 Outlook

6.2.1 Future trajectories

Up to now, I have applied this novel TMS mapping approach to pinpoint cortical muscle representations in the primary motor cortex (M1). A limitation of the current implementation is the assumption that a single cortical site is functionally involved in the TMS-modulated output. While this assumption holds for this restricted region of interest in M1, functions in the brain are most often processed via functional networks, spreading across the cortex. To address this interaction of multiple brain regions, the proposed localization method could be extended to allow the identification of interacting neuronal populations, for example, by transitioning from mass-univariate regression to multivariate procedures, i.e., fitting hyperplanes instead of one-dimensional regression lines. In addition, multiple interaction types, i.e., logical operators like OR, AND, and XOR, would have to be tested for all potential connections. This massive increase in tests would likely introduce the need for subsampling strategies to reduce the number of tested elements, faster fitting procedures, and heuristics to select reasonable candidate networks.

For the current, single-node implementation, two main trajectories arise to further exploit the underlying idea to utilize the relationship between induced e-fields and the modulated responses (the cortical I/O curve): I) Due to the precise identification of muscle representations in the motor cortex a dosing strategy based on individual cortical e-field thresholds seems feasible (subsection 6.2.2). II) Examining the cortical I/O curve is not limited to M1 mappings but can potentially also be applied to locate functions of higher cognition (subsection 6.2.3). In principle, every brain function processed in a local cortical region should be localizable with the here presented approach. Below, I outline both approaches and their potential gains for the scientific community.

6.2.2 Applications to dosing

TMS dosing, i.e., the standardization of the stimulation intensity across subjects, is key for successful group-level TMS experiments due to the large inter-individual differences of TMS thresholds. Especially the skin–cortex distance and individual

gyrification patterns yield highly individual stimulator intensities to activate cortical neurons effectively. Up to now, simplistic *heuristics* (subsection 2.3.1) have been used to assess this variability across subjects. In short, the individual sensitivity to TMS is assessed employing motor cortex excitability due to the availability of a quantitative outcome metric: the motor threshold (MT). Subsequently, TMS at the study's real target brain region is applied at the motor threshold or an adjusted MT intensity. Critically, individual *thresholds* here are quantified in terms of the TMS device stimulat*or* intensity, whereas the cortical stimulat*ion* intensity is what drives the physiological effect (see subsection 2.2.1). Thus, differences in cortical stimulation exposure are critically underappreciated, both within and across subjects.

The advent of precise and individual cortical field thresholds

Now, with a TMS mapping approach that can precisely pinpoint the MEPs' origins within gray matter, an individual stimulation threshold can finally be quantified via the cortical e-field exposure itself. A precise localization of finger muscle representations (chapter 4) and, subsequently, an accurate assessment of the resting motor threshold (rMT; subsection 5.3.5) renders the readout of the specific e-field strength to activate cortical neurons possible – on the subject-level.

This dosing metric reproduces the same cortical stimulation strength as rMT stimulation at the primary motor cortex yields – at any given cortical target.

In-silico comparison between dosing metrics

I virtually applied this novel dosing metric based on the *cortical e-field threshold* to a set of subjects who took part in the localization study presented above (chapter 4). Specifically, I extracted the realized induced e-field magnitude at each subject's individual FDI muscle representation for the stimulation intensity that elicited MEPs of $50\,\mu\text{V}$. This MEP amplitude is the default MEP threshold for the *5–10–Rothwell* method (subsection 2.3.2), against which this novel, cortical e-field-based dosing metric was tested. I compared this to the cortical stimulation strengths yielded by the two current major dosing approaches, which either rely on the rMT alone or adjust the stimulator intensity based on the cortex–to–skin distance (*Stokes* algorithm, subsubsection 2.3.1.2). I chose two prototypical cortical targets as virtual TMS

targets to compare these three dosing metrics:

   i) right primary motor cortex ($M1_{right}$)
   ii) left inferior parietal lobe (IPL_{left})

The first virtual target, $M1_{right}$, is the homologue of the left primary motor cortex ($M1_{left}$), from which the cortical e-field threshold is extracted, Choosing an area of comparable physiological properties allows for estimating differences of the TMS-induced effects of the three dosing approaches stemming from differences in the cortical stimulation exposure. Under the assumption of similar neuronal activation profiles between the left and right motor cortices, and the fitted I/O curve from $M1_{left}$ are used to quantify the TMS effect in $M1_{right}$ across the different dosing approaches. The second virtual target, IPL_{left}, has previously been targeted in numerous TMS studies to examine its causal relevance for a set of higher-cognitive functions, including attentional processes, semantic processing, and social cognition (Numssen, Bzdok, & Hartwigsen, 2021; Krall et al., 2016; Hartwigsen et al., 2010). For both, I followed the current standard procedure to define individual targets in TMS studies: First, the target coordinates in a standard brain template space (MNI template) were selected from an existing fMRI study. Second, these group-level coordinates were transformed into each individual subject space. Third, if this transformation yielded coordinates outside of gray matter, the closest gray matter location was chosen as the final target instead.

DOSING VIA RESTING MOTOR THRESHOLDS (rMT). Studies relying on the rMT apply this stimulator intensity or a percentage of it. Here, 100 %rMT was used to allow for a straightforward comparison between the different dosing approaches.

DOSING VIA THE STOKES ALGORITHM. This dosing procedure has been introduced as a "[s]imple metric for scaling motor threshold based on scalp-cortex distance" (Stokes et al., 2005). Differences in the cortical depth between $M1_{left}$ and the real cortical target are taken into account in a linear fashion (cf. subsubsection 2.3.1.2). Specifically, for each millimeter difference between both targets, the stimulator intensity is adjusted by 3 %MSO. Importantly, $M1_{left}$, in this case, is usually manually chosen as the gray matter surface of the hand knob ($M1_{hand}$).

DOSING VIA CORTICAL E-FIELD THRESHOLDS. This metric assumes a similar neuronal e-field activation threshold with respect to the induced e-field from TMS across the cortex. Accordingly, the cortical FDI representation identified in chapter 4 is used to find the individual e-field magnitude yielding MEPs of 50 µV (cf. Rossini et al., 1994). This threshold can either be extracted from the fitted cortical I/O curve at the FDI representation (Chapter 5, step 53) or can be experimentally assessed (see Equation 6.1) following a precise rMT determination (subsection 5.3.5).

$$\%MSO_{target} = rMT * |E|_{FDI}^{1A/\mu s} * fac \qquad \text{e-field based dosing} \quad (6.1)$$

where:

$\%MSO_{target}$ = stimulator intensity in %MSO for the cortical target,

rMT = resting motor threshold in %MSO,

$E_{FDI}^{1\%MSO}$ = e-field magnitude at FDI location for 1 A/µs stimulator output,

fac = vendor specific A/µs to %MSO conversion factor.

To yield a stable e-field estimate, a spherical ROI with 2 mm diameter was placed around the identified cortical FDI representation in $M1_{left}$ and masked to gray matter tissue. The same ROI definition was used for the other two cortical targets ($M1_{right}$, IPL_{left}) to extract the e-field's magnitude for the dosing strategies described above.

RESULTS. On average, the three cortical targets differed in cortical depth: $M1_{left}$: 9.85 mm ± 1.69 mm; $M1_{right}$: 14.18 mm ± 0.85; IPL: 8.05 mm ± 1.2 mm. Across subjects, the cortical e-field threshold to elicit MEPs of 50 µV was 65.35 V/m ± 6.32 V/m.

Both rMT-based approaches could not reproduce the cortical e-field exposure assessed at M1 for rMT stimulator intensity (see Figure 6.1 for whole brain results for an exemplary subject and Figure 6.2 for group-level results). Cortical e-field exposures from the plain rMT dosing approach were highly correlated with cortical depth differences between $M1_{left}$ and $M1_{left}$ or IPL, respectively. Here, IPL stimulation was of comparable strength on average, with distinct deviations on the subject-level and significantly lower in $M1_{right}$. Also, the Stokes algorithm did not fully compensate for the observed differences in stimulation strength: Cortical stimulation at $M1_{right}$
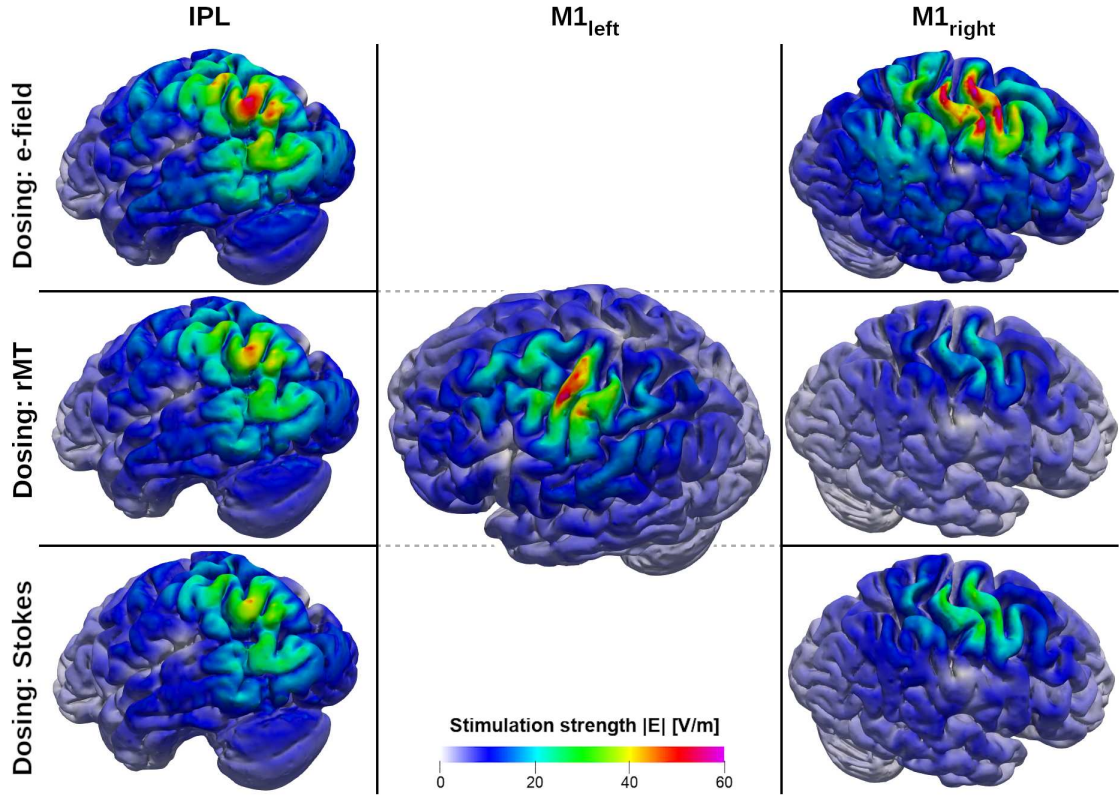
Figure 6.1: The cortical stimulation exposure differs across dosing strategies.
Virtual comparison between three TMS dosing strategies: I) e-field-based, II) resting motor
threshold (rMT) based, and III) rMT adjusted via the Stokes algorithm, shown for an
exemplary subject (S03). Center column: All three dosing strategies are based on left
primary motor cortex ($M1_{left}$) stimulation, yielding $50\,\mu V$ motor evoked potentials (MEPs)
of the right index finger (FDI) muscle. Top row: e-field-based dosing yields the same
cortical stimulation strength at all cortical targets, i.e., inferior parietal lobe (IPL; left
column) and right primary motor cortex ($M1_{right}$; right column). Center row: rMT-based
dosing applies the same stimulat*or* intensity for all targets, yielding strongly differing (here:
reduced) cortical stimulat*ion* strength across targets. Bottom row: The Stokes heuristic
tries to compensate for different cortical depths without yielding satisfactory results. Color:
Electric field magnitude $|E|$, shown on gray matter surface.

was, on average, closer to the cortical e-field threshold (Stokes-adjusted: 47.24 V/m
$\pm$ 12.51 V/m; rMT-based: 35.84 V/m $\pm$ 13.34 V/m), but still significantly lower.
The TMS-induced effects, quantified via MEP amplitudes, differed similarly between
the dosing strategies. Paralleling the induced e-field strengths, rMT-based dosing
(0.0085 mV $\pm$ 0.0036 mV) yielded significantly smaller MEPs compared to e-field-
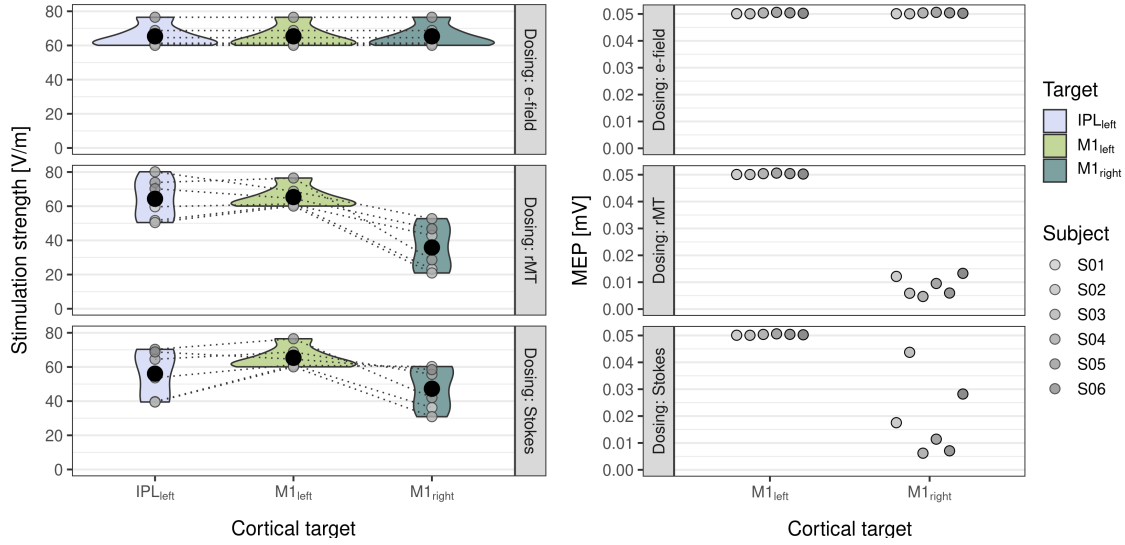
Figure 6.2: MT-based dosing significantly understimulates the cortical tissue.
The cortical stimulation (left, e-field magnitude $|E|$) and the TMS-induced effects (right, motor evoked potential (MEP) amplitudes) show high levels of variability across cortical sites when the stimulation strength is adjusted based on the MT or the Stokes algorithm. Left: The cortical stimulation strength (e-field magnitude $|E|$) at two cortical targets (IPL$_{left}$, M1$_{right}$) compared to M1$_{left}$. MT based dosing yields significantly lower stimulation exposure for all subjects at M1$_{right}$ and varying stimulation strength at the IPL target. Adjusting for different cortical depths via the Stokes algorithm worsens the cortical stimulation strength for the IPL$_{left}$ target and improves results for M1$_{right}$. Black points: average stimulation strength.
Right: TMS effects differ drastically between the three dosing strategies. MEPs for M1$_{right}$ were calculated with the I/O curves M1$_{left}$, which were fit on experimental data. Both, rMT-based and Stokes adjusted dosing yields significantly lower MEPs than the e-field-based dosing strategy.

based dosing (0.05 mV $\pm$ 0.0002 mV). Adjusting the simulator intensity via the Stokes algorithm improved the results (Stokes-adjusted: 0.019 mV $\pm$ 0.0145 mV).

In summary, this virtual TMS dosing study identified serious shortcomings in dosing approaches that solely rely on the MT in terms of stimulator intensity. These dosing regimes lead to a considerable, unexplained variance of the cortical stimulation strength, i.e., over- or understimulation, and thereby unreliable TMS-induced effects. Together, these results underline the importance of defining a subject- and target-specific TMS intensity based on the cortical stimulation exposure instead of relying on motor threshold dosing approaches.

6.2.3 Mapping higher cognition with TMS

From its very first methodological beginnings, TMS has been used to gain insights into causal structure-function relationships of the human brain (Magnusson & Stevens, 1914; Hess et al., 1987). However, despite its strong physiological effects, directly affecting brain processing via superthreshold neuronal stimulation, TMS studies often lack strong effect sizes on the group-level. In addition to a physiologically motivated dosing strategy (see above), a method to precisely locate cognitive functions within the cortex on the subject-level with TMS is currently lacking.

Below, I outline the utilization of the mapping approach presented in chapter 4 to locate a cognitive process. To my best knowledge, this is the first example of localization in the cognitive domain on the subject-level, which is based on cortical I/O curves, i.e., the quantification of the behavioral effect of the induced e-field. Specifically, locating attentional reorienting processes in the right inferior parietal lobe (IPL_{right}) in a single subject is used as an exemplary use case.

Attentional reorienting

Experimental paradigm. Attentional reorienting processes have been localized in the right IPL (IPL_{right}) via TMS on the group-level before (Rushworth et al., 2001) with variants of the Posner task (Posner, 1980). All Posner-like tasks are based on violating a previously built spatial expectancy.

Specifically, in each trial, two empty rectangular boxes are presented side-by-side on a screen to the volunteer with a fixation cross at the center of the screen. In the *cue*–phase (250 ms or 350 ms) the fixation cross is replaced with an arrow either pointing left or right. In the *target* phase, an asterisk is presented in one of the boxes. In 75 % of the trials, the target's location is congruent with the cue arrow (*valid* condition). In 25 % of the trials, the target is presented at the incongruent side (*invalid* condition; see Numssen, Bzdok, and Hartwigsen (2021) for task details).

Due to the high probability of congruent trials (*valid* trials) an expectancy is built for the target's position. In case of violating this expectancy (*invalid* trials), attentional reorientation processes are triggered.

Experimental design. The experimental design for the TMS localization was closely matched to the primary motor cortex mapping technique (chapter 4). For each

trial of the Posner-like task, one stimulation at a quasi-random TMS coil position and orientation around the IPL_{right} region was given. In contrast to the single TMS pulses used before, here, an rTMS protocol (five pulse burst at 10 Hz, 20 ms after target presentation) was used following previous literature (Rushworth et al., 2001). In total, 500 trials in blocks of 100 were shown to the subject, yielding 125 *invalid* trials and 375 *valid* trials. The same task was presented in a 3 T fMRI (Siemens Skyra) to the same subject to provide data to test the TMS localization against. The fMRI analysis followed standard procedures for mass-univariate analyses of local brain activity. Specifically, an echo planar-imaging (EPI) sequence was acquired during the task to yield an estimate of local brain processing demands (blood oxygen level-dependent imaging; BOLD). The fMRI data were preprocessed with fMRIPrep (v21.0.1; Esteban et al., 2019, 2020), a pipeline to apply minimal, standardized, and reproducible pre-processing. A 5 mm full-width half-maximum (FWHM) smoothing kernel was applied, the design matrix was specified with nipype (v1.8.3; Gorgolewski et al., 2016), and the voxel-wise generalized linear models (GLMs) were computed with SPM12 (www.fil.ion.ucl.ac.uk/spm). Finally, the voxel-wise contrast for the GLM betas $invalid - rest$ was computed to remove task-unrelated brain activity.

RESULTS. Out of 125 invalid trials, 104 were answered correctly (83.2 %) and within the expected response time limits (100 ms to 500 ms). The response times for *invalid* trials were slower (245 ms $\pm$ 37 ms than for *valid* trials (194 ms $\pm$ 41 ms) and well within the range of previous experiments (Numssen, Bzdok, & Hartwigsen, 2021). The fMRI results (Figure 6.3) identified one anterior cluster within the supramarginal gyrus (X: 39, Y: -64, Z: 12) and one posterior cluster (X: 39, Y: -77, Z: -25) regions within angular gyrus to be specifically active during processing the *invalid* trials. Lowest T-values were calculated within the sulcus between the supramarginal gyrus and angular gyrus, i.e., approximately between the cytoarchitectonic regions PFm and Pf (Zilles & Amunts, 2010). This pattern was paralleled to large parts by the TMS mapping results of the attentional reorienting processes: Lowest R^2 values were calculated at the transition between the supramarginal and angular gyri, and the highest R^2 values in the dorsal part of the anterior IPL_{right} part (X: 42.2, Y: -64.9, Z: 10.2) and in the inferior part of the angular gyrus (X: 34.9, Y: -72.7, Z: -22.1).

These results stem from a straightforward implementation of the novel TMS mapping
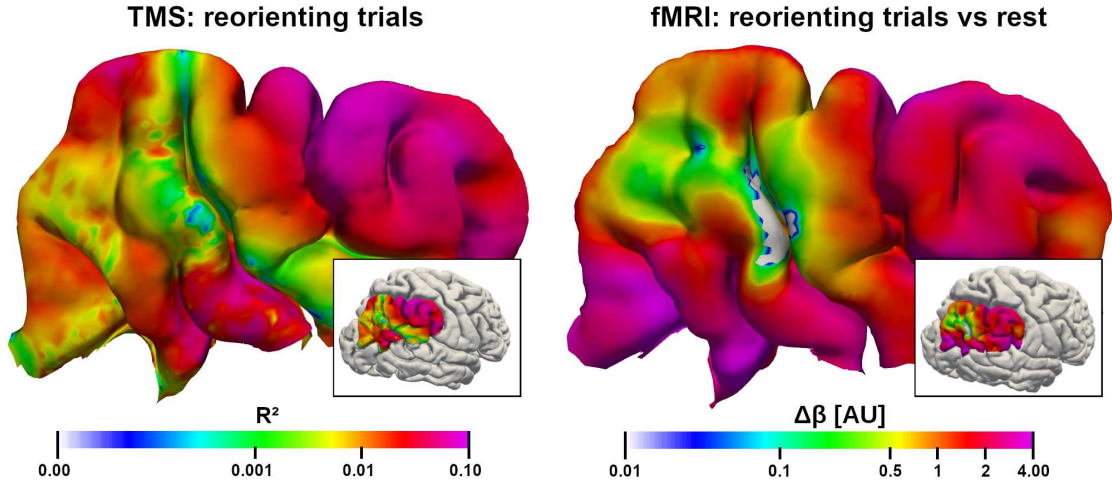
Figure 6.3: TMS localization of attentional processes reproduces fMRI results.
Single-subject results for a standard fMRI analysis (right) of attentional reorienting and
with TMS (left). The same Posner-like task was used in both modalities (see text). For
the novel TMS mapping approach, the local induced e-fields from quasi-random coil
positions were regressed on the reaction times from the attentional reorienting trials,
i.e., the *invalid* condition. For the fMRI analysis, the contrast *invalid − rest* was
computed to remove task-unrelated brain activity from attentional reorienting related
processes. Color: R^2 goodness-of-fit for sigmoidal rt $|E|$ fits (left). GLM beta differences
for *attentional reorienting − rest* (right); Results are shown on the gray matter surface
in the right inferior parietal lobe (IPL_{right}) region of interest.

strategy developed in the motor domain to locate attentional processes – without any
in-depth adaptations to this cognitive regime. Despite distinct differences between
these two domains, for example, noise levels of the output measures and different
saturation levels of the TMS effects, relevant features of an fMRI-based localization
were discovered with the TMS-based localization. Nevertheless, also differences exist
between both mapping approaches, potentially due to multiple cortical regions being
involved in the processing. In addition, if TMS targets – and thus, identifies – the
same neuronal populations as fMRI remains elusive.

Together, this first application of the cortical TMS mapping strategy in a cognitive
domain yielded promising results. It revealed several directives that will have to be
assessed to fully leverage its potential gains in this domain.

6.3 Conclusions

In the works presented above, I introduced a novel approach to identify functionally relevant cortical regions with TMS– together with a principled and working implementation of this rationale. This mapping approach relies on the assessment of the functional relationship itself between the local TMS-induced e-field strength and the evoked response, for example, MEPs to map the primary motor cortex. This combination of state-of-the-art e-field modeling to precisely estimate the induced e-fields for individual head and brain anatomies with prior knowledge about the input-output behavior of cortical motor neurons enabled a precise cortical mapping of causally involved neuronal populations. Based on an initial proof-of-concept realization, I developed a more efficient and robust implementation to realize this rationale with the use of quasi-random stimulation positions and orientations. Notably, this efficient implementation has been realized in a set of fourteen healthy subjects with consistent, precise results, with a subsequent experimental session underlining the method's validity. However, besides *validity*, also *applicability* was a major development aim, reflected in a simple experimental design and short experimental duration.
This dual focus was further underlined with the publication of an extensive set of in-depth explanations to implement this mapping procedure, including all necessary scripts and analysis code.

The proposed mapping approach is currently fully usable to map motor cortices, with superiority to current mapping approaches, concerning experimental duration, localization precision (also within the cortical tissue), and scientific integrity. However, the underlying idea to exploit the functional relation between e-field and response at the cortical level to locate functions is not limited to motor cortices or other primary regions of the human brain. Instead, this concept should also be profitable for higher cognition, a domain that suffers from high inter-individual variation and low – and sometimes unpredictable – TMS effects. The precise cortical localization of cortical muscle representations on the individual level and individual activation profiles of such, allow precise quantification of cortical e-field thresholds. Quantifying this individual activation threshold with respect to the induced e-field allows for an objective and physiologically based TMS dosing scheme. Finally, I presented an initial application of the technique to map attentional processes to show its full potential.

Despite further work being necessary to adapt the analysis to this functional domain and to strengthen the hypotheses of the neuronal activation profiles, these initial results provide a promising outlook into potential future adaptations of the underlying rationale.

I hope this work will be adapted in the ever-advancing non-invasive brain stimulation field and genuinely think it will prove its virtue.

Appendices

Appendix A: Congruence factor implementation

```
1  def congruence_factor(elm_idx_list, mep, mep_params, e, n_samples=100):
2      """
3      Calculate congruence factors for given zaps and elements,
         ↪   parallelized over elements, MEP fit is discretized into
         ↪   n_samples.
4
5      Parameters
6      ----------
7      elm_idx_list : np.ndarray
8          List of element indices to compute.
9      mep : list of Mep object
10         List of fitted Mep objects for all conditions.
11     mep_params : np.ndarray of float
12         Mep parameters of curve fits used to calculate the MEP.
13         - e.g.: [mep_#1_para_#1, mep_#1_para_#1, mep_#2_para_#1, ...]
14     e : list of list of np.ndarray of float
15         Electric fields, e.g., (e_mag, e_norm, e_tan).
16     n_samples : int, default=100
17         Discretization resolution and e curves.
18
19     Returns
20     -------
21     congruence_factor : np.ndarray of float [n_roi, n_datasets]
22         Congruence factor in each elm_idx and for each input dataset
23     """
24
25     [...]
26     # congruence factor calculation for a single element
27     for cond in conditions:
28         last_cond = cond
29         # resample intensity axis of shifted mep curve
30         n_steps = ((e_min[ref] - shift[ref]) - ((e_min[ref] -
            ↪   shift[ref]) / intensities_max[cond] *
            ↪   intensities_min[cond])) / shift[ref]
31         intens_mep = np.linspace(intensities_min[cond],
            ↪   intensities_max[cond], n_steps)
32
33         # initial shift (e'_mep)
34         initial_shift = (e_min[ref] - shift[ref]) /
            ↪   intensities_max[cond]
```

```
35
36          # start index of initially shifted and stretched mep curve
37          start_mep_shift = find_nearest(e_x_global, initial_shift *
            ↪  intensities_min[cond])
38          mep_shift = mep[cond].eval(intens_mep, mep_params[cond])
39
40          # determine length of mep curve w.r.t. its location
41          max_e_mep_end = (e_max[ref] + shift[ref]) *
            ↪  intensities_max[cond] / intensities_min[cond]
42          len_e_mep_start = mep_shift.size
43          len_e_mep_end = np.ceil((max_e_mep_end - e_max[ref] +
            ↪  shift[ref]) / shift[ref])
44
45          # length of shifted curve as a function of position (gets
            ↪  longer while shifting)
46          len_mep_shift = np.round(np.linspace(len_e_mep_start,
            ↪  len_e_mep_end, len_e_mep_start + n_samples + 2 *
            ↪  shift[ref]))
47
48          # construct shift array
49          stepsize_shift_intens = (intensities_max[ref] -
            ↪  intensities_min[ref]) \ n_samples
50          min_intens_ref = intensities_min[ref] - stepsize_shift_intens *
            ↪  (1 + len_e_mep_start)
51          max_intens_ref = intensities_max[ref] + stepsize_shift_intens *
            ↪  (1 + len_e_mep_end)
52
53          shift_array = mep[ref].eval(np.arange(min_intens_ref,
            ↪  max_intens_ref, stepsize_shift_intens), mep_params[ref])
54
55          # generate index shift list to compare curves
56          slice_idx = np.outer(len_mep_shift[:, np.newaxis],
            ↪  np.linspace(0, 1, len_e_mep_start)[np.newaxis, :])
57          slice_idx = np.round(np.add(slice_idx,
            ↪  np.arange(slice_idx.shape[0])[:, np.newaxis])).astype(int)
58
59          # the error is y-difference between mep[idx] and
            ↪  mep[reference].zero_padded
60          err = np.sqrt(np.sum((shift_array[slice_idx] - mep_shift) ** 2,
            ↪  axis=1))
61
62          # which shift leads to minimum error
63          tau_cond[ref, last_cond] = (start_mep_shift - start_ind[cond])
            ↪  * stepsize + np.argmin(err) * shift[ref]
64
```

```
65  # sum up errors and divide by e_mean over all conditions
66  congruence_factor = 1 / (np.sqrt(np.sum(np.square(tau_cond) * 2)) /
    ↪  e_mean / n_conditions / (n_conditions - 1))
```

Listing A.1: Initial congruence_factor() code to calculate the congruence factor. Cut to code section to compute the congruence factor for a single cortical element.

Appendix B: Experiment 1: Permutation results
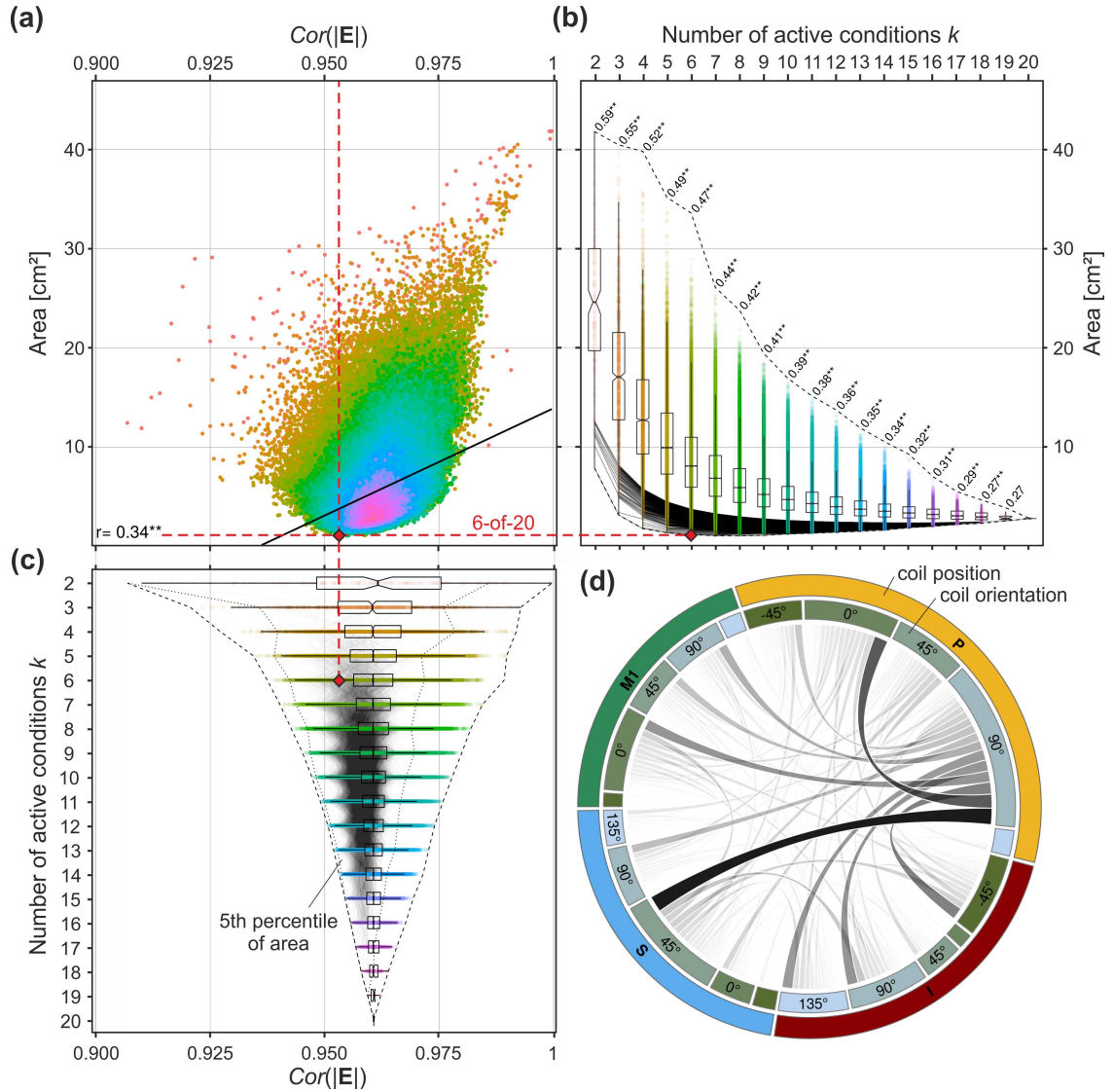
Figure B.1: De-correlated e-fields yield a better localization (Sub01).
See Figure 3.10 for details. Dashed red line: Set of six coil positions/orientations yielding
the best localization result. Its cross-correlation coefficient ($r = 0.953$) is lower than
the first quartile of possible solutions. (a) Relationship between cross-correlation of the
e-field magnitude and hotspot area size. The correlation between hotspot size and e-field
cross-correlation for all $k = 20$ is $r = 0.34; p \ll .001$. (b) The hotspot area of the congruence
factor decreases with an increasing number of conditions k. (c) Relationship between the
cross-correlation coefficient of the e-fields and the number of active conditions k. (d) Paired
proportions of coil positions (outer circle) and orientations (inner circle) from upper 5th
percentile of all combinations ($k = 20$) yielding good localization results (black lines in
(b)). Figure published initially in Weise & Numssen et al. (2020).
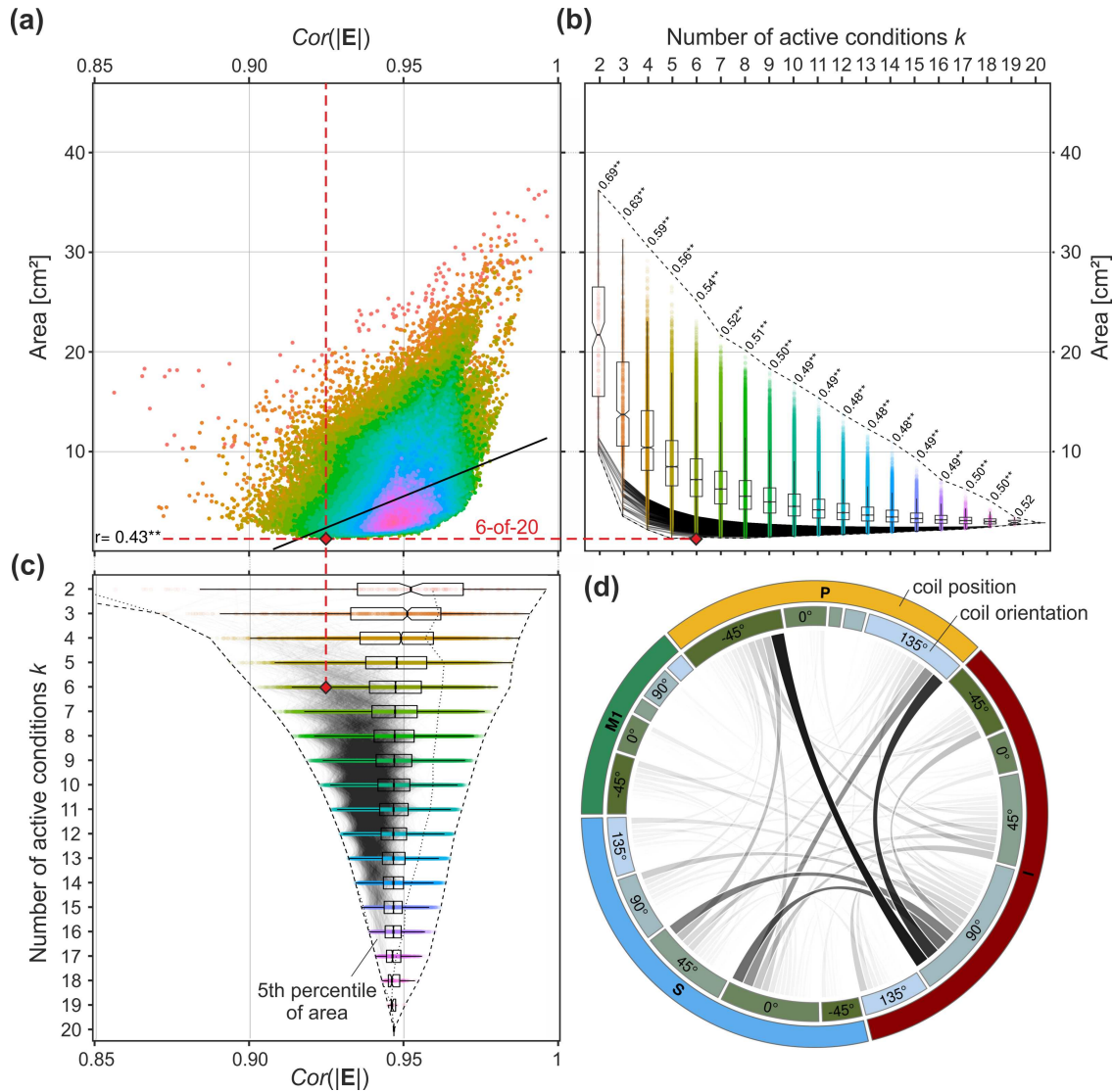
Figure B.2: De-correlated e-fields yield a better localization (Sub12).
See Figure 3.10 for details. Dashed red line: Set of six coil positions/orientations yielding the best localization result. Its cross-correlation coefficient ($r = 0.925$) is lower than the first quartile of all possible solutions. (a) Relationship between cross-correlation of the e-field magnitude and hotspot area size. The correlation between hotspot size and e-field cross-correlation for all $k = 20$ is $r = 0.43; p \ll .001$. (b) The hotspot area of the congruence factor decreases with an increasing number of conditions k. (c) Relationship between the cross-correlation coefficient of the e-fields and the number of active conditions k. (d) Paired proportions of coil positions (outer circle) and orientations (inner circle) from upper 5th percentile of all combinations ($k = 20$) yielding good localization results (black lines in (b)). See Figure 3.10 for details. Figure published initially in Weise & Numssen et al. (2020).
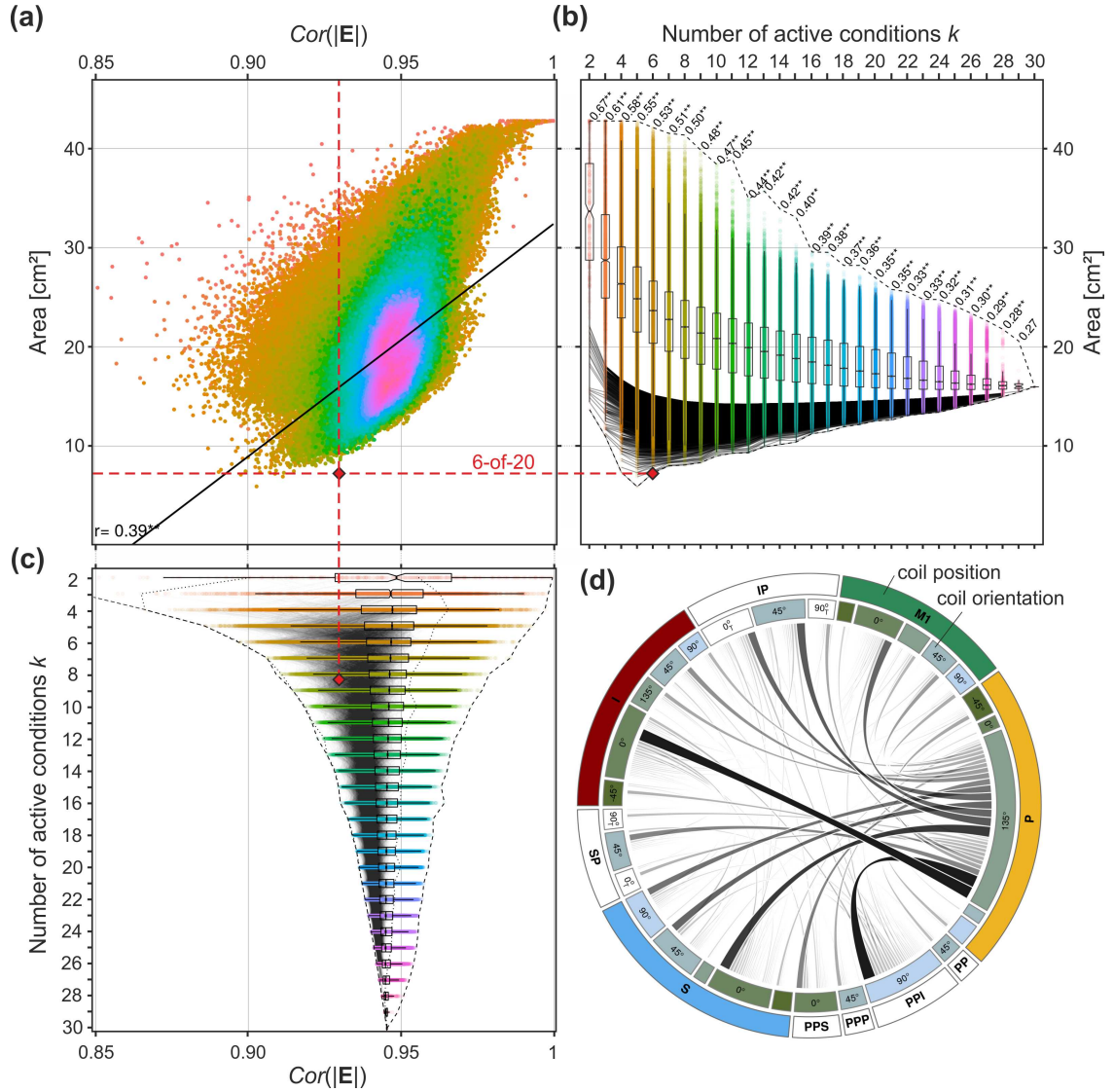
Figure B.3: De-correlated e-fields yield a better localization (Sub15).
See Figure 3.10 for details. Dashed red line: Set of six coil positions/orientations yielding the best localization result. Its cross-correlation coefficient ($r = 0.93$) is lower than the first quartile of possible solutions. (a) Relationship between cross-correlation of the e-field magnitude and hotspot area size. The correlation between hotspot size and e-field cross-correlation for all $k = 20$ is $r = 0.39$ $p \ll .001$. (b) The hotspot area of the congruence factor decreases with an increasing number of conditions k. (c) Relationship between the cross-correlation coefficient of the e-fields and the number of active conditions k. (d) Paired proportions of coil positions (outer circle) and orientations (inner circle) from upper 5th percentile of all combinations ($k = 20$) yielding good localization results (black lines in (b)). White color indicates the additional coil positions and the superscript T indicates a tilted coil orientation (Figure 3.13) See Figure 3.10 for details. Figure published initially in Weise & Numssen et al. (2020).

Appendix C: Calculating the optimal coil configurations

```
1  def optimize_tms_coil_pos(tms_optim, target=None, handle_dir=None,
   ↪   radius=20, angle_limits=None, resolution_pos=1.5,
   ↪   resolution_angle=15, n_cpu=1):
2      """
3      Compute optimal TMS coil position/rotation for maximum field at
           ↪   cortical target. This implements a brute-force approach to
           ↪   find the optimal coil position & rotation to maximize normE at
           ↪   a given cortical target. The target is projected to the
           ↪   nearest position at the skin surface and candidate coil
           ↪   positions/rotations are then distributed equally in a circular
           ↪   plane around that location.
4      The number of candiate coil positions/rotations is defined by the
           ↪   two resolution parameters (_pos and angle), the radius of the
           ↪   circular plane, and angle_limits.
5      All simulations are stored in one .hdf5 file.
6
7      Parameters
8      ----------
9      target: np.ndarray or list of float
10         XYZ coordinates to optimize coil position/rotation for.
11     tms_optim: simnibs.TMSOPTIMIZATION
12         Session object with TMSLIST().
13     handle_dir: list of num or np.ndarray
14         Coil handle prolongation. Default: left M1-45° (-2.8, 7, 8.1).
15     radius: float (Default: 20.)
16         Region of interest (ROI) radius around skin target.
17     resolution_pos: float  (Default: 1.5)
18         Resolution in mm of the coil positions in the ROI.
19     resolution_angle: float (Default: 15)
20         Resolution in deg of the coil positions in the region of
              ↪   interest.
21     angle_limits: list of int or np.ndarray (Default: [-60, 60])
22         Range of angles to get coil rotations for.
23     n_cpu: Int (Default: 1)
24         Number of cores to use.
25
26     Returns
27     -------
```

```
28       file
29           all simulations are stored in tms_optim.fname_hdf5
30       file
31           |tms_optim.qoi| at tms_optim.target for all simulations saved
             ↪  in pathfem/tms_optim.optim_name + tms_optim.timestr + .csv
32       file
33           TMSOPTIMIZATION() to run simulations in
             ↪  pathfem/tms_optim.optim_name + tms_optim.time_str + .mat
34       file
35           TMSOPTIMIZATION() with optimal coil positions in
             ↪  pathfem/tms_optim.optim_name + tms_optim.time_str +
             ↪  optimal_coil_pos.mat
36       dict
37           'best_conds': simnibs.TMSLIST() for optimal coil position(s)
38           'simulations': simulation filenames,
39           'tms_optim': simnibs.SESSION() object used for simulation
40       """
41
42       # some argument checks, defaults, type handling
43       if angle_limits is None:
44           angle_limits = [-60, 60]
45       if handle_dir is None:
46           handle_dir = np.array([-2.8, 7, 8.1])
47
48       assert tms_optim.optimlist, "Please provide
         ↪  simnibs.simulation.sim_struct.TMSOPTIMIZATION with TMSLIST
         ↪  optimlist."
49       assert tms_optim.radius >= tms_optim.resolution_pos
50       if not tms_optim.optimlist.pos and not tms_optim.target:
51           raise ValueError("Provide either target or
             ↪  tms_optim.optimlist.pos .")
52
53       # run simulations
54       simnibs.utils.simnibs_logger.logger.info(f"Starting optimization:
         ↪  {len(tms_optim.optimlist.pos)} FEMs on {n_cpu} cpus")
55       simulations_fn = tms_optim.run(allow_multiple_runs=True,
         ↪  cpus=n_cpu)
56
57       # evaluate all simulations
58       # This returns a TMSOPTIMIZATION() with the optimal
         ↪  position/orientation
59       tms_list_optim = eval_optim(simulations_fn, target, tms_optim,
         ↪  os.path.join(tms_optim.pathfem,
         ↪  f"{tms_optim.optim_name}_{tms_optim.time_str}.csv"),
         ↪  qoi=tms_optim.qoi)
```

```
60
61      # return best position
62      return {'best_conds': tms_list_optim, 'simulations':
        ↪   simulations_fn, 'tms_optim': tms_optim}
```

Listing C.1: Relevant parts of `optimize_tms_coil_pos()` code to perform TMS coil optimization based on the e-field magnitude $|E|$.

References

Aberra, A. S., Peterchev, A. V., & Grill, W. M. (2018). Biophysically realistic neuron models for simulation of cortical stimulation. *Journal of Neural Engineering*, *15*(6). doi: 10.1088/1741-2552/aadbb1

Aberra, A. S., Wang, B., Grill, W. M., & Peterchev, A. V. (2020). Simulation of transcranial magnetic stimulation in head model with morphologically-realistic cortical neurons. *Brain Stimulation*, *13*(1), 175–189. doi: 10.1016/j.brs.2019.10.002

Akaike, H. (1974). A new look at the statistical model identification. *IEEE Transactions on Automatic Control*, *19*(6), 716–723. doi: 10.1109/TAC.1974.1100705

Alavi, S. M. M., Goetz, S. M., & Peterchev, A. V. (2019). Optimal estimation of neural recruitment curves using Fisher information: application to transcranial magnetic stimulation. *IEEE Transactions on Neural Systems and Rehabilitation Engineering*, *27*(6), 1320–1330. doi: 10.1109/TNSRE.2019.2914475

Anatomical Museum, U. o. E. (2018, 7). *3D Printable Phrenological Glazed Head by Anatomical Museum.* Retrieved from https://www.myminifactory.com/object/3d-print-phrenological-glazed-head-70131

Aonuma, S., Gomez-Tames, J., Laakso, I., Hirata, A., Takakura, T., Tamura, M., & Muragaki, Y. (2018). A high-resolution computational localization method for transcranial magnetic stimulation mapping. *NeuroImage*, *172*, 85–93. doi: 10.1016/j.NeuroImage.2018.01.039

Awiszus, F. (2003). TMS and threshold hunting. In *Supplements to clinical neurophysiology* (Vol. 56, pp. 13–23). Elsevier. doi: 10.1016/s1567-424x(09)70205-3

Ayachit, U. (2015). *The ParaView Guide: A Parallel Visualization Application. Available from https://www.paraview.org. [11/03/2022].* Kitware, Inc. Retrieved from https://www.paraview.org doi: 10.5555/2789330

Balslev, D., Braet, W., McAllister, C., & Miall, R. C. (2007). Inter-individual variability in optimal current direction for transcranial magnetic stimulation of the motor cortex. *Journal of Neuroscience Methods*, *162*(1-2), 309–313. doi: 10.1016/j.jneumeth.2007.01.021

Barker, A. T., Jalinous, R., & Freeston, I. L. (1985). Non-invasive magnetic stimulation of human motor cortex. *Lancet*, *1*(8437), 1106e7. doi: 10.1515/eng-2018-0022

Bergmann, T. O., Karabanov, A. N., Hartwigsen, G., Thielscher, A., & Siebner, H. R. (2016). Combining non-invasive transcranial brain stimulation with neuroimaging and electrophysiology: Current approaches and future perspectives. *NeuroImage*, *140*, 4–19. doi: 10.1016/j.neuroimage.2016.02.012

Bergmann, T. O., Mölle, M., Schmidt, M. A., Lindner, C., Marshall, L., Born, J., & Siebner, H. R. (2012). Eeg-guided transcranial magnetic stimulation reveals rapid shifts in motor cortical excitability during the human sleep slow oscillation. *Journal of Neuroscience*, *32*(1), 243–253.

Beynel, L., Appelbaum, L. G., Luber, B., Crowell, C. A., Hilbig, S. A., Lim, W., . . . others (2019). Effects of online repetitive transcranial magnetic stimulation (rtms) on cognitive processing: a meta-analysis and recommendations for future studies. *Neuroscience & Biobehavioral Reviews*, *107*, 47–58.

Bikson, M., Hanlon, C. A., Woods, A. J., Gillick, B. T., Charvet, L., Lamm, C., . . . Others (2020). Guidelines for TMS/tES clinical services and research through the COVID-19 pandemic. *Brain Stimulation*, *13*(4), 1124–1149. doi: 10.1016/j.brs.2020.05.010

Braga, R. M., & Buckner, R. L. (2017). Parallel Interdigitated Distributed Networks within the Individual Estimated by Intrinsic Functional Connectivity. *Neuron*, *95*(2), 457–471.e5. doi: 10.1016/j.neuron.2017.06.038

Brasil-Neto, J. P., Cohen, L. G., Panizza, M., Nilsson, J., Roth, B. J., & Hallett, M. (1992). Optimal focal transcranial magnetic activation of the human motor cortex: Effects of coil orientation, shape of the induced current pulse, and stimulus intensity. *Journal of Clinical Neurophysiology*, *9*(1), 132–136. doi: 10.1097/00004691-199201000-00014

Brasil-Neto, J. P., Cohen, L. G., & Hallett, M. (1994). Central fatigue as revealed by postexercise decrement of motor evoked potentials. *Muscle & Nerve*, *17*(7), 713–719. doi: 10.1002/mus.880170702

Brodmann, K. (1909). *Vergleichende Lokalisationslehre der Grosshirnrinde in ihren Prinzipien dargestellt auf Grund des Zellenbaues* (Vol. 44) (No. 0). Barth.

Bungert, A., Antunes, A., Espenhahn, S., & Thielscher, A. (2016, sep). Where does TMS Stimulate the Motor Cortex? Combining Electrophysiological Measurements and Realistic Field Estimates to Reveal the Affected Cortex Position. *Cerebral Cortex*, 1–12. doi: 10.1093/cercor/bhw292

Chung, S. W., Hill, A. T., Rogasch, N. C., Hoy, K. E., & Fitzgerald, P. B. (2016). Use of theta-burst stimulation in changing excitability of motor cortex: a systematic review and meta-analysis. *Neuroscience & Biobehavioral Reviews*, *63*, 43–64. doi: 10.1016/j.neubiorev.2016.01.008

Clapp, W. C., Hamm, J. P., Kirk, I. J., & Teyler, T. J. (2012). Translating long-term potentiation from animals to humans: A novel method for noninvasive assessment of cortical plasticity. *Biological Psychiatry*, *71*(6), 496–502. doi: 10.1016/j.biopsych.2011.08.021

Conforto, A. B., Kohl, A. S., Kaelin-lang, A., & Ro, K. M. (2004). Impact of coil position and electrophysiological monitoring on determination of motor thresholds to transcranial magnetic stimulation. *Clinical Neurophysiology*, *115*, 812–819. doi: 10.1016/j.clinph.2003.11.010

Dale, A. M., Fischl, B., & Sereno, M. I. (1999). Cortical surface-based analysis: I. Segmentation and surface reconstruction. *NeuroImage*, *9*(2), 179–194. doi: 10.1006/nimg.1998.0395

Davila-Pérez, P., Jannati, A., Fried, P. J., Cudeiro Mazaira, J., & Pascual-Leone, A. (2018). The Effects of Waveform and Current Direction on the Efficacy and Test–Retest Reliability of Transcranial Magnetic Stimulation. *Neuroscience*, *393*, 97–109. doi: 10.1016/j.neuroscience.2018.09.044

De Geeter, N., Crevecoeur, G., Leemans, A., & Dupré, L. (2014). Effective electric fields along realistic DTI-based neural trajectories for modelling the stimulation mechanisms of TMS. *Physics in Medicine & Biology*, *60*(2), 453. doi: 10.1088/0031-9155/60/2/453

Deng, Z. D., Lisanby, S. H., & Peterchev, A. V. (2013). Electric field depth-focality tradeoff in transcranial magnetic stimulation: Simulation comparison of 50 coil designs. *Brain Stimulation*, *6*(1), 1–13. doi: 10.1016/j.brs.2012.02.005

Di Lazzaro, V., Oliviero, A., Pilato, F., Saturno, E., Dileone, M., Mazzone, P., ... Rothwell, J. C. (2004). The physiological basis of transcranial motor cortex stimulation in conscious humans. *Clinical Neurophysiology*, *115*, 255–266. doi: 10.1016/j.clinph.2003.10.009

Drakaki, M., Mathiesen, C., Siebner, H. R., Madsen, K. H., & Thielscher, A. (2021). Validated TMS coil models for electric field simulations. *Brain Stimulation: Basic, Translational, and Clinical Research in Neuromodulation*, *14*(6), 1631. doi: 10.1016/j.brs.2021.10.138

Dubbioso, R., Madsen, K. H., Thielscher, A., & Siebner, H. R. (2021). The myelin content of the human precentral hand knob reflects interindividual differences in manual motor control at the physiological and behavioral level. *Journal of Neuroscience*, *41*(14), 3163–3179. doi: 10.1523/JNEUROSCI.0390-20.2021

Dubbioso, R., Raffin, E., Karabanov, A. N., Thielscher, A., & Siebner, H. R. (2017). Centre-surround organization of fast sensorimotor integration in human motor hand area. *Neuroimage*, *158*, 37–47. doi: 10.1016/j.neuroimage.2017.06.063

Dum, R., & Strick, P. (2004). Motor Areas in the Frontal Lobe. *Physiology & Behavior*, *77*, 677–682. doi: 10.1201/9780203503584.sec1

Epstein, C. M. (2012). TMS stimulation coils. In *Oxford handbook of transcranial stimulation.* doi: 10.1093/oxfordhb/9780198568926.013.0004

Esteban, O., Ciric, R., Finc, K., Blair, R. W., Markiewicz, C. J., Moodie, C. A., ... Gorgolewski, K. J. (2020). Analysis of task-based functional MRI data preprocessed with fMRIPrep. *Nature Protocols*, *15*(7), 2186–2202. doi: 10.1038/s41596-020-0327-3

Esteban, O., Markiewicz, C. J., Blair, R. W., Moodie, C. A., Isik, A. I., Erramuzpe, A., ... Others (2019). fMRIPrep: a robust preprocessing pipeline for functional MRI. *Nature methods*, *16*(1), 111–116. doi: 10.1038/s41592-018-0235-4

Fischl, B., Sereno, M. I., & Dale, A. M. (1999). Cortical surface-based analysis: II. Inflation, flattening, and a surface-based coordinate system. *NeuroImage*, *9*(2), 195–207. doi: 10.1006/nimg.1998.0396

Florman, J. E., Duffau, H., & Rughani, A. I. (2013). Lower motor neuron findings after upper motor neuron injury: Insights from postoperative supplementary motor area syndrome. *Frontiers in Neuroengineering*, *7*(MAR), 1–7. doi: 10.3389/fnhum.2013.00085

Fox, P. T., Narayana, S., Tandon, N., Sandoval, H., Fox, S. P., Kochunov, P., & Lancaster, J. L. (2004). Column-Based Model of Electric Field Excitation of Cerebral Cortex. *Human Brain Mapping*, *22*(1), 1–14. doi: 10.1002/hbm.20006

Gaser, C., Dahnke, R., Thompson, P. M., Kurth, F., & Luders, E. (2022). CAT – A Computational Anatomy Toolbox for the Analysis of Structural MRI Data. *bioRxiv*. doi: 10.1101/2022.06.11.495736

Geeter, N. D., Dupré, L., & Crevecoeur, G. (2016). Modeling transcranial magnetic stimulation from the induced electric fields to the membrane potentials along tractography-based white matter fiber tracts. *Journal of Neural Engineering*, *13*(2), 26028. doi: 10.1088/1741-2560/13/2/026028

Geuzaine, C., & Remacle, J. F. (2009). Gmsh: A 3-D finite element mesh generator with built-in pre- and post-processing facilities. *International Journal for Numerical Methods in Engineering*, *79*(11), 1309–1331. doi: 10.1002/nme.2579

Geveci, B. (2005). ParaView: An End-User Tool for Large Data Visualization ParaViewWeb View project. *Los Alamos national laboratory*, *836*(8). Retrieved from https://datascience.dsscale.org/wp-content/uploads/2016/06/ParaView.pdf

Geyer, S., Ledberg, A., Schleicher, A., Kinomura, S., Schormann, T., Burgel, U., ... Roland, P. E. (1996). Two different areas within the primary motor cortex of man. *Nature*, *382*(6594), 805–807. doi: 10.1038/382805a0

Geyer, S., Matelli, M., Luppino, G., & Zilles, K. (2000). Functional neuroanatomy of the primate isocortical motor system. *Anatomy and embryology*, *202*(6), 443–474.

Glasser, M. F., Coalson, T. S., Robinson, E. C., Hacker, C. D., Harwell, J., Yacoub, E., ... Van Essen, D. C. (2016). A multi-modal parcellation of human cerebral cortex. *Nature*, *536*(7615), 171–178. doi: 10.1038/nature18933

Glasser, M. F., & van Essen, D. C. (2011). Mapping human cortical areas in vivo based on myelin content as revealed by T1- and T2-weighted MRI. *Journal of Neuroscience*, *31*(32), 11597–11616. doi: 10.1523/JNEUROSCI.2180-11.2011

Goetz, S. M., Alavi, S. M. M., Deng, Z.-D., & Peterchev, A. V. (2019). Statistical model of motor-evoked potentials. *IEEE Transactions on Neural Systems and Rehabilitation Engineering*, *27*(8), 1539–1545.

Goetz, S. M., Luber, B., Lisanby, S. H., & Peterchev, A. V. (2014). A novel model incorporating two variability sources for describing motor evoked potentials. *Brain Stimulation*, *7*(4), 541–552.

Goldsworthy, M. R., Hordacre, B., & Ridding, M. C. (2016). Minimum number of trials required for within-and between-session reliability of TMS measures of corticospinal excitability. *Neuroscience*, *320*, 205–209. doi: 10.1016/j.neuroscience.2016.02.012

Gomez, L. J., Dannhauer, M., Koponen, L. M., & Peterchev, A. V. (2020). Conditions for numerically accurate TMS electric field simulation. *Brain Stimulation*, *13*(1), 157–166. doi: 10.1016/j.brs.2019.09.015

Gorgolewski, K. J., Esteban, O., Burns, C., Ziegler, E., Pinsard, B., Madison, C., ... Ghosh, S. (2016, apr). *Nipype: a flexible, lightweight and extensible*

neuroimaging data processing framework in Python. 0.12.0-rc1. Zenodo. doi: 10.5281/zenodo.50186

Gray, H. (1918). *Anatomy of the human body. Philadelphia: Lea & Febiger, 1918; Bartleby.com, 2000.*

Graziano, M. S., Taylor, C. S., & Moore, T. (2002). Complex movements evoked by microstimulation of precentral cortex. *Neuron*, *34*(5), 841–851. doi: 10.1016/S0896-6273(02)00698-0

Güllmar, D., Haueisen, J., & Reichenbach, J. R. (2010). Influence of anisotropic electrical conductivity in white matter tissue on the EEG/MEG forward and inverse solution. A high-resolution whole head simulation study. *NeuroImage*, *51*(1), 145–163.

Hagan, C. E., Bolon, B., & Keene, C. D. (2012). *Nervous System* (First Edit ed.). Elsevier Inc. doi: 10.1016/B978-0-12-381361-9.00020-2

Hallett, M. (2007). Transcranial Magnetic Stimulation: A Primer. *Neuron*, *55*(2), 187–199. doi: 10.1016/j.neuron.2007.06.026

Hammond, G. (2002). Correlates of human handedness in primary motor cortex: A review and hypothesis. *Neuroscience and Biobehavioral Reviews*, *26*(3), 285–292. doi: 10.1016/S0149-7634(02)00003-9

Hannah, R., Rocchi, L., Tremblay, S., & Rothwell, J. C. (2016). Controllable pulse parameter tms and tms-eeg as novel approaches to improve neural targeting with rtms in human cerebral cortex. *Frontiers in neural circuits*, *10*, 97.

Hannah, R., & Rothwell, J. C. (2017). Pulse duration as well as current direction determines the specificity of transcranial magnetic stimulation of motor cortex during contraction. *Brain stimulation*, *10*(1), 106–115.

Hartwigsen, G., Baumgaertner, A., Price, C. J., Koehnke, M., Ulmer, S., & Siebner, H. R. (2010). Phonological decisions require both the left and right supramarginal gyri. *Proceedings of the National Academy of Sciences*, *107*(38), 16494–16499. doi: 10.1073/pnas.100812110

Hartwigsen, G., Bergmann, T. O., Herz, D. M., Angstmann, S., Karabanov, A. N., Raffin, E., ... Siebner, H. R. (2015). Modeling the effects of noninvasive transcranial brain stimulation at the biophysical, network, and cognitive Level. In *Progress in brain research* (Vol. 222, pp. 261–287). Elsevier B.V. doi: 10.1016/bs.pbr.2015.06.014

Hartwigsen, G., & Bzdok, D. (2018). Multivariate single-subject analysis of short-term reorganization in the language network. *Cortex*, *106*, 309–312. doi: 10.1016/j.cortex.2018.06.013

Hartwigsen, G., Saur, D., Price, C. J., Ulmer, S., Baumgaertner, A., & Siebner, H. R. (2013). Perturbation of the left inferior frontal gyrus triggers adaptive plasticity in the right homologous area during speech production. *Proceedings of the National Academy of Sciences of the United States of America*, *110*(41), 16402–16407. doi: 10.1073/pnas.1310190110

Hess, C., Mills, K. R., & Murray, N. M. F. (1987). Responses in Small Hand Muscles From Magnetic Stimulation of the Brain. *J. Physiol.*, *388*, 397–419.

Huang, Y. Z., Edwards, M. J., Rounis, E., Bhatia, K. P., & Rothwell, J. C. (2005). Theta burst stimulation of the human motor cortex. *Neuron*, *45*(2), 201–206. doi: 10.1016/j.neuron.2004.12.033

Huber, L., Finn, E. S., Handwerker, D. A., Bönstrup, M., Glen, D. R., Kashyap, S., ... Bandettini, P. A. (2020). Sub-millimeter fMRI reveals multiple topographical digit representations that form action maps in human motor cortex. *NeuroImage*, *208*(November 2019). doi: 10.1016/j.neuroimage.2019.116463

Jenkinson, M., Beckmann, C. F., Behrens, T. E., & Woolrich, M. W. (2012). 720 Smith SM (2012) FSL. *NeuroImage*, *62*, 782–790. doi: 10.1016/j.NeuroImage.2011.09.015

Julkunen, P., Säisänen, L., Hukkanen, T., Danner, N., & Könönen, M. (2012). Does second-scale intertrial interval affect motor evoked potentials induced by single-pulse transcranial magnetic stimulation? *Brain Stimulation*, *5*(4), 526–532. doi: 10.1016/j.brs.2011.07.006

Kammer, T., Beck, S., Thielscher, A., Laubis-Herrmann, U., & Topka, H. (2001). Motor thresholds in humans: a transcranial magnetic stimulation study comparing different pulse waveforms, current directions and stimulator types. *Clinical neurophysiology*, *112*(2), 250–258.

Kleim, J. A., Kleim, E. D., & Cramer, S. C. (2007). Systematic assessment of training-induced changes in corticospinal output to hand using frameless stereotaxic transcranial magnetic stimulation. *Nature protocols*, *2*(7), 1675–1684. doi: 10.1038/nprot.2007.206

Koponen, L. M., Goetz, S. M., Tucci, D. L., & Peterchev, A. V. (2020). Sound comparison of seven TMS coils at matched stimulation strength. *Brain Stimulation*, *13*(3), 873–880. doi: 10.1016/j.brs.2020.03.004

Krall, S. C., Volz, L. J., Oberwelland, E., Grefkes, C., Fink, G. R., & Konrad, K. (2016). The right temporoparietal junction in attention and social interaction: A transcranial magnetic stimulation study. *Human Brain Mapping*, *37*(2), 796–807. doi: 10.1002/hbm.23068

Kraus, D., & Gharabaghi, A. (2015). Projecting navigated TMS sites on the gyral anatomy decreases inter-subject variability of cortical motor maps. *Brain Stimulation*, *8*(4), 831–837. doi: 10.1016/j.brs.2015.03.006

Kraus, D., & Gharabaghi, A. (2016). Neuromuscular plasticity: disentangling stable and variable motor maps in the human sensorimotor cortex. *Neural plasticity*, *2016*.

Krieg, S. M., Lioumis, P., Mäkelä, J. P., Wilenius, J., Karhu, J., Hannula, H., . . . Picht, T. (2017). Protocol for motor and language mapping by navigated TMS in patients and healthy volunteers; workshop report. *Acta Neurochirurgica*, *159*(7), 1187–1195. doi: 10.1007/s00701-017-3187-z

Krieg, T. D., Salinas, F. S., Narayana, S., Fox, P. T., & Mogul, D. J. (2013). PET-based confirmation of orientation sensitivity of TMS-induced cortical activation in humans. *Brain Stimulation*, *6*(6), 898–904. doi: 10.1016/j.brs.2013.05.007

Kuhnke, P., Meyer, L., Friederici, A. D., & Hartwigsen, G. (2017). Left posterior inferior frontal gyrus is causally involved in reordering during sentence processing. *NeuroImage*. doi: 10.1016/j.neuroimage.2017.01.013

Laakso, I., Murakami, T., Hirata, A., & Ugawa, Y. (2018). Where and what TMS activates: Experiments and modeling. *Brain Stimulation*, *11*(1), 166–174. doi: 10.1016/j.brs.2017.09.011

Li, X., Morgan, P. S., Ashburner, J., Smith, J., & Rorden, C. (2016). The first step for neuroimaging data analysis: DICOM to NIfTI conversion. *Journal of neuroscience methods*, *264*, 47–56.

Magnusson, C. E., & Stevens, H. C. (1914). Visual sensations caused by a magnetic field. *The London, Edinburgh, and Dublin Philosophical Magazine and Journal of Science*, *28*(164), 188–207. doi: 10.1080/14786440808635200

Magsood, H., & Hadimani, R. L. (2021). Development of anatomically accurate brain phantom for experimental validation of stimulation strengths during TMS. *Materials Science and Engineering C*, *120*, 111705. doi: 10.1016/j.msec.2020.111705

Mandija, S., Petrov, P. I., Neggers, S. F., Luijten, P. R., & van den Berg, C. A. (2016). MR-based measurements and simulations of the magnetic field created by a realistic transcranial magnetic stimulation (TMS) coil and stimulator. *NMR in Biomedicine*, *29*(11), 1590–1600. doi: 10.1002/nbm.3618

Martuzzi, R., van der Zwaag, W., Farthouat, J., Gruetter, R., & Blanke, O. (2014). Human finger somatotopy in areas 3b, 1, and 2: A 7T fMRI study using a natural stimulus. *Human Brain Mapping*, *35*(1), 213–226. doi: 10.1002/hbm.22172

Mathew, J., Kübler, A., Bauer, R., & Gharabaghi, A. (2016). Probing corticospinal recruitment patterns and functional synergies with transcranial magnetic stimulation. *Frontiers in cellular neuroscience*, *10*, 175. doi: 10.3389/fncel.2016.00175

Maykaa, M., Corcos, D. M., Leurgans, S. E., & Vaillancourt, D. E. (2006). Three-dimensional locations and boundaries of motor and premotor cortices as defined by functional brain imaging. *Neuroimage*, *31*(4), 1453–1474. doi: 10.1016/j.neuroimage.2006.02.004

McLean, A. L. (2019). Publication trends in transcranial magnetic stimulation: a 30-year panorama. *Brain Stimulation*, *12*(3), 619–627. doi: 10.1016/j.brs.2019.01.002

Mills, K. R., Boniface, S. J., & Schubert, M. (1992). Magnetic brain stimulation with a double coil: the importance of coil orientation. *Electroencephalography and Clinical Nneurophysiology*, *85*(1), 17–21. doi: 10.1016/0168-5597(92)90096-t

Moezzi, B., Schaworonkow, N., Plogmacher, L., Goldsworthy, M. R., Hordacre, B., McDonnell, M. D., ... Triesch, J. (2018). Simulation of electromyographic recordings following transcranial magnetic stimulation. *Journal of Neurophysiology*, *120*(5), 2532–2541. doi: 10.1152/jn.00626.2017

Möller, C., Arai, N., Lücke, J., & Ziemann, U. (2009). Hysteresis effects on the input–output curve of motor evoked potentials. *Clinical Neurophysiology*, *120*(5), 1003–1008. doi: 10.1016/j.clinph.2009.03.001

Müller, F., & Ziemann, U. (2007). Bestimmung der zentralmotorischen Leitungszeit. In *Das TMS-Buch* (pp. 71–78). Springer.

Nazarova, M., Novikov, P., Ivanina, E., Kozlova, K., Dobrynina, L., & Nikulin, V. V. (2021). Mapping of multiple muscles with transcranial magnetic stimulation: absolute and relative test–retest reliability. *Human Brain Mapping*, *42*(8), 2508–2528. doi: 10.1002/hbm.25383

Neggers, S. F. W., Langerak, T. R., Schutter, D. J. L. G., Mandl, R. C. W., Ramsey, N. F., Lemmens, P. J. J., & Postma, A. (2004). A stereotactic method for image-guided transcranial magnetic stimulation validated with fMRI and motor-evoked potentials. *Neuroimage*, *21*(4), 1805–1817. doi: 10.1016/j.neuroimage.2003.12.006

Ngomo, S., Leonard, G., Moffet, H., & Mercier, C. (2012). Comparison of transcranial magnetic stimulation measures obtained at rest and under active conditions and their reliability. *Journal of neuroscience methods*, *205*(1), 65–71.

Nielsen, J. F. (1996). Logarithmic distribution of amplitudes of compound muscle action potentials evoked by transcranial magnetic stimulation. *Journal of Clinical Neurophysiology*, *13*(5), 423–434. doi: 10.1097/00004691-199609000-00005

Nielsen, J. F., Madsen, K. H., Puonti, O., Siebner, H. R., Bauer, C., Madsen, C. G., . . . Thielscher, A. (2018). Automatic skull segmentation from MR images for realistic volume conductor models of the head: Assessment of the state-of-the-art. *Neuroimage*, *174* (March), 587–598. doi: 10.1016/j.neuroimage.2018.03.001

Ninomiya, T., ichi Inoue, K., Hoshi, E., & Takada, M. (2019). Layer specificity of inputs from supplementary motor area and dorsal premotor cortex to primary motor cortex in macaque monkeys. *Scientific Reports*, *9* (1). doi: 10.1038/s41598-019-54220-z

Nummenmaa, A., Stenroos, M., Ilmoniemi, R. J., Okada, Y. C., Hämäläinen, M. S., & Raij, T. (2013). Comparison of spherical and realistically shaped boundary element head models for transcranial magnetic stimulation navigation. *Clinical Neurophysiology*, *124* (10), 1995–2007.

Numssen, O., Bzdok, D., & Hartwigsen, G. (2021). Functional specialization within the inferior parietal lobes across cognitive domains. *elife*, *10*. doi: 10.7554/eLife.63591

Numssen, O., Weise, K., Kalloch, B., Zier, A.-L., Thielscher, A., Hartwigsen, G., & Knösche, T. R. (2022). *Precise motor mapping with transcranial magnetic stimulation - data and code.* https://osf.io/myrqn/. doi: 10.17605/OSF.IO/MYRQN

Numssen, O., Zier, A.-L., Thielscher, A., Hartwigsen, G., Knösche, T. R., & Weise, K. (2021). Efficient high-resolution TMS mapping of the human motor cortex by nonlinear regression. *NeuroImage*, *245*, 118654. doi: 10.1016/j.neuroimage.2021.118654

Oldfield, R. C. (1971). The assessment and analysis of handedness: The Edinburgh inventory. *Neuropsychologia*, *9* (1), 97–113. doi: 10.1016/0028-3932(71)90067-4

Opitz, A., Legon, W., Rowlands, A., Bickel, W. K., Paulus, W., & Tyler, W. J. (2013). Physiological observations validate finite element models for estimating subject-specific electric field distributions induced by transcranial magnetic stimulation of the human motor cortex. *NeuroImage*, *81*, 253–264.

Opitz, A., Windhoff, M., Heidemann, R. M., Turner, R., & Thielscher, A. (2011). How the brain tissue shapes the electric field induced by transcranial magnetic stimulation. *NeuroImage*, *58*(3), 849–859. doi: 10.1016/j.neuroimage.2011.06.069

Opitz, A., Zafar, N., Bockermann, V., Rohde, V., & Paulus, W. (2014). Validating computationally predicted TMS stimulation areas using direct electrical stimulation in patients with brain tumors near precentral regions. *NeuroImage: Clinical*, *4*, 500–507.

Pascual-Leone, A., Bartres-Faz, D., & Keenan, J. (1999). Transcranial magnetic stimulation: studying the brain-behaviour relationship by induction of 'virtual lesions'. *Philosophical Transactions of the Royal Society of London. Series B: Biological Sciences*, *354*(1387), 1229–1238.

Pascual-Leone, A., Davey, N. J., Rothwell, J., Wasserman, E. M., & Puri, B. K. (2002). *Handbook of transcranial magnetic stimulation.* Arnold.

Pascual-Leone, A., Houser, C. M., Reese, K., Shotland, L. I., Grafman, J., Sato, S., ... Hallett, M. (1993, apr). Safety of rapid-rate transcranial magnetic stimulation in normal volunteers. *Electroencephalography and Clinical Neurophysiology/Evoked Potentials Section*, *89*(2), 120–130. doi: 10.1016/0168-5597(93)90094-6

Paus, T. (2005). Inferring causality in brain images: a perturbation approach. *Philosophical transactions of the Royal Society of London. Series B, Biological sciences*, *360*(1457), 1109–1114. doi: 10.1098/rstb.2005.1652

Pellegrini, M., Zoghi, M., & Jaberzadeh, S. (2018). The effect of transcranial magnetic stimulation test intensity on the amplitude, variability and reliability of motor evoked potentials. *Brain Research*, *1700*(May), 190–198. doi: 10.1016/j.brainres.2018.09.002

Pelletier, I., Sauerwein, H. C., Lepore, F., Saint-Amour, D., & Lassonde, M. (2007). Non-invasive alternatives to the Wada test in the presurgical evaluation of language and memory functions in epilepsy patients. *Epileptic disorders*, *9*(2), 111–126.

Penfield, W., & Rasmussen, T. (1950). *The cerebral cortex of man; a clinical study of localization of function.* Macmillan.

Penny, W., Friston, K. J., Ashburner, J., Kiebel, S. J., & Nichols, T. E. (2011). *Statistical parametric mapping: The analysis of functional brain images.* Academic press.

Peterchev, A. V., Goetz, S. M., Westin, G. G., Luber, B., & Lisanby, S. H. (2013). Pulse width dependence of motor threshold and input–output curve characterized with controllable pulse parameter transcranial magnetic stimulation. *Clinical Neurophysiology*, *124*(7), 1364–1372.

Pitkänen, M., Kallioniemi, E., Julkunen, P., Nazarova, M., Nieminen, J. O., & Ilmoniemi, R. J. (2017). Minimum-Norm Estimation of Motor Representations in Navigated TMS Mappings. *Brain Topography*, *30*(6), 711–722. doi: 10.1007/s10548-017-0577-8

Posner, M. I. (1980). Orienting of attention. *The Quarterly journal of experimental psychology*, *32*(1), 3–25. doi: 10.1080/00335558008248231

Preuss, T. M., Stepniewska, I., & Kaas, J. H. (1996). Movement representation in the dorsal and ventral premotor areas of owl monkeys: A microstimulation study. *Journal of Comparative Neurology*, *371*(4), 649–676. doi: 10.1002/(SICI)1096-9861(19960805)371:4<649::AID-CNE12>3.0.CO;2-E

Puonti, O., Van Leemput, K., Saturnino, G. B., Siebner, H. R., Madsen, K. H., & Thielscher, A. (2020). Accurate and robust whole-head segmentation from magnetic resonance images for individualized head modeling. *Neuroimage*, *219*(February), 117044. doi: 10.1016/j.neuroimage.2020.117044

Raffin, E., Pellegrino, G., Di Lazzaro, V., Thielscher, A., & Siebner, H. R. (2015). Bringing transcranial mapping into shape: sulcus-aligned mapping captures motor somatotopy in human primary motor hand area. *Neuroimage*, *120*, 164–175.

Raffin, E., & Siebner, H. R. (2019). Use-dependent plasticity in human primary motor hand area: synergistic interplay between training and immobilization. *Cerebral Cortex*, *29*(1), 356–371.

Ravazzani, P., Ruohonen, J., Grandori, F., & Tognola, G. (1996). Magnetic stimulation of the nervous system: induced electric field in unbounded, semi-infinite, spherical, and cylindrical media. *Annals of biomedical engineering*, *24*(5), 606–616.

Rizzolatti, G., & Fabbri-Destro, M. (2009). Premotor Cortex in Primates: Dorsal and Ventral. *Encyclopedia of Neuroscience*, 935–945. doi: 10.1016/B978-008045046-9.01320-6

Rosanova, M., Casali, A., Bellina, V., Resta, F., Mariotti, M., & Massimini, M. (2009). Natural frequencies of human corticothalamic circuits. *Journal of Neuroscience*, *29*(24), 7679–7685.

Rösler, J., Niraula, B., Strack, V., Zdunczyk, A., Schilt, S., Savolainen, P., … Others (2014). Language mapping in healthy volunteers and brain tumor patients with a novel navigated TMS system: evidence of tumor-induced plasticity. *Clinical Neurophysiology*, *125*(3), 526–536.

Rossi, S., Antal, A., Bestmann, S., Bikson, M., Brewer, C., Brockmöller, J., … Hallett, M. (2021). Safety and recommendations for TMS use in healthy subjects and patient populations, with updates on training, ethical and regulatory issues: Expert Guidelines. *Clinical Neurophysiology*, *132*(1), 269–306. doi: 10.1016/j.clinph.2020.10.003

Rossi, S., Hallett, M., Rossini, P. M., Pascual-Leone, A., Avanzini, G., Bestmann, S., … Ziemann, U. (2009). Safety, ethical considerations, and application guidelines for the use of transcranial magnetic stimulation in clinical practice and research. *Clinical Neurophysiology*, *120*(12), 2008–2039. doi: 10.1016/j.clinph.2009.08.016

Rossini, P. M., Barker, A. T., Berardelli, A., Caramia, M. D., Caruso, G., Cracco, R. Q., … Lücking, C. H. (1994). Non-invasive electrical and magnetic stimulation of the brain, spinal cord and roots: basic principles and procedures for routine clinical application. Report of an IFCN committee. *Electroencephalography and Cinical Neurophysiology*, *91*(2), 79–92. doi: 10.1016/0013-4694(94)90029-9

Rossini, P. M., Burke, D., Chen, R., Cohen, L. G., Daskalakis, Z., Di Iorio, R., … Ziemann, U. (2015). Non-invasive electrical and magnetic stimulation of the brain,

spinal cord, roots and peripheral nerves: Basic principles and procedures for routine clinical and research application: An updated report from an I.F.C.N. Committee. *Clinical Neurophysiology*, *126*(6), 1071–1107. doi: 10.1016/j.clinph.2015.02.001

Rothwell, J. C., Hallett, M., Berardelli, A., Eisen, A., Rossini, P., & Paulus, W. (1999). Magnetic stimulation: motor evoked potentials. The International Federation of Clinical Neurophysiology. *Electroencephalography and clinical neurophysiology. Supplement*, *52*, 97–103.

Ruohonen, J., & Karhu, J. (2010). Navigated transcranial magnetic stimulation. *Neurophysiologie Clinique*, *40*(1), 7–17. doi: 10.1016/j.neucli.2010.01.006

Rushworth, M. F. S., Ellison, A., & Walsh, V. (2001). Complementary localization and lateralization of orienting and motor attention. *Nature Neuroscience*, *4*(6), 656–661. doi: 10.1038/88492

Sakreida, K., Blume-Schnitzler, J., Heim, S., Willmes, K., Clusmann, H., & Neuloh, G. (2019). Phonological picture–word interference in language mapping with transcranial magnetic stimulation: an objective approach for functional parcellation of Broca's region. *Brain Structure and Function*, *224*(6), 2027–2044. doi: 10.1007/s00429-019-01891-z

Sakreida, K., Lange, I., Willmes, K., Heim, S., Binkofski, F., Clusmann, H., & Neuloh, G. (2018). High-resolution language mapping of Broca's region with transcranial magnetic stimulation. *Brain Structure and Function*, *223*(3), 1297–1312. doi: 10.1007/s00429-017-1550-8

Salinas, F. S., Szabó, C. Á., Zhang, W., Jones, L., Leland, M. M., Wey, H.-Y., ... Narayana, S. (2011). Functional neuroimaging of the baboon during concurrent image-guided transcranial magnetic stimulation. *NeuroImage*, *57*(4), 1393–1401.

Salvador, R., Silva, S., Basser, P. J., & Miranda, P. (2011). Determining which mechanisms lead to activation in the motor cortex: A modeling study of transcranial magnetic stimulation using realistic stimulus waveforms and sulcal geometry. *Clinical Neurophysiology*, *122*(4), 748–758. doi: 10.1016/j.clinph.2010.09.022

Sasaki, T., Kodama, S., Togashi, N., Shirota, Y., Sugiyama, Y., ichi Tokushige, S., ... Hamada, M. (2018). The intensity of continuous theta burst stimulation, but not the waveform used to elicit motor evoked potentials, influences its outcome in the human motor cortex. *Brain Stimulation*, *11*(2), 400–410. doi: 10.1016/j.brs.2017.12.003

Saturnino, G. B., Madsen, K. H., & Thielscher, A. (2019). Electric field simulations for transcranial brain stimulation using FEM: an efficient implementation and error analysis. *Journal of Neural Engineering*, *16*(6), 66032. doi: 10.1088/1741-2552/ab41ba

Saturnino, G. B., Puonti, O., Nielsen, J. D., Antonenko, D., Madsen, K. H., & Thielscher, A. (2019). SimNIBS 2.1: A Comprehensive Pipeline for Individualized Electric Field Modelling for Transcranial Brain Stimulation. *Brain and Human Body Modeling*, 3–25. doi: 10.1007/978-3-030-21293-3_1

Saturnino, G. B., Thielscher, A., Madsen, K. H., Knösche, T. R., & Weise, K. (2019). A principled approach to conductivity uncertainty analysis in electric field calculations. *NeuroImage*, *188*(December 2018), 821–834. doi: 10.1016/j.neuroimage.2018.12.053

Schmidt, S., Cichy, R. M., Kraft, A., Brocke, J., Irlbacher, K., & Brandt, S. A. (2009). An initial transient-state and reliable measures of corticospinal excitability in TMS studies. *Clinical Neurophysiology*, *120*(5), 987–993.

Seo, H., Schaworonkow, N., Jun, S. C., & Triesch, J. (2016). A multi-scale computational model of the effects of TMS on motor cortex. *F1000Research*, *5*.

Shamov, T., Spiriev, T., Tzvetanov, P., & Petkov, A. (2010). The combination of neuronavigation with transcranial magnetic stimulation for treatment of opercular gliomas of the dominant brain hemisphere. *Clinical neurology and neurosurgery*, *112*(8), 672–677.

Siddiqi, S. H., Kording, K. P., Parvizi, J., & Fox, M. D. (2022a). Causal mapping of human brain function. *Nature Reviews Neuroscience*, *23*(6), 361–375. doi: 10.1038/s41583-022-00583-8

Siddiqi, S. H., Kording, K. P., Parvizi, J., & Fox, M. D. (2022b). Causal mapping of human brain function. *Nature reviews neuroscience*, *23*(6), 361–375.

Siebner, H. R. (2020). Does TMS of the precentral motor hand knob primarily stimulate the dorsal premotor cortex or the primary motor hand area? *Brain Stimulation*, *13*(2), 517–518. doi: 10.1016/j.brs.2019.12.015

Siebner, H. R., Funke, K., Aberra, A. S., Antal, A., Bestmann, S., Chen, R., . . . Ugawa, Y. (2022). Transcranial magnetic stimulation of the brain: What is stimulated? – A consensus and critical position paper. *Clinical Neurophysiology*, *140*, 59–97. doi: 10.1016/j.clinph.2022.04.022

Siebner, H. R., & Rothwell, J. (2003). Transcranial magnetic stimulation: new insights into representational cortical plasticity. *Experimental brain research*, *148*(1), 1–16.

Silva, S., Basser, P. J., & Miranda, P. (2008). Elucidating the mechanisms and loci of neuronal excitation by transcranial magnetic stimulation using a finite element model of a cortical sulcus. *Clinical Neurophysiology*, *119*, 2405—-2413. doi: 10.1016/j.clinph.2008.07.248

Smith, S. M., Jenkinson, M., Woolrich, M. W., Beckmann, C. F., Behrens, T., Johansen-Berg, H., . . . Flitney, D. E. (2004). Advances in functional and structural MR image analysis and implementation as FSL. *NeuroImage*, *23*, S208—-S219.

Sommer, M., Alfaro, A., Rummel, M., Speck, S., Lang, N., Tings, T., & Paulus, W. (2006). Half sine, monophasic and biphasic transcranial magnetic stimulation of the human motor cortex. *Clinical neurophysiology*, *117*(4), 838–844.

Sondergaard, R. E., Martino, D., Kiss, Z. H., & Condliffe, E. G. (2021). TMS Motor Mapping Methodology and Reliability: A Structured Review. *Frontiers in Neuroscience*, *15*(August), 1–13. doi: 10.3389/fnins.2021.709368

Stokes, M. G., Chambers, C. D., Gould, I. C., Henderson, T. R., Janko, N. E., Allen, N. B., & Mattingley, J. B. (2005). Simple metric for scaling motor threshold based on scalp-cortex distance: Application to studies using transcranial magnetic stimulation. *Journal of neurophysiology*, *94*(6), 4520–4527. doi: 10.1152/jn.00067.2005

Thielscher, A., Antunes, A., & Saturnino, G. B. (2015). Field modeling for transcranial magnetic stimulation: A useful tool to understand the physiological effects of TMS? *Proceedings of the Annual International Conference of the IEEE Engineering in Medicine and Biology Society, EMBS*, *2015-Novem*, 222–225. doi: 10.1109/EMBC.2015.7318340

Thielscher, A., & Kammer, T. (2002). Linking physics with physiology in TMS: A sphere field model to determine the cortical stimulation site in TMS. *NeuroImage*, *17*, 1117—-1130. doi: 10.1006/nimg.2002.1282

Thielscher, A., Opitz, A., & Windhoff, M. (2011). Impact of the gyral geometry on the electric field induced by transcranial magnetic stimulation. *NeuroImage*, *54*(1), 234–243. doi: 10.1016/j.neuroimage.2010.07.061

Thielscher, A., Reichenbach, A., Uurbil, K., & Uluda, K. (2010). The cortical site of visual suppression by transcranial magnetic stimulation. *Cerebral Cortex*, *20*(2), 328–338. doi: 10.1093/cercor/bhp102

Ueno, S., Tashiro, T., & Harada, K. (1988). Localized stimulation of neural tissues in the brain by means of a paired configuration of time-varying magnetic fields. *Journal of Applied Physics*, *64*(10), 5862–5864.

Van De Ruit, M., Perenboom, M. J. L., & Grey, M. J. (2015). TMS brain mapping in less than two minutes. *Brain stimulation*, *8*(2), 231–239.

Wagner, T. A., Zahn, M., Grodzinsky, A. J., & Pascual-Leone, A. (2004). Three-dimensional head model simulation of transcranial magnetic stimulation. *IEEE Transactions on Biomedical Engineering*, *51*(9), 1586–1598. doi: 10.1109/TBME.2004.827925

Walsh, V., & Pascual-Leone, A. (2003). *Transcranial magnetic stimulation: A neurochromometrics of mind.* MIT press.

Weise, K., Numssen, O., Kalloch, B., Zier, A.-L., Thielscher, A., Haueisen, J., . . . Knösche, T. R. (2022). Precise transcranical magnetic stimulation motor mapping. *Nature Protocols*. doi: 10.1038/s41596-022-00776-6

Weise, K., Numssen, O., Thielscher, A., Hartwigsen, G., & Knösche, T. R. (2020). A novel approach to localize cortical TMS effects. *NeuroImage*, *209*, 116486. doi: 10.1016/j.neuroimage.2019.116486

Wilson, S. A., Thickbroom, G. W., & Mastaglia, F. L. (1993). Transcranial magnetic stimulation mapping of the motor cortex in normal subjects: the representation of two intrinsic hand muscles. *Journal of the neurological sciences*, *118*(2), 134–144.

Windhoff, M., Opitz, A., & Thielscher, A. (2013). Electric field calculations in brain stimulation based on finite elements: An optimized processing pipeline for the generation and usage of accurate individual head models. *Human Brain Mapping*, *34*(4), 923–935. doi: 10.1002/hbm.21479

Witham, C. L., Fisher, K. M., Edgley, S. A., & Baker, S. N. (2016). Corticospinal inputs to primate motoneurons innervating the forelimb from two divisions of primary motor cortex and area 3a. *Journal of Neuroscience*, *36*(9), 2605–2616. doi: 10.1523/JNEUROSCI.4055-15.2016

Woolrich, M. W., Jbabdi, S., Patenaude, B., Chappell, M., Makni, S., Behrens, T., ... Smith, S. M. (2009). Bayesian analysis of neuroimaging data in FSL. *NeuroImage*, *45*(1 Suppl), S173—-S186. doi: 10.1016/j.neuroimage.2008.10.055

Wu, J., Ngo, G. H., Greve, D., Li, J., He, T., Fischl, B., ... Yeo, B. T. (2018). Accurate nonlinear mapping between MNI volumetric and FreeSurfer surface coordinate systems. *Human Brain Mapping*, *39*(9), 3793–3808. doi: 10.1002/hbm.24213

Yousry, T. A., Schmid, U. D., Alkadhi, H., Schmidt, D., Peraud, A., Buettner, A., & Winkler, P. (1997). Localization of the motor hand area to a knob on the precentral gyrus. A new landmark. *Brain*, *120*(1), 141–157. doi: 10.1093/brain/120.1.141

Yu, C., Li, J., Liu, Y., Qin, W., Li, Y., Shu, N., ... Li, K. (2008). White matter tract integrity and intelligence in patients with mental retardation and healthy adults. *NeuroImage*, *40*(4), 1533–1541. doi: 10.1016/j.neuroimage.2008.01.063

Zheng, K.-Y., Dai, G.-Y., Lan, Y., & Wang, X.-Q. (2020). Trends of Repetitive Transcranial Magnetic Stimulation From 2009 to 2018: A Bibliometric Analysis. *Frontiers in Neuroscience*, *14*(February), 1–11. doi: 10.3389/fnins.2020.00106

Ziemann, U., & Siebner, H. R. (2015). Inter-subject and intersession variability of plasticity induction by non-invasive brain stimulation: Boon or bane? *Brain Stimulation*, *8*(3), 662–663. doi: 10.1016/j.brs.2015.01.409

Zienkiewicz, O. C., & Zhu, J. Z. (1992). The superconvergent patch recovery and aposteriori error estimates. Part 1: the recovery technique. *International Journal for Numerical Methods in Engineering*, *33*, 1331–1364. doi: 10.1002/nme.1620330702

Zilles, K., & Amunts, K. (2010). Centenary of Brodmann's map conception and fate. *Nature Reviews Neuroscience*, *11*(2), 139–145. doi: 10.1038/nrn2776

Zmeykina, E., Mittner, M., Paulus, W., & Turi, Z. (2020). Weak rTMS-induced electric fields produce neural entrainment in humans. *Scientific reports*, *10*(1), 1–16. doi: 10.1038/s41598-020-68687-8